



Norwegian University of  
Science and Technology

# Analysis and Design of Stiffened Columns in Offshore Floating Platforms Subjected to Supply Vessel Impacts

**Terje Skogan Bøe**

Marine Technology

Submission date: June 2018

Supervisor: Jørgen Amdahl, IMT

Norwegian University of Science and Technology  
Department of Marine Technology





## MASTER THESIS 2018

For

Stud. Techn. Terje Skogan Bøe

### **Analysis and Design of Stiffened Columns in Offshore Floating Platforms to Supply Vessel Impacts**

*Analyse og dimensjonering av avstivede søyler i offshore plattformers utsatt for støt fra forsyningskip*

Supply vessels, passing merchant vessels and shuttle tankers are regarded a major threat for offshore structures and platforms are often designed intentionally to resist collisions. In Norwegian sector of the North Sea the standard design event has been a supply vessel of 5,000 tons displacement sailing into a platform with a speed of 2m/s. With the recent update of NORSOK N-003 the standard size for a supplyvessel is 10,000 tons. For bow collisions the speed has increased to 3 m/s. For design purposes standard force-deformation curves for bow, side and stern impacts are defined in NORSOK N-004 Appendix A for bow, sideways and stern impact. Appendix A is essentially identical to the recommended practice DNV-GL RP-C204 from 2010. A revision of RP-C204 is expected in the fall of 2017, with a significant update on design force-deformation curves for supply vessels. However, there are relatively few new clauses for the structural design of large, diameter stiffened cylinders.

With respect to the distribution of strain energy dissipation there may be distinguished between three design principles, namely *strength design*, *ductility design* and *shared-energy design* depending upon the relative strength the ship and the platform:

*Strength design* implies that the platform is strong enough to resist the collision force with minor deformation, so that the striking ship is forced to deform and dissipate the major part of the collision energy. *Ductility design* implies that the platform undergoes large, plastic deformations and dissipates the major part of the collision energy.

*Shared energy design* implies that both the platform and the striking ship contribute significantly to the energy dissipation.

From a calculation point of view, strength design or ductility design is favorable. In strength design, it is only necessary to verify that the struck ship is capable of resisting the total collision force and the local high pressure intensities during the deformation process. In ductility design, the shape of the deformation is highly dominated by the geometry of the striking ship structure and the energy dissipation can be analyzed by means of plastic methods. In shared energy design, both the magnitude and the distribution of the collision force depend upon the deformation of both ships. This interaction makes the analysis more complex and calls for nonlinear finite element analysis. In most cases ductility or shared energy design is used or assumed. However, strength design may in some cases be achieved with small changes in structural configuration or material improvement.

The purpose of this work is to contribute to the development of simplified methods and guidance for the design of large diameter stiffened columns of semi-submersibles. The work can also be relevant for the design of columns/pontoons in floating bridges and offshore fish farms

The following topics should be addressed:

1. Complete the script developed for automatic generation of finite element mesh for stiffened columns. Based on the review of typical dimensions of stiffened columns propose a parametric study where the scantlings, e.g. the diameter, thickness, frame spacing, compartmentalization as well as material strength may be varied. It may be considered to vary the parameters beyond “normal” values
2. Perform finite element analysis of ship collision against the modeled columns with LS-DYNA. Analysis shall be conducted for stern, bow and side impacts. Existing ship finite element models will be made available. To the extent possible conduct also simulations where the rigid body motions are also included in LS-DYNA simulations. Develop force-intensity curves for various contact areas. Describe the damage pattern. Material fracture and tearing due to excessive straining of watertight compartments shall be considered
3. Compare the results of numerical simulations with estimates based on simple methods for analysis of external and internal mechanics. . Emphasis shall be placed on the methods behind the current and the proposed new requirements given in DNV GL RP-C204. The applicability of the method proposed by Yu et.al.: *Large inelastic deformation resistance of stiffened panels subjected to lateral loading* J. of Marine Structures, 2018 shall be evaluated. . Consider also models to estimate the energy dissipation in decks/stringers and bulkheads
4. Based on the experience obtained from the simulations and comparisons with simplified methods propose modifications to improve the accuracy of the simplified methods. Propose requirements that may be applied for strength design of stiffened columns.
5. Conclusions and recommendations for further work

Literature studies of specific topics relevant to the thesis work may be included.

The work scope may prove to be larger than initially anticipated. Subject to approval from the supervisor, topics may be deleted from the list above or reduced in extent.

In the thesis the candidate shall present his personal contribution to the resolution of problems within the scope of the thesis work.

Theories and conclusions should be based on mathematical derivations and/or logic reasoning identifying the various steps in the deduction.

The candidate should utilize the existing possibilities for obtaining relevant literature.

The thesis should be organized in a rational manner to give a clear exposition of results, assessments, and conclusions. The text should be brief and to the point, with a clear language. Telegraphic language should be avoided.

The thesis shall contain the following elements: A text defining the scope, preface, list of contents, summary, main body of thesis, conclusions with recommendations for further work, list of symbols and acronyms, references and (optional) appendices. All figures, tables and equations shall be numerated.

The supervisor may require that the candidate, in an early stage of the work, presents a written plan for the completion of the work. The plan should include a budget for the use of computer and laboratory resources which will be charged to the department. Overruns shall be reported to the supervisor.

The original contribution of the candidate and material taken from other sources shall be clearly defined. Work from other sources shall be properly referenced using an acknowledged referencing system.

The report shall be submitted in two copies:

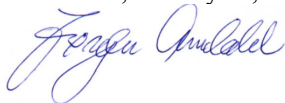
- Signed by the candidate
- The text defining the scope included
- In bound volume(s)
- Drawings and/or computer prints which cannot be bound should be organized in a separate folder.

**Supervisor:**  
Prof. Jørgen Amdahl

**Co-supervisor**  
PhD Zhaolong Yu

**Deadline:, June 11, 2018**

Trondheim, January 15, 2018



Jørgen Amdahl



---

## Abstract

In this work the resistance of a stiffened column exposed to stern corner impacts is studied. The effect of ring and vertical stiffeners are explored, as well as the effect of decks and bulkheads. It is found that the ring stiffener is an important part of the load carrying structure for radial loads. These are therefore isolated and studied in greater detail.

The ring stiffeners are analysed as a semicircular arch using several analytical models, as well as with the finite element method. It is shown that the collapse load for a ring stiffener with a stocky cross section can be well estimated by both a static and a kinematic model. For a more slender cross section local effects such as buckling of the web and top flange is important for the response.

A folding line model for the local collapse of the cross section is proposed, and included in the kinematic model. This increases the accuracy of the model significantly, especially for slender cross sections at large displacements.

The accuracy of the statical model was improved by introducing interaction equations between the moment capacity and the axial load. This resulted in a iterative formula.

Finite element analyses of stern corner impacts have been performed for several different designs of stiffened columns to determine how a strength design can be obtained. It is found that the collapse of the ring stiffeners give a reduction in capacity and subsequently large deformations. This collapse load is therefore proposed as a limit for strength design.

The vertical stiffening is shown to influence the collapse load by restraining the lateral displacement of the ring stiffener web, in addition to providing the necessary strength to carry the impact load to the ring stiffeners.

The effect of decks was found to be minor with respect to the initial collapse, but important for the energy dissipation at large deformations. Bulkheads were found to give little to no extra capacity apart from the case where they are directly inline with the impact direction.

## Sammendrag

I denne oppgaven har en avstivet sirkulær sylinder ustatt for skipsstøt blitt analysert. Effekten av ulike geometriske parametere har blitt utforsket, blandt annet dimensjonene av ringstiverne of vertikalstiverne. Effekten av dekk og skott ble også studert. Ringstiverene viste seg å være viktige for strukturens evne til å bære radielle laster. Disse ble derfor isolert og studert nøyere.

Ringstiverene ble analysert som en sirkulær bue med flere ulike analytiske metoder. For forholdsvis kompakte tverrsnitt kan sammenbruddslasten tilnærmes godt ved hjelp av både statiske og kinematiske beregningsmodeller. For slanke tverrsnitt blir lokale effekter som buling av ringstiverens steg og toppflens viktig, og mer sofistikerte metoder er nødvendig.

For å forbedre nøyaktigheten til den kinematiske modellen ble en lokal folde-mekaniske introdusert. Denne modellen ga betydelig bedre samsvar mellom den analytiske modellen og elementmetode-beregninger, spesielt for slanke tverrsnitt og ved store utbøyninger.

Nøyaktigheten til den statiske analysen ble forbedret ved å innføre interaksjons-likninger som beskriver samvirke mellom momentkapasitet og aksielle laster. Det resulterende uttrykket er på en iterativ form.

Elementmetodeanalyser ble utført av flere ulike søyledesign utsatt for hekkhjørnekollisjoner for å undersøke hvordan man mest effektivt kan oppnå et styrkedesign. Når ringstiverene når sammenbruddslasten mister strukturen evnen til å motstå kollisjonskraften og store deformasjoner oppstår. Denne kapasiteten er derfor foreslått som en grense for styrkedesign.

De vertikale stiverne er vist å påvirke sammenbrukkslasten ved å motvirke vertikale forsyvninger av ringstiverseget, i tillegg til å bære kontakttrykket som virker på konstruksjonen mellom ringstiverene.

Effekten av dekk og skott ble deretter undersøkt. Tilstedeværelsen av dekk viste seg å ikke påvirke kollapslasten signifikant, men bidro kraftig til reststyrken etter første kollaps. Vertikale skott bidrar lite hvis ikke skipsstøtet treffer direkte på linje med skottet.



---

## Preface

This master thesis is the result of the work done during the spring semester 2018. The thesis marks the culmination of a five year Master of Science degree in marine technology at the Norwegian University of Science and Technology. The thesis is an extension of the work I did as a project thesis during the autumn of 2017, and some of the modelling and literature study was conducted during that work.

During the thesis the scope of work have been adjusted in agreement with the project supervisor, Professor Jørgen Amdahl. The main change is that the effect of the rigid body motions of the ship have been neglected in all analysis. This was done to be able to use more time on the study of the ring stiffeners. The focus have also been shifted towards the stern corner impact, with the bow and side scenarios only used for comparison. This is manly done in an effort to try and understand the underlying mechanisms of the impact before changing too many variables.

The scope of work also includes a reference to the newly proposed method by Yu (2017) regarding large inelastic response of stiffened plates. This method was reviewed and found not to be relevant as the capacity is governed by the ring stiffeners. However the approach used to reach this method highly inspired the work herein. The interaction equations he proposed as a part of his work are directly used.

I would like to thank my supervisor Professor Jørgen Amdahl for help and guidance during the work, and for giving me the opportunity to explore the task at hand without to much intervention. My co-supervisor Zhalong Yu gave valuable guidance in the use of the analysis software *LS-DYNA*, I owe him a thanks for giving of his time to help me in my project. I would also like to thank PhD Yanyan Sha for giving a helpful introduction to the modelling and analysis procedure using *Patran* and *LS-DYNA* and to PhD Martin Storheim for his willingness to help me understand the implemented material models.



Terje Skogan Bøe  
Trondheim, June 11, 2018

# Contents

<b>1</b>	<b>Nomenclature</b>	<b>ix</b>
<b>2</b>	<b>Abbreviations</b>	<b>x</b>
<b>3</b>	<b>Introduction</b>	<b>1</b>
<b>4</b>	<b>Energy dissipation</b>	<b>3</b>
4.1	Equivalent displacement . . . . .	9
<b>5</b>	<b>Finite element analysis</b>	<b>12</b>
5.1	Nonlinear finite element analysis . . . . .	12
5.1.1	Contact boundary condition . . . . .	14
5.1.2	Two-bar problem . . . . .	15
5.2	Time integration techniques . . . . .	16
5.2.1	Central difference method . . . . .	16
5.2.2	Critical timestep . . . . .	18
<b>6</b>	<b>Material models</b>	<b>20</b>
6.1	Yield criteria . . . . .	20
6.2	Hardening rule . . . . .	21
6.3	Flow rule . . . . .	22
6.4	Tensile failure . . . . .	23
6.5	Material parameters . . . . .	25
<b>7</b>	<b>Ring stiffener collapse load</b>	<b>27</b>
7.1	Bound theorems . . . . .	27
7.2	Slenderness . . . . .	28
7.3	Static analysis . . . . .	29
7.3.1	Elastic phase . . . . .	30
7.3.2	Plastic hinges . . . . .	32
7.3.3	Reduction in moment capacity due to compression . . . . .	35
7.4	Kinematic analysis . . . . .	39
7.4.1	Alternative mechanism . . . . .	41
7.4.2	Folding mechanism . . . . .	45
7.5	Verification using finite elements . . . . .	51
7.5.1	Influence of vertical stiffeners . . . . .	55
<b>8</b>	<b>Collapse of the three dimensional column</b>	<b>56</b>
<b>9</b>	<b>Finite element model</b>	<b>60</b>
9.1	Column model . . . . .	60

9.1.1	Finite element mesh . . . . .	62
9.2	Stern model . . . . .	64
9.3	Effect of boundary conditions . . . . .	65
9.4	Effect of fracture . . . . .	69
9.5	Analysis control . . . . .	70
9.5.1	Contact definitions . . . . .	70
9.5.2	Timestep and mass scaling . . . . .	70
9.5.3	Impact speed . . . . .	72
9.6	Effect of both structures being deformable . . . . .	73
<b>10</b>	<b>Analysis of stern corner impact</b>	<b>74</b>
10.1	Phases of the stern corner impact . . . . .	75
10.2	Impact area and pressure . . . . .	77
10.3	Relative strength . . . . .	79
10.3.1	Internal distribution of energy dissipation . . . . .	81
10.4	Effect of ring stiffeners . . . . .	82
10.5	Effect of vertical stiffeners . . . . .	85
10.6	Effect of shell thickness . . . . .	89
10.7	Effect of bulkhead . . . . .	90
10.8	Effect of deck . . . . .	91
10.9	Side and bow impact . . . . .	92
10.10	Strength design . . . . .	95
<b>11</b>	<b>Conclusion</b>	<b>97</b>
11.1	Strength design . . . . .	98
<b>12</b>	<b>Further work</b>	<b>99</b>
	<b>Bibliography</b>	<b>101</b>
	<b>Appendix A Dimensions</b>	<b>A-1</b>
	<b>Appendix B Control cards used in the analyses</b>	<b>B-1</b>
	<b>Appendix C Derivation of interaction equations</b>	<b>C-1</b>
	<b>Appendix D Derivation of mechanism angles</b>	<b>D-1</b>
	<b>Appendix E Length of diagonal folding lines</b>	<b>E-1</b>
	<b>Appendix F Force deformation curves</b>	<b>F-1</b>

## List of Figures

1	Damaged column leg after supply vessel impact . . . . .	2
2	Correlation between dissipated energy and damaged volume in ship collisions . . . . .	3
3	Design principles . . . . .	4
4	Conventional energy distribution . . . . .	5
5	Design impact force indentation curves . . . . .	8
6	Varying relative resistance . . . . .	9
7	Strain energy versus time . . . . .	10
8	Energy represented by force displacement curves . . . . .	11
9	Penalty method for handling contact problems . . . . .	14
10	The two-bar problem . . . . .	15
11	Discretization of the displacement . . . . .	17
12	Kinematic and isotropic hardening models . . . . .	21
13	Stress strain curves for the implemented material models . . . . .	26
14	Idealized static problem . . . . .	29
15	Ring subjected to opposing forces . . . . .	30
16	Results from elastic analysis . . . . .	31
17	Total moment distribution . . . . .	34
18	Stages of interaction between compression and bending . . . . .	36
19	Interaction between moment capacity and axial force . . . . .	37
20	Kinematic model . . . . .	39
21	Alternative kinematic model . . . . .	41
22	Comparison between finite element and kinematic analysis . . . . .	43
23	Development of moments in hinges A, B and C . . . . .	44
24	Assumed folding mechanism for web and plate flange . . . . .	45
25	Geometrical observations related to the folding mechanism . . . . .	46
26	Lengths of the assumed folding lines . . . . .	47
27	Assumed mechanism for the flange . . . . .	47
28	Actual folding patterns from FEA . . . . .	49
29	Moment comparison between FEA and folding mechanism . . . . .	49
30	Comparison between FEA and folding mechanism for design C03 . . . . .	50
31	Comparison between FEA and folding mechanism for design C01 . . . . .	50
32	Normalised collapse load . . . . .	52
33	Collapse of ring stiffener. Von Mises stress contour plot . . . . .	54
34	Effect of vertical stiffeners . . . . .	55
35	The effect of multiple ring stiffeners . . . . .	56
36	Linear relation between number of stiffeners and collapse load . . . . .	58
37	Column model . . . . .	61
38	Typical mesh . . . . .	62

---

39	Effect of mesh size . . . . .	63
40	Stern model with main dimensions . . . . .	64
41	Stern corner vs. 10 m rigid column . . . . .	65
42	Effect of half model . . . . .	66
43	Effect the modelled hight . . . . .	67
44	Displacement shape at the end of the analysis . . . . .	68
45	Effect of fracture . . . . .	69
46	The effect of mass scaling . . . . .	71
47	Effect of impact velocity . . . . .	72
48	Comparison between coupled and uncoupled analysis . . . . .	73
49	Overview of impact scenario . . . . .	74
50	Phases of a stern corner impact . . . . .	75
51	Collapse of A01 . . . . .	76
52	Impact force versus time . . . . .	77
53	Interface pressure on column . . . . .	78
54	Mass as a measure for strength . . . . .	79
55	Distribution of energy for design A01 . . . . .	81
56	Ring stiffener sections . . . . .	82
57	Ring stiffeners with different slenderness . . . . .	83
58	Effect of varying ring stiffener spacing . . . . .	84
59	Equal total vertical stiffener area . . . . .	85
60	Equal vertical stiffener sections . . . . .	86
61	Effect of relative position of the vertical stiffeners . . . . .	88
62	Effect of shell plate thickness . . . . .	89
63	Effect of bulkheads . . . . .	90
64	Horizontal section at 1.2 m . . . . .	91
65	Effect of deck . . . . .	91
66	Deformed bow and side after 2 m global displacement . . . . .	92
67	Comparison between stern corner, side and bow impacts . . . . .	93
68	Force distribution between forecastle and bulb in bow impact . . . . .	94
69	Force displacement in strength design . . . . .	95
70	Deformed stern after strength design impact . . . . .	96
A.1	Principal drawing of the column . . . . .	A-1
A.2	Stiffener definitions . . . . .	A-1
C.1	Stage 1 . . . . .	C-2
C.2	Stage 2 . . . . .	C-3
C.3	Stage 2 . . . . .	C-7
D.1	Kinematic model . . . . .	D-1
D.2	Calculation model for position of point B . . . . .	D-2
E.1	Lengths of the assumed folding lines . . . . .	E-1

## List of Tables

3	Material parameters (True stress strain) . . . . .	25
---	----------------------------------------------------	----

# 1 Nomenclature

Variable	Unit	Description
$E$	MPa	Youngs Modulus
$I$	mm <sup>4</sup>	Moment of inertia
$P$	N	Impact force
$\bar{P}$	-	Normalised impact force, $\bar{P} = \frac{PR}{M_P}$
$\lambda$	-	Dimensionless slenderness parameter, $\lambda = \frac{M_P}{N_P R}$
$R$	mm	Radius
$\sigma$	MPa	Stress
$\sigma_Y$	MPa	Yield stress
$\varepsilon$	-	Strain
$\varepsilon_P$	-	Plastic strain
$\nu$	-	Poisson ratio
$\rho$	kg/m <sup>3</sup>	Density of steel
$l_e$	mm	Characteristic edge length of one element
$t_e$	mm	Characteristic element thickness
$A_e$	mm <sup>2</sup>	Area of cross section including effective plate flange
$A_f$	mm <sup>2</sup>	Area of cross section top flange
$A_p$	mm <sup>2</sup>	Area of cross section plate flange
$A_w$	mm <sup>2</sup>	Area of cross section web
$N_P$	N	Plastic axial force, $N_P = A_e \sigma_Y$
$W_P$	mm <sup>3</sup>	Plastic section modulus
$M_P$	Nmm	Plastic moment, $M_P = W_P \sigma_Y$
$\mathbf{M}$	kg	Mass matrix
$\mathbf{C}$	kg/s	Damping matrix
$\mathbf{K}$	N/mm	Stiffness matrix
$\mathbf{u}$	mm	Nodal displacement vector
$\mathbf{Q}$	N	External force vector
$\Delta t_{cr}$	s	Critical timestep
$dw_i$	m	Relative deformation for the installation
$dw_s$	m	Relative deformation for the ship
$m$	kg	Mass
$a$	kg	Hydrodynamic added mass
$v$	m/s	Velocity
$E_s$	GJ	Strain energy
$W_e, \delta W_e$	GJ	External work, virtual external work
$W_e, \delta W_e$	GJ	Internal work, virtual internal work

See also appendix A for definitions of geometrical parameters.

## 2 Abbreviations

BWH	Bressan-Williams-Hill fracture criterion
RTCL	The Rice-Tracey Cockcroft-Latham fracture criterion
ALS	Accidental limit state
ULS	Ultimate limit state
FEA	Finite element analysis
NLFEA	Non linear finite element analysis
FEM	Finite element model
RS	Ring stiffener
VS	Vertical stiffener
BHD	Bulkhead



### 3 Introduction

The probability of a ship impacting an offshore installation is quite low, however the consequences of such an incident can be significant for the installation's structural integrity, stability and operability. A large impact may also lead to other accidents such as leakage of hydrocarbons and fires. For these reasons it is important to consider such events in the design.

In design codes the different scenarios that can affect the integrity of a structure is normally divided into two categories. These are the ultimate limit state (ULS) and the accidental action limit state (ALS). The ultimate limit state is the largest loading that are expected to occur with a yearly occurrence probability of  $10^{-2}$ . The structure is to be designed to withstand the ULS conditions without significant structural damage (Moan, 1994). Similarly is the probability level for the ALS conditions set to  $10^{-4}$ . The ALS loading should not give a loss of structural integrity, or safety critical equipment (DNVGL-RP-C204, 2010). After a ALS incident the structure should still be able to resist an ULS event. Design codes provide requirements on the size and speed of colliding vessels to be considered for both these categories (NORSOK-N003, 2016).

The consequences of ship impacts can be managed by three different methods. Firstly operational restrictions may be enforced on the visiting vessel. Limits can be set on the weight, velocity and manoeuvrability within the area surrounding the structure, this is often referred to as *event control*. Event control can reduce the probability and magnitude of ship impacts. The second design method is termed *indirect design*, and relates to general measures to ensure the structural integrity without directly considering the impact load. These measures can include designing with redundancy in the load carrying structures, using sufficiently ductile materials and avoid dependence on slender members with non ductile post buckling behaviour. The last method is *direct design* where the impact itself is used as a basis for the design. Loads are established based on the type of impact, and the damage is assessed in the relevant region (DNVGL-RP-C204, 2010). The direct design approach is considered herein.

In this thesis the focus have been on impact from a platform supply vessel visiting the platform. Other collision events may include impacts from tankers loading at the field, passing merchant vessels, aircrafts enroute to or from the installation, or ice-bergs (NORSOK-N003, 2016).

Circular stiffened shells are used in several different applications offshore, both as pressure vessels and as load bearing columns. Such columns are found in structures ranging from floating bridges, to offshore platforms. Most notably perhaps, is the columns of a semi submersible platform such as the Aker H3

design. Similar columns are also found in other offshore structures including monopile and tension leg platform types. In these application the stiffened shell can be subjected to ship impacts.

The current practise when a supply vessels visits an offshore rig is to position the vessel with the stern towards the installation, minimising the risk of bow impacts, and giving good access to the vessel's cargo area. This leaves the columns of the platform exposed to stern corner impacts. Figure 1 shows an example the leg of an semi submersible platform damaged by a supply vessel impact.



Figure 1: Column leg after supply vessel impact (Do Amaral Amante et al., 2008)

The column legs of a semi submersible are a critial part of both the load bearing and the flotation structure. Do Amaral Amante et al. (2008) analysed the residual buclikng strength of such a column after broad side ship impacts and found that the capacity was reduced by 9%. Hu et al. (2009) performed a similar analysis on another design and found that the residual strength is satisfactory. This shows that the current designs are well equipped to handle impacts without posing an immediate risk to the safety of the platform. Secondary effects such as water ingress and subsequent loss of stability can still lead to dangerous situations, as well as downtime and production loss.

The collapse of flat stiffened panels have been studied at great detail, and multiple analytical expressions for the resistance exists (Yu, 2017). The influence of curvature in the panel have also been studied to some extent. Johansen and Amdahl (1997) proposed a simple plastic mechanism to describe the collapse of a ring stiffener, and Spoorenberg et al. (2012) proposed a iterative method to determine the ultimate load of a circular arch. Both these methods are considered herein. In this thesis several different analytical methods, as well as finite element analyses, are used to in an effort to describe the collapse.

## 4 Energy dissipation

In all physical processes the total energy is conserved. In a ship collision the initial kinetic energy in the striking ship must be converted to strain energy and dissipated as heat. It is interesting to quantify how this strain energy is divided between the striking ship and the installation, and how much damage each vessel must undergo to dissipate all the necessary energy. Some energy will also be dissipated through other processes such as wave making, these effects are neglected in the following discussion.

The evaluation of the energy distribution have historically been based on one of four methods. These are statistical, experimental, simplified analytical methods or more recently non linear finite element analysis.

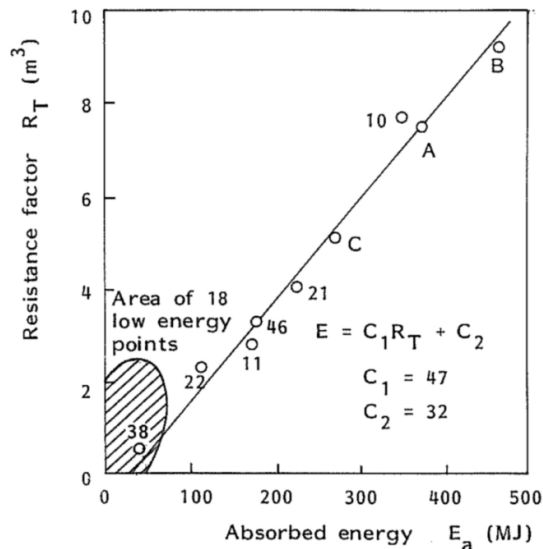


Figure 2: Correlation between dissipated energy and damaged volume in ship collisions, figure taken from Storheim (2016)

Minorsky is known for his early work on ship on ship collisions with both empirical and statistical methods. Using 26 full scale collisions reported by the U.S Coastal Guard he showed a linear connection between the energy dissipated in MJ and the volume of damaged material, the data and the resulting regression line is shown in figure 2 (Amdahl, 1983). This expression gives good results for high

energy impacts, but for lower levels the scatter is significant. In this thesis the energy levels are about 20 MJ and thereby out of bounds of Minorskys formula.

For lower energy levels simplified analytical methods may yield better results. These are often based on plasticity theory and kinematic models of the impacting bodies. In these models all deformations are assumed to be localised in yield lines, and the energy dissipated is linked to the angle which the structure rotates about these lines.

Experimental methods consisting of both full scale and model scale impacts are the most accurate methods for studying impact mechanics (Yu, 2017). The drawback of course is the need for large expensive structures that will get destroyed. Experiments like this provide important data that can be used to verify and tune analytical methods.

In recent times non linear finite element method have become the preferred tool to assess damage, due to the fact that computers have developed to the point where analyses of complete systems with a reasonable fine mesh are feasible. This method is able to predict the damage pattern with high accuracy, and is often used as virtual experiments. Simplified methods are never the less still important as a design tool, given that it allows for quick assessment of the general damage, and a better understanding of the problem at hand.

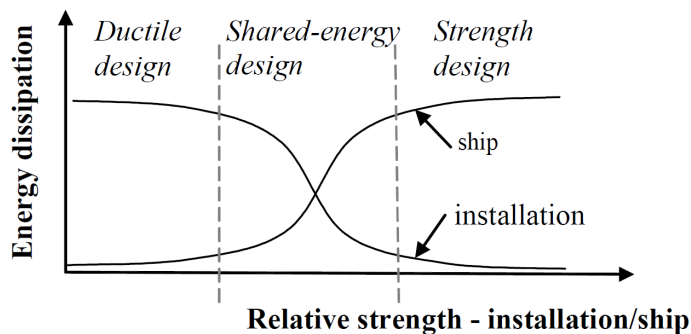


Figure 3: Design principles (DNVGL-RP-C204, 2010)

Figure 3 outlines the concepts of *Ductile design*, *Shared-energy design* and *Strength design*. These three different design principles are based on the relative distribution of strain energy. In the case of ductile design the installation is designed in such a way that most of the impact energy is dissipated in the installation, through large plastic deformations. In the strength design regime the installation

is designed to withstand the impact with only minor deformations and the impact energy will therefore have to be dissipated through deformation of the ship. In between these extremes one finds the shared-energy design philosophy where both the installation and the ship undergo some plastic deformation. In design of offshore structures it is advantageous to aim for a strength or shared-energy design DNVGL-RP-C204 (2010).

In shared energy design the distribution of strain energy, and thereby the amount of damage, can be studied using the force deformation curves. A conceptual example of such a curve is presented in figure 4. The dissipated strain energy,  $E_s$ , can be found by integrating the force over the displacement. By keeping the force level equal for both parties, one can find the force and displacement that gives the required total energy. Mathematically this can be expressed as

$$E_s = E_{s,s} + E_{s,i} = \int_0^{w_{s,max}} P_s dw_s + \int_0^{w_{i,max}} P_i dw_i. \quad (1)$$

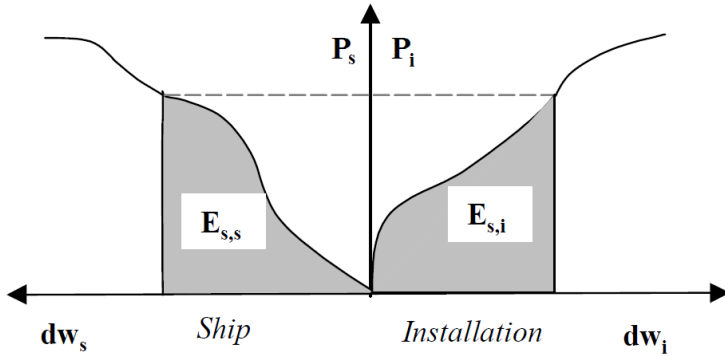


Figure 4: Conventional energy distribution (DNVGL-RP-C204, 2010)[Modified]

Depending on the type of impact the energy to be dissipated does not necessarily reflect the entire initial kinetic energy. In some impacts the striking ship retains some of its kinetic energy, and in other cases the installation may be set in motion and thereby gain kinetic energy. In DNVGL-RP-C204 (2010) the requirement for impact energy is dependent on whether the structure is fixed or compliant.

For a fixed structures the maximum impact energy to be dissipated is the entire initial kinetic energy of the impacting vessel. The energy is given by

$$E_s = \frac{1}{2}(m_s + a_s)v_s^2 \quad (2)$$

where  $m_s$  and  $a_s$  is the mass and added mass of the vessel, and  $v_s$  is the impact velocity.

For compliant installations the energy to dissipate can be taken as

$$E_s = \frac{1}{2}(m_s + a_s)v_s^2 \frac{\left(1 - \frac{v_i}{v_s}\right)^2}{1 + \frac{m_s + a_s}{m_i + a_i}} \quad (3)$$

where  $v_i$ ,  $m_i$  and  $a_i$  is the initial velocity mass and added mass of the installation. The velocity of the installation is often negligible. (NORSOK-N004, 2004)

A structure can be assumed compliant if the duration of the impact is small compared to the fundamental period of vibration of the structure (NORSOK-N004, 2004). Since the fundamental period for sway and surge of a semi submersibles is in the order of 100 s (Larsen, 2014), it is safe to use the compliant assumption.

In an accidental limit state (ALS) analysis of a stern impact the initial kinetic energy should not be taken less than 22 MJ if no operational restrictions on allowable visiting vessels are imposed (NORSOK-N003, 2016). This figure is derived from a assumed impact with a 10 000 tonne ship impacting with a velocity of 2 m/s and 10% added mass. For ULS analysis, the velocity can be taken as 0.5 m/s giving an energy equal to 1.38 MJ. In the following, only the ALS requirement is discussed.

Using a somewhat conservative estimated installation weight of 50 000 tonne and 10% added mass, equation 3 gives the energy going towards strain  $E_s = 18$  MJ. By assuming a compliant structure one can reduce the energy level by nearly 20%. In this thesis the full 22 MJ is used due to the lack of information about the structure.

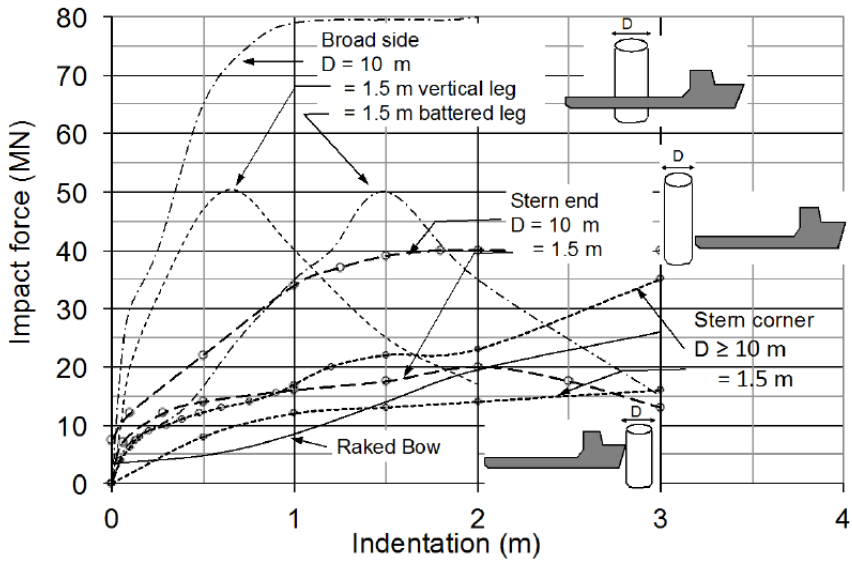
In their recommended practise C204 DNV GL presents force deformation curves for various impact scenarios. In the current document the curves are based on a 5000 tonne supply vessel (DNVGL-RP-C204, 2010). As stated earlier the current NORSOK requirement is 10 000 tonne, additionally there have been changes in the design of the supply vessel fleet since the last revision. To ensure that the recommended practice is up to date a revised version is currently being developed. The new version will include updated force displacement curves, based on analyses of a standardized supply vessel in the range of 10 000 tonnes (DNVGL-RP-C204, 2016). The old and new curves are compared in figure 5. In these curves the structure is held rigid and the striking ship follows a prescribed path with a constant velocity.

The recommended curves does not take the deformation of the installation into

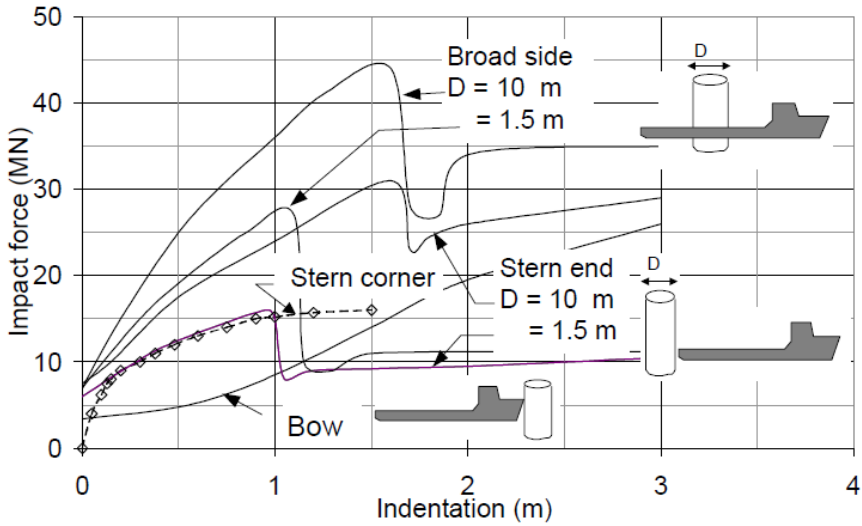
account. In practical engineering the force deformation curves is often established for the two interacting structures independently, assuming the other to be rigid. In shared energy design this is however not accurate as the deformations changes the impact area and therefore impact pressure and ultimately the resistance (Yu, 2017).

The method of analysing a constant velocity impact and later calculate the damage based on equation 1 rest on the assumption that the collision mechanism and strain energy dissipation can be decoupled. According to Storheim (2016) this distinction where first suggested by Minorsky in 1959. This decoupling is useful both in simplified energy methods, and when using non linear finite element analyses. It also gives the possibility of representing impacts with different combinations of mass and velocity by the same analysis. The inertia effects in the collision is however neglected, and accordingly the change in kinetic energy during the analysis should be verified to be negligible(DNVGL-RP-C204, 2010).

Yu (2017) showed by a full 6 degree of freedom coupled analysis that the structural damage obtained from this decoupled model might give inaccurate results, especially for small collision angles. He gave several explanations for the discrepancies, including the effect of changing added mass, varying impact angle and secondary impacts due to roll, pitch and heave.



(a) Proposed (DNVGL-RP-C204, 2016)



(b) Current (DNVGL-RP-C204, 2010)

Figure 5: Design impact force indentation curves



### 4.1 Equivalent displacement

To represent the impact by its force deformation curve a representative displacement must be chosen. The displacement in the ship and in the installation must be taken in the same location, and thereby sum to the rigid body motion of the ship. In simple cases the maximum displacement of both the structures often occur at the same location, and the choice of displacements is trivial.

However when the case gets more advanced and the relative strength of the two structures varies from location to location the deformations may not be possible to define unambiguously. This problem is illustrated in figure 6, where 6a shows a simple representation of a stern corner impact where the deformations are well defined and case 6b shows a similar impact, but now with the addition of a deck in the column. If the displacement of the two structures is measured in way of the deck, the column will seem to be in the strength design range with the ship undergoing most of the damage. If however one use the maximal deflection of both structures as a measure the total deflection will be larger than the rigid body motion of the ship and one overestimates the energy dissipated.

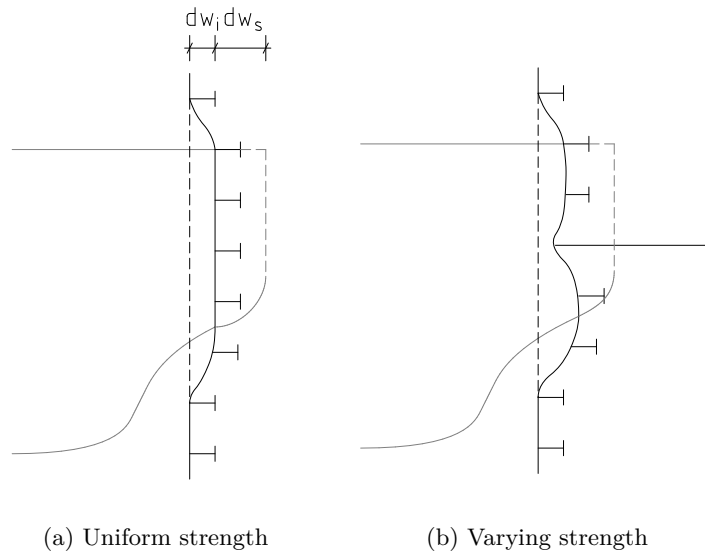


Figure 6: Varying relative resistance, dotted lines represent original shapes of the structures.

To get a better picture of the actual distribution of strain energy in a coupled analysis the plastic work done to the ship and installation can be logged through out the analysis and used as a measure for the strain energy. By logging the energy for each part, one can also get an idea on how the energy is distributed within the structures. Figure 7 shows how such an energy versus time graph may be used to determine the relative distribution of strain energy.

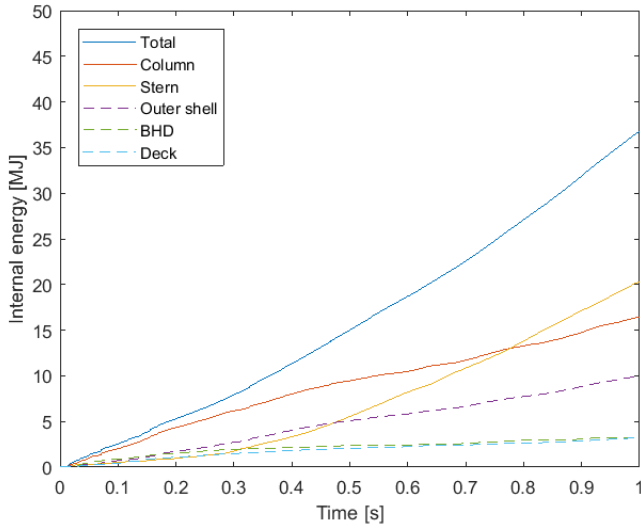


Figure 7: Strain energy versus time, parts of the column are represented by the dotted lines.

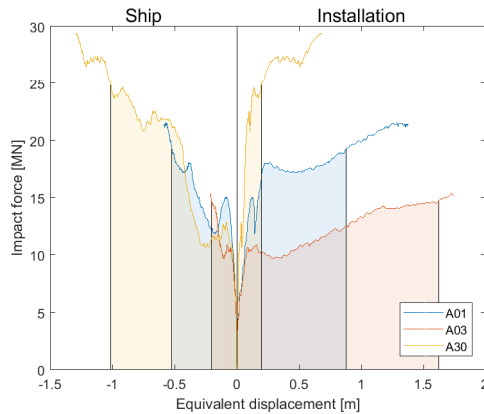
Figure 7 does not give much insight into the impact scenario as it is cumulative and therefore strictly increasing. Even though the energy distribution now is captured by the plastic work data, it is interesting to find a force deformation curve to describe the development of the impact. By utilizing the known strain energy ( $E_s$ ) and impact force ( $P$ ), it is possible to define an equivalent displacement at timestep  $t$  by rewriting the trapezoidal rule for numerical integration. The resulting expression becomes:

$$dw_{eq,t} = \sum_{i=1}^t \frac{\Delta E_{s,i}}{P_{i-\frac{1}{2}}} = \sum_{i=1}^t \frac{E_{s,i} - E_{s,i-1}}{\frac{1}{2}(P_i + P_{i-1})}. \quad (4)$$

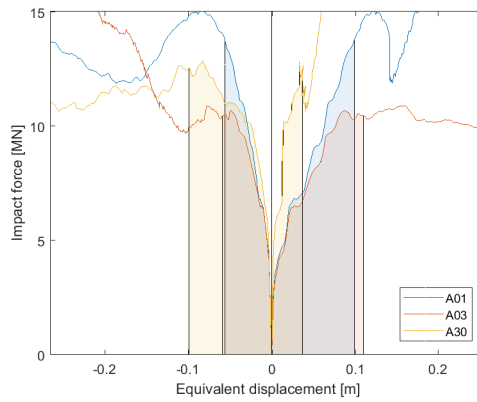
This equivalent displacement gives a force displacement curve which is consistent

with respect to both the force level and the energy. The equivalent displacements must however not be confused with a real displacement as it may differ significantly from the displacements present in the colliding bodies.

This approach is adopted for the force deformation curves herein. Examples of the resulting force deformation curves is given in figure 8. The energy requirements for the ALS and the ULS are shaded in figure 8a and 8b respectively, for three different designs.



(a) ALS criterion, 22 MJ



(b) ULS criterion, 1.38 MJ

Figure 8: Energy represented by force displacement curves

## 5 Finite element analysis

The finite element method is a power full numerical method for solving differential equations in an approximate manner. The defining characteristics of the finite element method is that the region for which the differential equation is to be solved is divided into smaller region, so called *finite elements* and the approximations are then carried out for each of these small elements rather than for the entire region (Ottosen and Petersson, 1992).

When the method is applied to structural problems the differential equation is formulated in terms of the displacements. Over a small element it is assumed that the change in the displacement is small enough such that it can be found by interpolating the displacements in discrete nodes on the boundary of the element.

A stiffness relation between the force and displacement are established on the element level, and presented in a stiffness matrix. These relations are collected in a global stiffness matrix for the whole system such that the forces working on each node ( $\mathbf{Q}$ ) can be given in terms of the global stiffness matrix ( $\mathbf{K}$ ) and the nodal displacement vector ( $\mathbf{u}$ ) in the following manner.

$$\mathbf{K}\mathbf{u} = \mathbf{Q} \quad (5)$$

The displacements can then be found by solving expression 5 for the vector  $\mathbf{u}$  either by inverting  $\mathbf{K}$  or by some numerical solving algorithm. Other interesting quantities, such as strains and stresses, are easily calculated once the displacements are found.

### 5.1 Nonlinear finite element analysis

The method of expressing the relation between the force and deformation trough a constant stiffness matrix is only valid if the system behaves linearly. This is rarely the case for accidental limit state analyses. In a nonlinear case the stiffness becomes dependent on the nodal displacements:

$$\mathbf{K}(\mathbf{u})\mathbf{u} = \mathbf{Q} \quad (6)$$

The nonlinearities in a structural problem can be classified into three main categories, geometrical, material and boundary condition nonlinearities (Cook et al., 2002). All these are important in impact analyses.

Geometrical nonlinearities are due to changes in geometry as the load history progresses. This change will affect the stiffness of the structure as well as the cross sectional areas used for stress calculations. In impact analyses the expected deformations are large, and the effects of geometrical change will be significant. The structural stiffness is expected to quickly diverge from the initial linear elastic stiffness. An example of a nonlinear geometry problem is given in section 5.1.2.

The material nonlinearities are connected with the stress strain relationship for the given material. In a linear elastic case the stress and strain is expected to follow Hooke's law.

$$\sigma = E\varepsilon \tag{7}$$

This relation is however only valid for small strains. For larger strains plasticity becomes important and the linear relation is no longer valid. Fracturing of the material is also a highly nonlinear effect that is important for the capacity at high strains. The material models used in this report is presented in detail in section 6.

Faces coming in and out of contact is considered a nonlinear boundary condition. This condition is characterised by sudden changes in stiffness which can lead to problems with convergence (Cook et al., 2002). The identification of contact area is also computationally challenging, and have to be updated for each timestep. Several contact criteria are implemented in LS-DYNA, with the kinematic constraint method as the default option. This method is briefly outlined in section 5.1.1.

### 5.1.1 Contact boundary condition

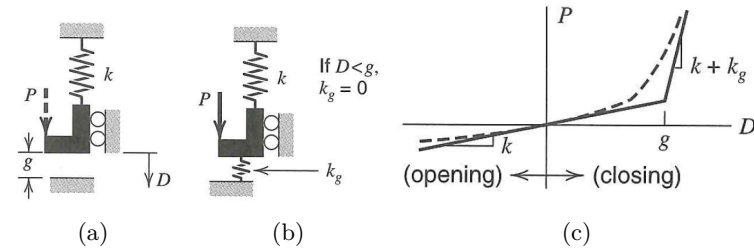


Figure 9: Penalty method for handling contact problems, (a) Mathematical problem, (b) Computational model, (c) Resulting force deformation curve (Cook et al., 2002)

The default contact criteria in the analysis software LS-DYNA is based on the penalty method (LS-DYNA Support, a). This procedure is outlined in figure 9 for a simple case of a rigid L-shaped bracket contacting a rigid surface. To represent the contact a non linear spring with stiffens given as

$$k = \begin{cases} k_g, & \text{if } D \geq g \\ 0, & \text{if } D < g \end{cases} \quad (8)$$

is placed between the two impacting bodies.  $D$  and  $g$  are given in figure 9a. The stiffness  $k_g$  is given a value large enough to prevent overclosing the gap, but not so large as to create convergence problems. The dotted line in figure 9c is sometimes adopted to aid with numerical stability. (Cook et al., 2002)

In the case presented above one knows where and when the two bodies will contact in advance, and can already from start implement the spring. In a collision analysis the exact positions of contact is impossible to determine before the analysis begins and some modifications are necessary. First one surface is designated as the master surface, and the other as the slave. At each timestep a search for slave nodes penetrating the master surface is performed. When a penetration is found a spring is placed between the the node and the master surface exerting a force proportional to the penetration depth. (LS-DYNA Support, a)

### 5.1.2 Two-bar problem

One of the simplest systems where nonlinear geometry is important is the two-bar system in figure 10a. In this problem a point load acts on two bar elements pinned to each other and to a rigid boundary. As the center point is forced down the bars have to compress to accommodate the geometrical change. This change in geometry changes the stiffness of the system, leading to a non linear system.

The resulting force deformation curve is given in figure 10b. One can observe how the stiffness reduces as the angle  $\alpha$  reduces. This is due to the geometry being such that a small increment in the deflection gives a smaller compression of the bars for a small value of  $\alpha$  than for a large. The initial stiffness from linear theory is also given on the figure as the tangent to the non-linear solution at no deformations ( $k_0$ ). It is clear that the non linear effects quickly become significant.

At one point the force reaches a maximum and further loading leads to a phenomena called snap through. Snap trough describes the sudden unloading and large deformations that happen when a local maxima of the force deformation curve is reached. The true equilibrium path will not follow the path described by the curve in figure 10b, but rather "jump" across the minimum to the next point on the curve with sufficient resistance. This will in the case of the two-bar problem mean a change from compression to tension in the bars.

This snap through phenomena can lead to problems with the numerical time integration as it happen suddenly and involve large displacements. In an analysis where the mass of the structure is considered the numerical stability is somewhat improved as the inertia effects limits the instantaneous response.

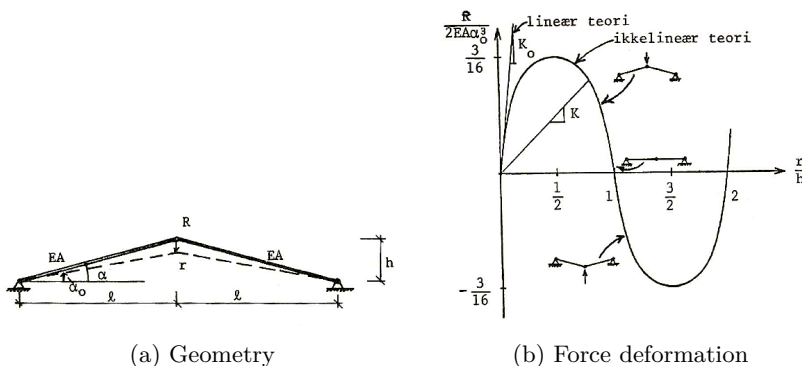


Figure 10: The two-bar problem (Bergan and Syvertsen, 1977)

## 5.2 Time integration techniques

In order to analyse a dynamic problem in the time domain it is necessary to solve the dynamic equilibrium equation given as:

$$\mathbf{M}\ddot{\mathbf{u}} + \mathbf{C}\dot{\mathbf{u}} + \mathbf{K}\mathbf{u} = \mathbf{Q}(t) \quad (9)$$

In practise this involves numerical integration of the response( $\mathbf{u}$ ) in time. The response is discretized in the time domain and the initial state is assumed to be known. There are two main ideas on how to predict the following steps, namely explicit and implicit integration procedures.

Explicit methods can generally be expressed as

$$\mathbf{u}_{n+1} = f(\mathbf{u}_n, \dot{\mathbf{u}}_n, \ddot{\mathbf{u}}_n, \mathbf{u}_{n-1} \dots) \quad (10)$$

and uses only uses information about the current timestep and previous timesteps in order to predict the next. Explicit methods are only conditionally stable, and will "blow up" if the timestep exceeds a critical value denoted  $\Delta t_{cr}$ .

In addition to the information used by the explicit methods, the implicit methods uses the equilibrium condition in the next timestep to predict the changes in acceleration. Generally the implicit methods can be given as

$$\mathbf{u}_{n+1} = f(\dot{\mathbf{u}}_{n+1}, \ddot{\mathbf{u}}_{n+1}, \mathbf{u}_n, \dot{\mathbf{u}}_n, \ddot{\mathbf{u}}_n, \mathbf{u}_{n-1} \dots). \quad (11)$$

Commonly used implicit methods are unconditionally stable, i.e. they remain stable even for large timesteps (Cook et al., 2002). The tradeoff is however that each timestep of the implicit methods are more costly.

In collision analysis the total simulation time is quite short, while the model can be large and complex. An explicit method is therefore often a good choice with many short, relatively cheap, timesteps.

### 5.2.1 Central difference method

One well used solution method is the central difference method. The analysis software used herein, LS-DYNA, uses a variation of this method (Hallquist, 2006).



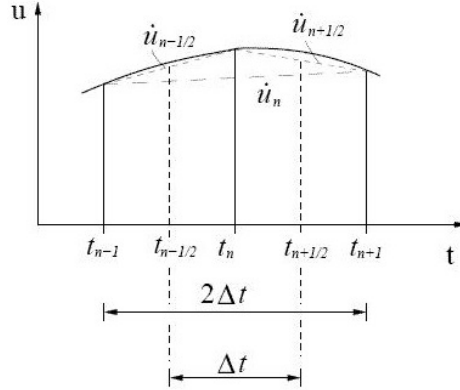


Figure 11: Discretization of the displacement

The displacements are discretised as shown in figure 11, and the current velocity and acceleration is assumed to be on the form:

$$\dot{\mathbf{u}} = \frac{1}{2\Delta t} (\mathbf{u}_{n+1} - \mathbf{u}_{n-1}) \quad (12)$$

$$\begin{aligned} \ddot{\mathbf{u}} &= \frac{1}{\Delta t} (\dot{\mathbf{u}}_{n+\frac{1}{2}} - \dot{\mathbf{u}}_{n-\frac{1}{2}}) \\ &= \left( \frac{\mathbf{u}_{n+1} - \mathbf{u}_n}{\Delta t} - \frac{\mathbf{u}_n - \mathbf{u}_{n-1}}{\Delta t} \right) \\ &= \frac{1}{\Delta t^2} (\mathbf{u}_{n+1} - 2\mathbf{u}_n + \mathbf{u}_{n-1}) \end{aligned} \quad (13)$$

Substituting equation 12 and 13 into the dynamic equation of motion (equation 9) yields:

$$\left( \mathbf{M} + \frac{\Delta t}{2} \mathbf{C} \right) \mathbf{u}_{n+1} = \Delta t^2 \mathbf{Q}_n - (\Delta t^2 \mathbf{K} - 2\mathbf{M}) \mathbf{u}_n - \left( \mathbf{M} - \frac{\Delta t}{2} \mathbf{C} \right) \mathbf{u}_{n-1} \quad (14)$$

This expression is given by the current and previous time steps, i.e. the method is of the explicit type and a stability criterion must be established.

### 5.2.2 Critical timestep

The stability criterion is established by looking at an undamped linear system. The mode shapes of the system can be found by solving the eigenvalue problem given as

$$[\mathbf{K} - \omega\mathbf{M}]\phi = \mathbf{0} \quad (15)$$

where  $\phi$  is a modal matrix of eigenvectors and  $\omega$  is the corresponding eigenvalues (Langen, 1999).

The matrix  $\phi$  can be normalized such that

$$\phi^T \mathbf{M} \phi = \mathbf{I} \quad (16)$$

$$\phi^T \mathbf{K} \phi = \omega^2 \quad (17)$$

$$(18)$$

leaving the dynamic equation of motion as

$$\ddot{\mathbf{u}} + \omega^2 \mathbf{u} = \underbrace{\phi^T \mathbf{Q}}_{=Y} \quad (19)$$

In the central difference method the acceleration is given as

$$\ddot{\mathbf{u}}_n = \frac{1}{\Delta t^2} (\mathbf{u}_{n+1} - 2\mathbf{u}_n + \mathbf{u}_{n-1}). \quad (20)$$

Substituting this expression into 19 gives the position at time  $n + 1$  as

$$\mathbf{u}_{n+1} = (2 - \Delta t^2 \omega^2) \mathbf{u}_n - \mathbf{u}_{n-1} + \Delta t^2 Y_n \quad (21)$$

or on matrix form

$$\begin{bmatrix} \mathbf{u}_{n+1} \\ \mathbf{u}_n \end{bmatrix} = \underbrace{\begin{bmatrix} 2 - \Delta t^2 \omega^2 & -1 \\ 1 & 0 \end{bmatrix}}_A \begin{bmatrix} \mathbf{u}_n \\ \mathbf{u}_{n-1} \end{bmatrix} + \begin{bmatrix} \Delta t^2 \\ 0 \end{bmatrix} Y_n. \quad (22)$$

After  $m$  steps with  $Y = 0$  the the displacement vector  $\hat{x}_m$  is given by

$$\hat{\mathbf{u}}_m = A^m \hat{\mathbf{u}}_0 \quad (23)$$

and it becomes apparent that  $A$  must be banded when  $m$  approaches infinity. It can be shown that this is the case only if the spectral radius of  $A$  is smaller than 1, giving the critical timestep as

$$\Delta t \leq \frac{2}{\omega_{max}} = \Delta t_{cr}. \quad (24)$$

In the damped case the same procedure can be used to show that

$$\Delta t \leq \frac{2}{\omega_{max}} \left( \sqrt{1 + \xi^2} - \xi \right) \quad (25)$$

where  $\xi$  is the damping ratio (Cook et al., 2002).

For a two node bar element with lumped masses, the highest eigenfrequency can be given as

$$\omega_{max} = 2\sqrt{\frac{AE}{ml_e}} = \frac{2}{l_e}\sqrt{\frac{E}{\rho}} \quad \text{for } m = \rho Al_e \quad (26)$$

where  $l_e$  is a characteristic element length (Cook et al., 2002).

Combining equation 26 and 24, and noticing that  $\sqrt{\frac{E}{\rho}} = c$  is the speed of sound in the material, gives an alternative expression for the critical timestep.

$$\Delta t_{cr} \leq \frac{l_e}{c} \quad (27)$$

This expression show how the critical timestep can be interpreted as the minimum time for which information can not propagate more than the distance between two nodes.

Unfortunately this estimate is not always conservative for shell elements and it is inconvenient to calculate the distance between all nodes in the element. It can also happen that  $\Delta t_{cr}$  is governed by flexural modes, whose natural frequency is not dependent on the nodal distances (Cook et al., 2002). To account for potential odd sized elements the characteristic length can be taken as the area of the element divided by the minimum of the longest side or the longest diagonal.

There are no available stability proofs for time integration in nonlinear problems. The current practice is therefore to use the value obtained for the linear case with a suitable safety factor.

$$\Delta t_{cr} = \gamma \Delta t_{cr,linear}. \quad (28)$$

The value of  $\gamma$  is typically 0.9 for a standard analysis (LS-DYNA, 2003).

## 6 Material models

The art of modelling material behaviour using mathematical formulations have been widely studied, and many different models have been proposed. For simple, low strain, applications the elastic model is often sufficient. In this model only the elasticity modulus ( $E$ ) is required. When the stress exceeds the elastic range the material starts to yield, and the problem quickly becomes more advanced. In the plastic region one can in some use cases conservatively assume that the stress remains at the yield level for increasing strains, in this case the material is said to behave perfectly plastic. The elastic perfectly plastic approach can both be overly conservative for some materials, and non-conservative in cases where lower resistance is beneficial. A more advanced hardening rule is therefore required.

There are in fact three important rules needed to model a material (Moan, 2003). These are:

1. *Yield criteria* which determines the state of stress for the onset of yielding.
2. *Hardening rule* which gives an expression for the changes in the yield condition as the material hardens during plastic flow.
3. *Flow rule* which describes how the plastic strain increment develops.

In addition to these one need to formulate a tensile failure criterion if the material is expected to undergo extreme deformations.

### 6.1 Yield criteria

The yield criteria determines the onset of yielding. In the one dimensional case it can simply be stated that yielding starts when the stress reaches the yield limit, often taken as the tensile yield strength (Moan, 2003). In principle the stress space is six-dimensional and thus one need a five-dimensional surface to capture the full yield surface. An often used yield criterion when working with metals is the von Mises yield criterion. This method is of the associative type where yielding is postulated to take place if the effective stress reaches a limit value (Cook et al., 2002). The effective, or von Mises, stress is given as:

$$\sigma_e = \frac{1}{\sqrt{2}} [(\sigma_x - \sigma_y)^2 + (\sigma_y - \sigma_z)^2 + (\sigma_z - \sigma_x)^2 + 6(\tau_{xy}^2 + \tau_{yz}^2 + \tau_{zx}^2)]^{\frac{1}{2}} \quad (29)$$

The yield criterion can formally be stated as

$$F = \sigma_e - \sigma_0 = 0 \quad (30)$$

where  $\sigma_0$  is the stress at which yielding should occur. This stress level starts as the yield stress of the material  $\sigma_Y$  and develops as described by the hardening rule, as the analyses progresses.

The yield criteria gives different states of stress dependent on the value

$$F < 0 \quad \text{Elastic} \quad (31)$$

$$F = 1 \quad \text{Plastic} \quad (32)$$

$$F > 0 \quad \text{Inadmissible} \quad (33)$$

i.e. the stress state will always be within (elastic) or on (plastic) the yield surface.

**6.2 Hardening rule**

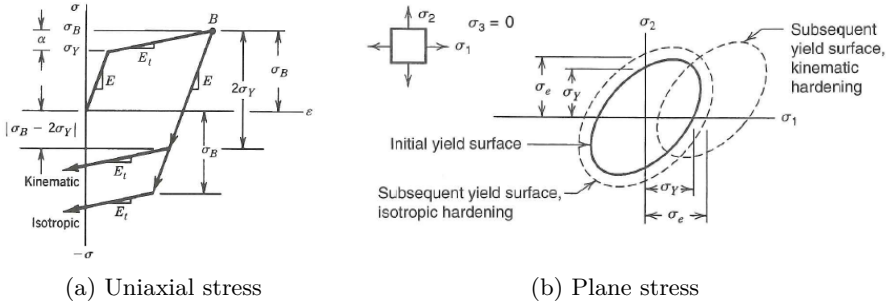


Figure 12: Kinematic and isotropic hardening models (Cook et al., 2002)

When plastic flow occur the yield surface may move or change shape. For steel and other metals this change manifests as a increase in the force deformation curve for the structure, and a rise in the yield strength. This effect is called strain hardening.

The hardening rule is best described trough an example. For a uniaxial stress state a sample follows the simplified stress strain curve in figure 12a. After yielding the stress follows a linear hardening curve with a slope  $E_t$ . When the sample reaches point B the loading is released. The stress now reduces with a slope  $E$  equal to the original elasticity. The load is then reversed and a negative stress is introduced. If yielding is assumed to occur at  $|\sigma| = \sigma_B$  the hardening is said to be isotropic. This rule is however in conflict with what is observed for common metals, where yielding is continued at a value  $\sigma_B - 2\sigma_Y$  (Moan, 2003).

This hardening rule is termed kinematic hardening. In practice the two rules may be used in combination. In figure 12b the resulting yield surfaces of the two models are presented for a case of plane stress.

The linear relationship between the plastic strain and the stress in the plastic phase depicted in figure 12a is too simple to represent real materials. In this work the rule adopted is a Hollomon type power hardening rule, extended to include a yield plateau. This rule gives the true stress as a function of the true strain and two material parameters  $K$  and  $n$ .

The hardening rule is given as

$$\sigma = K \left( \varepsilon_p + \left( \frac{\sigma_Y}{K} \right)^{\frac{1}{n}} - \varepsilon_{plateau} \right)^n \quad \text{for } \varepsilon_p > \varepsilon_{plateau} \quad (34)$$

where the parameters  $K$  and  $n$  are the hardening modulus and hardening exponent respectively (Storheim, 2016). These parameters are often given for the specific material, or they can be calculated based on the ultimate stress and the corresponding strain in the following manner,

$$n = \ln(1 + \varepsilon_{UTS}) \text{ and } K = \sigma_{UTS} \left( \frac{\varepsilon}{n} \right)^n \quad (35)$$

ensuring that the ultimate stress is the maximal stress in the engineering stress strain curve.

### 6.3 Flow rule

The strain increments are regarded to be composed of an elastic and a plastic component (Cook et al., 2002). The fundamental assumption is that these two strains are independent and can be calculated separately.

$$d\varepsilon = d\varepsilon_e + d\varepsilon_p \quad (36)$$

The elastic part of the strain is recoverable at unloading. The stress increments are associated with the elastic part of the strain through the elastic modulus as

$$d\sigma = \mathbf{E}d\varepsilon_e \quad (37)$$

When the yield function reaches the value  $F = 1$ , plastic straining occurs. This strain is not recoverable and will lead to permanent deformations of the structure.

The plastic strain increment can be given formally as

$$d\varepsilon_p = \frac{\partial Q}{\partial \sigma} d\lambda \quad (38)$$

where  $Q$  is a function with unit stress called the plastic potential, and  $d\lambda$  is termed the plastic multiplier (Cook et al., 2002). For ductile materials the function  $Q$  take the same value as the yield function  $F$ , these flow rules are called associated. The plastic flow is dependent on the stress state, the yield surface and material parameters. The partial derivative of the plastic potential gives the direction of the plastic strain increment, while the plastic multiplier scales the size of the step, as to keep the stress state on the yielding surface. The derivation of this multiplier is not practical to include herein.

## 6.4 Tensile failure

In collision analyses and other high deformation applications the tensile failure model used is important for the results. Tensile failure occurs when the material is loaded in tensile beyond its ultimate capacity and therefore fractures. In ductile materials the loaded sample often develops a small constriction at one point, and all subsequent deformations is confined here. This phenomena is termed necking (Callister and Rethwisch, 2015).

Two models were considered during the work in this thesis. The first criterion considered was the maximum principle strain. This model is adopted by DNVGL in the their recommended practises (DNVGL-RP-C208, 2016) however the limits presented is quite conservative (Storheim, 2016), and more practical values are hard to obtain. This method also gave some stability issues.

The model used in all the analyses herein is the BWH fracture criterion, extended to account for post necking damage as proposed by Storheim et al. (2015).

The BWH criterion for sheet metal instability is defined as

$$\sigma_1 = \begin{cases} \frac{2K}{\sqrt{3}} \frac{1+\frac{1}{2}\beta}{\sqrt{\beta^2+\beta+1}} \left( \frac{2}{\sqrt{3}} \frac{\hat{\varepsilon}_1}{1+\beta} \sqrt{\beta^2 + \beta + 1} \right)^n & \text{if } -1 < \beta \leq 0 \\ \frac{2K}{\sqrt{3}} \frac{\left( \frac{2}{\sqrt{3}} \hat{\varepsilon}_1 \right)^n}{\sqrt{1-\left( \frac{\beta}{2+\beta} \right)^2}} & \text{if } 0 < \beta \leq 1 \end{cases} \quad (39)$$

where  $\sigma_1$  is the major principle stress (Storheim et al., 2015).  $K$  and  $n$  are the power law hardening modulus and and exponent respectively. The variable  $\beta$  denotes the strain-rate ratio and  $\hat{\varepsilon}_1$  is the critical strain. The critical strain can be assumed equal to the power law exponent  $n$  if no measurements are

available. In course mesh applications the local stress concentrations will not be correctly captured and the criterion will predict instabilities to late. Storheim (2016) therefore implemented a geometric mesh scaling where the critical strain  $\hat{\varepsilon}_1$  is scaled with a factor  $\frac{1}{2} \left( \frac{t_e}{l_e} + 1 \right)$ , where  $t_e$  and  $l_e$  is the initial thickness and side length of the element. This geometrical scaling was proposed by Alsos et al. (2009) and is shown to better the prediction of instabilities when the mesh length is larger than the thickness of the shell.

When the BWH criterion is fulfilled a virtual neck is assumed to occur towards the principal strain axis. This necking leads to a thinning of the element which again leads to a reduction in element capacity. This reduction is included in a virtual damage defined as

$$1 - D = \frac{\exp(1 - \langle -\beta \rangle \Delta\varepsilon_1)}{1 + \frac{l_0}{t_0} [\exp(1 - \langle -\beta \rangle \Delta\varepsilon_1) - 1]} \quad (40)$$

where  $\Delta\varepsilon_1$  is the increase in the principle strain due to the necking (Storheim et al., 2015). The effect of the damage is included by replacing the stress tensor  $\boldsymbol{\sigma}$  with a effective stress tensor defined as

$$\tilde{\boldsymbol{\sigma}} = \frac{\boldsymbol{\sigma}}{1 - D}. \quad (41)$$

When a critical thickness strain is reached within the virtual neck the element is eroded. The thickness strain within the virtual neck is given

$$\tilde{\varepsilon}_3 = \varepsilon_3^0 \Delta\tilde{\varepsilon}_3 = \varepsilon_3^0 + \ln(1 - D), \quad l_0 \geq t_0 \quad (42)$$

and the erosion criterion is given

$$\tilde{\varepsilon}_{3,max} = \begin{cases} \varepsilon_3^0 (1 + \xi) & \text{if } -1 < \beta \leq 0 \\ \varepsilon_3^0 (1 + \xi (1 - \psi\beta)) & \text{if } 0 < \beta \leq 1 \end{cases} \quad (43)$$

where the parameters  $\xi$  and  $\psi$  are material parameters that can be calibrated from uniaxial tests. In lack of test data the parameters are taken as  $\xi = 1$  and  $\psi = 0.9$  as proposed by Storheim et al. (2015) for normal marine steels.



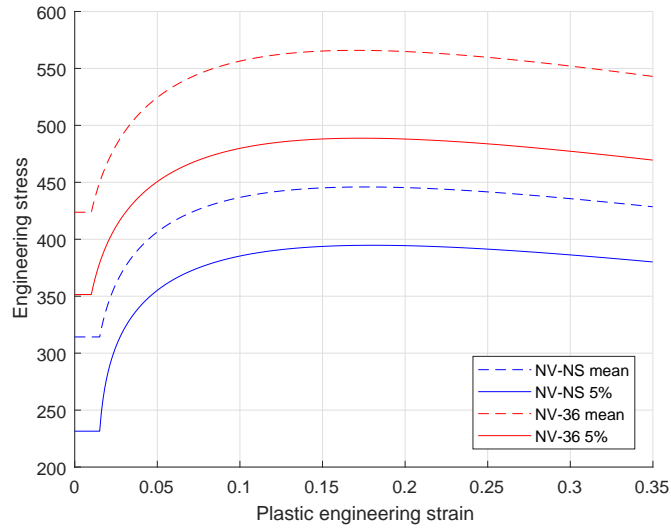
## 6.5 Material parameters

Four material models are used in the analyses herein. These models are all based on the previously discussed power law, with the hardening parameters and yield strength adjusted to give the sought after behaviour. The material parameters are chosen to represent the mean values, and a lower 5% percentile of two different commonly used offshore steels, namely normal steel(NV-NS) and high strength steel(NV-36). The mean values is used where a lower strength would be beneficial, that is in the striking ship, while the lower limit was used in the stricken installation to ensure a conservative analysis. This is in accordance with the recommendations in DNVGL-RP-C208 (2016).

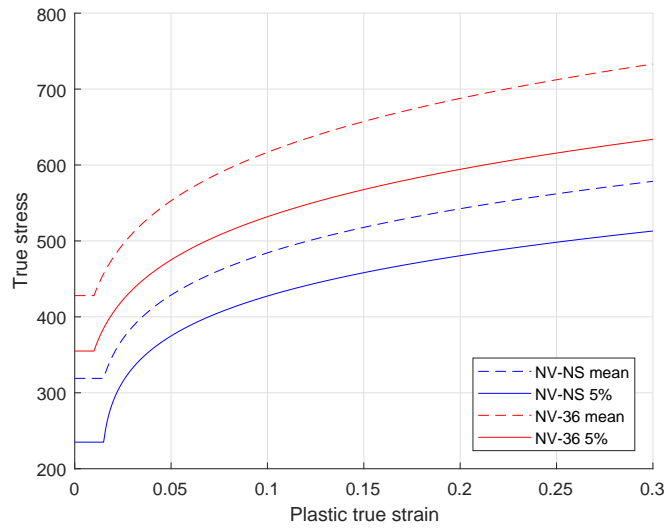
The values are based upon DNVGL-RP-C208 (2016) with some changes based on Storheim (2016) and DNVGL-OS-B101 (2003). The most notable change is that the ultimate stress for the lower curves are raised compared to the somewhat conservative values in the recommended practises. The models are presented in table 3 and figure 13a. The figure only depicts the plastic part of the curve.

Table 3: Material parameters (True stress strain)

MID Name		1 NV-NS mean	2 NV-36 mean	3 NV-NS 5%	4 NV-36 5%
E	[GPa]	210	210	210	210
$\sigma_Y$	[MPa]	319	428	235	355
$\sigma_{UTS}$	[MPa]	450	566	400	490
$\varepsilon_{UTS}$	[ - ]	0.018	0.018	0.018	0.018
$\varepsilon_{plateau}$	[ - ]	0.015	0.01	0.015	0.01
$K$	[MPa]	698.9	885.6	621.2	766.7
$n$	[ - ]	0.153	0.157	0.153	0.157
$\rho$	[t m <sup>-3</sup> ]	7.85	7.85	7.85	7.85
$\nu$	[ - ]	0.3	0.3	0.3	0.3



(a) Engineering stress strain



(b) True stress strain

Figure 13: Stress strain curves for the implemented material models

## 7 Ring stiffener collapse load

The critical load for the ring stiffeners is an important parameter when designing against ship impacts, as they are an integral part of the radial load bearing system. One important thing to note about the ring stiffeners is that the load is carried both in bending and compression, this makes them susceptible to buckling. After the critical load the geometry of the stiffener is such that the capacity reduces. This reduction is further amplified by local failures of the cross sections as the deformations become large.

In the following sections several simplified methods for determining the plastic collapse load of a ring stiffener are presented and discussed. The main motivation for doing simple methods like these are to quickly validate the design and to identify which parameters of the design that are most important.

For a real ring stiffener the boundary conditions are quite complex as it interact with the rest of the structure. By examining a full column analysis it seems like a clamped semicircular arch might be a good model to study the behaviour. The clamped support is somewhat too stiff, however the rotation in this area is neglectable in comparison with the deformation of the rest of the structure.

Spoorenberg et al. (2012) studied the collapse of circular arches with double symmetrical cross sections, and proposed a iterative solution based on a simplified yield contour and a combination of static and kinematic analysis technique. In their work a series of design curves are presented for design of circular arches. The approaches considered in the following is verified to coincide with these design curves.

### 7.1 Bound theorems

There are two distinct methods for calculating the plastic collapse load of a structure, namely static and kinematic analysis. In order to state some useful theorems regarding these methods some terms must first be defined.

1. A virtual displacement is kinematically admissible if:
  - a) Geometric compatibility between virtual displacements and rotations exist everywhere
  - b) The moment capacity in the yield hinges is equal to the plastic moment
2. A load condition is statically admissible if:

- a) Static equilibrium between external action and internal forces/moments is complied with everywhere
- b) The bending moment does not exceed the plastic moment anywhere in the structure

With these definitions the following theorems are generally true (Amdahl, 2013).

**Upper bound theorem:**

Of all kinematically admissible mechanisms will all, but the correct one, give a larger plastic resistance than the true resistance.

**Lower bound theorem:**

Of all statically admissible mechanisms will all, but the correct one, give a smaller plastic resistance than the true resistance.

**Uniqueness theorem:**

If a mechanism is both kinematically and statically admissible the calculated plastic resistance is the true plastic resistance.

The theorems are only valid for infinitesimal strains, and does therefore not give any information for large strain applications (Amdahl, 1983).

## 7.2 Slenderness

In order for a cross section to be able to develop a plastic hinge it must be compact enough to withstand the plastic moment without failing due to local buckling. The design codes Eurocode 3 (2005) and DNVGL-OS-C101 (2016) divides cross sections into four categories namely Plastic, Compact, Semi-compact and Slender. Plastic sections are able to form a plastic hinge with large rotational capacity. Compact sections will develop a plastic hinge, but have limited rotational capacity. Semi-compact and Slender section will fail before the moment reaches plastic moment and yield moment respectively. The simplest analytical methods for determining the collapse load will only be valid for cross sections of Plastic or Compact type, and even then only for small rotations. For more slender cross sections the analytical methods will present an upper bound.

Spoorenberg et al. (2012) proposed a non-dimensional slenderness parameter  $\lambda$  based on the plastic moment ( $M_P$ ), plastic normal force ( $N_P$ ) and the arch length of the analysed arch ( $S$ ). In this thesis all the analysed arches have the shape of a semicircle and therefore an arch length proportional to the radius ( $R$ ), and so the following definition for the non-dimensional slenderness parameter is adopted.

$$\lambda = \frac{M_P}{N_P R} \quad (44)$$

### 7.3 Static analysis

In this section a static analysis of a ring stiffener is performed. If one assumes that the structure is statically admissible this analysis will result in a lower bound of the collapse load as per the lower bound theorem (see section 7.1).

Take a circular arch with radius  $R$  and cross sectional parameters  $A$  and  $W_P$ . Let  $P$  be a point load in the crown of the arch (point A in figure 14).

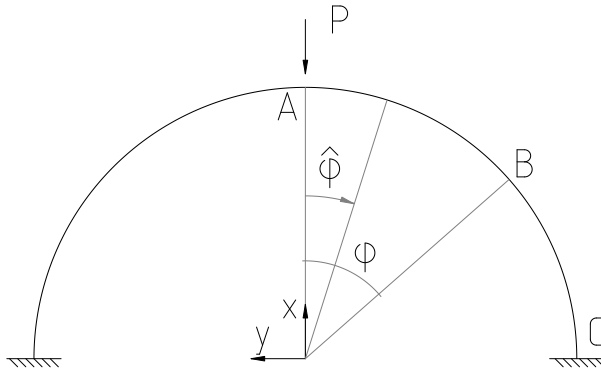


Figure 14: Idealized static problem

### 7.3.1 Elastic phase

In the first stage of loading, no yielding have occurred and the elastic solution is valid.

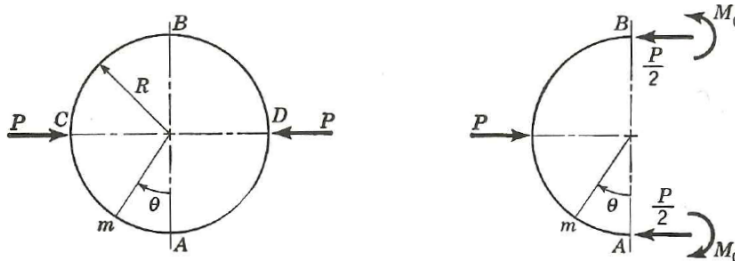


Figure 15: Ring subjected to opposing forces (Timoshenko and Gere, 1961)

Timoshenko and Gere (1961) showed how the elastic radial displacement of a circular arch can be given by the differential equation

$$\frac{d^2w}{d\theta^2} + w = -\frac{MR^2}{EI} \quad (45)$$

where  $M$  is the moment in the cross section and  $EI$  is the flexural rigidity of the curved bar in the plane of its initial curvature.

For the case of the ring subjected to two opposite but equal forces given in figure 15 they were able to show that the displacement is given

$$w(\theta) = \frac{PR^3}{4EI} \left( \cos \theta + \theta \sin \theta - \frac{4}{\pi} \right) \quad (46)$$

It is observed that the problem of the fixed arch in figure 14 can be expressed as a superposition of two instances of this solution with one rotated  $\frac{\pi}{2}$  from the other. Such that the total displacement can be expressed

$$w(\varphi) = w\left(\theta = \hat{\varphi} - \frac{\pi}{2}, P = P_A\right) + w\left(\theta = \hat{\varphi}, P = P_C\right) \quad (47)$$

where  $P_A$  is the force in point A,  $P_C$  is the radial reaction force in point C and  $\hat{\varphi}$  is an angle that is zero in point A and extending clockwise as defined in figure 14.

Given the condition that the radial displacement at  $\hat{\varphi} = \frac{\pi}{2}$  is zero one can obtain a relation between the external force  $P_A$  and the reaction forces in the supports.

The displacement in point C due to the two cases is

$$w(\hat{\varphi} = \frac{\pi}{2}) = \frac{P_A R^3}{4EI} \left( \frac{\pi}{2} - \frac{4}{\pi} \right) - \frac{P_C R^3}{4EI} \left( \frac{4}{\pi} - 1 \right) = 0 \quad (48)$$

giving the relation

$$P_C = \frac{8 - 2\pi}{\pi^2 - 8} P_A = k P_A \quad (49)$$

where  $k$  is a constant.

The full expression for the displacement can then be written

$$w(\hat{\varphi}) = \frac{P_A R^3}{4EI} \left[ \left( \sin \hat{\varphi} - \left( \hat{\varphi} - \frac{\pi}{2} \right) \cos \hat{\varphi} - \frac{4}{\pi} \right) + k \left( \cos \hat{\varphi} + \hat{\varphi} \sin \hat{\varphi} - \frac{4}{\pi} \right) \right] \quad (50)$$

The resulting displacement shape is plotted in figure 16a for some values of  $\frac{P_A R^3}{4EI}$ .

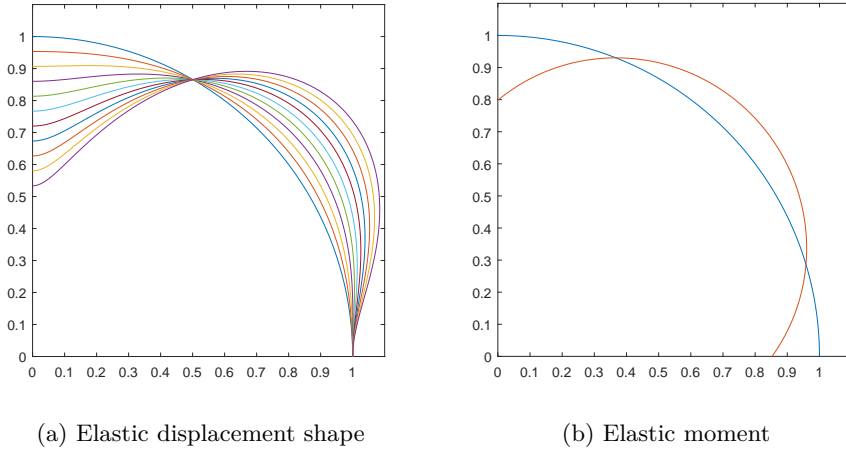


Figure 16: Results from elastic analysis

The moment in a cross section at  $\hat{\varphi}$  can be expressed

$$M(\hat{\varphi}) = \frac{PR}{2} \left[ \left( \frac{2}{\pi} - \sin \hat{\varphi} \right) + k \left( \frac{2}{\pi} - \cos \hat{\varphi} \right) \right] = \frac{PR}{2} \gamma(\hat{\varphi}) \quad (51)$$

where the function  $\gamma(\hat{\varphi})$  only is dependent on the angle. This function is plotted in figure 16b with the undeformed structure as a reference.

The initial elastic stiffness of the structure is found by solving the expression for the displacement in A with respect to the force.

The displacement in point A is

$$w_A = w(\hat{\varphi} = 0) = \frac{PR^3}{4EI} \left[ \left( \frac{\pi}{2} - \frac{4}{\pi} \right) + k \left( 1 - \frac{4}{\pi} \right) \right] \quad (52)$$

which gives the force as

$$P = \frac{4EI}{R^3} \left[ \left( \frac{\pi}{2} - \frac{4}{\pi} \right) + k \left( 1 - \frac{4}{\pi} \right) \right]^{-1} w_A = k_0 w_A \quad (53)$$

where  $k_0$  is the initial elastic stiffens.

### 7.3.2 Plastic hinges

The elastic stage ends when the largest bending moment in the structure is equal to the plastic moment. The critical load in in the first stage is then found when

$$M_{A,1} = \frac{P_1 R}{2} \gamma_A = M_P \quad (54)$$

giving that

$$P_1 = \frac{2}{\gamma_A} \frac{M_P}{R} \quad (55)$$

where  $M_P = W_P \sigma_Y$  is the plastic moment capacity and  $\gamma_A$  is the function  $\gamma(\hat{\varphi})$  given in equation 51 evaluated in A,  $\gamma_A$  takes the approximate value 0.30.

It is also noted that the moment in point B at the formation of the first hinge is given as

$$M_{B,1} = \frac{1}{2} \gamma_B P R = \frac{\gamma_B}{\gamma_A} M_P. \quad (56)$$

It is assumed that the difference in moment in point A and C is negligible, and that they fail at the same force level. It is further assumed that the contribution of shear forces can be neglected.



In the second stage of loading the moment in point A and point C is assumed to be constant equal to  $M_P$ , and thereby not able to carry any more load. The structure may therefore be studied as a three hinged circular arc. This structure is statically determinate and the moment in point B due to the further loading can be shown to be

$$\hat{M}_B = \frac{1}{2} \hat{P} R (\sin \varphi + \cos \varphi - 1) \quad (57)$$

The total moment in point B is then given as

$$M_{B,2} = M_{B,1} + \hat{M}_B \quad (58)$$

$$M_{B,2} = \frac{\gamma_B}{\gamma_A} M_P + \frac{1}{2} \hat{P} R (\sin \varphi + \cos \varphi - 1) \quad (59)$$

$$(60)$$

Inserting for  $\gamma_A = \gamma(0)$  and  $\gamma_B = \gamma(\varphi)$  from expression 51 gives the moment as

$$M_{B,2} = \frac{\left(\frac{2}{\pi} - \sin \varphi\right) + k \left(\frac{2}{\pi} - \cos \varphi\right)}{\frac{\pi}{2} + k \left(\frac{2}{\pi} - 1\right)} M_P + \frac{1}{2} \hat{P} R (\sin \varphi + \cos \varphi - 1) \quad (61)$$

The second hinge occurs when the moment reaches the plastic moment level, giving the expression

$$\frac{M_{B,2}}{M_P} = \frac{\left(\frac{2}{\pi} - \sin \varphi\right) + k \left(\frac{2}{\pi} - \cos \varphi\right)}{\frac{\pi}{2} + k \left(\frac{2}{\pi} - 1\right)} + \frac{1}{2} \frac{\hat{P} R}{M_P} (\sin \varphi + \cos \varphi - 1) = 1 \quad (62)$$

The force  $\hat{P}$  and  $\varphi$  was found by a numerical search for the lowest value of the force that satisfy this expression. The resulting values are:

$$\hat{P} \simeq 2.63 \frac{M_P}{R} \quad (63)$$

$$\varphi \simeq 0.258\pi \quad (64)$$

The load at which the hinge in B develops is then

$$P_2 = P_1 + \hat{P} \quad (65)$$

Giving the two critical loads as

$$P_{cr,1} \simeq 6.67 \frac{M_P}{R} \quad (66)$$

$$P_{cr,2} \simeq 9.30 \frac{M_P}{R} \quad (67)$$

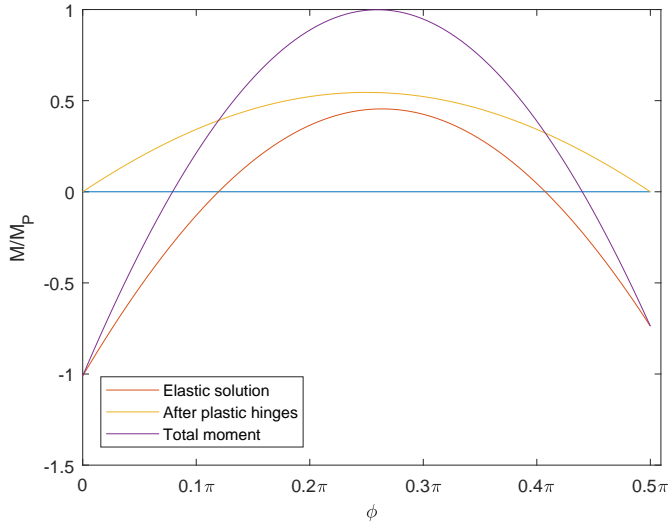


Figure 17: Total moment distribution

A normalised force parameter is introduced as

$$\bar{P} = \frac{PR}{M_P} \quad (68)$$

such that the critical loads can be written

$$\bar{P}_{cr,1} \simeq 6.67 \quad (69)$$

$$\bar{P}_{cr,2} \simeq 9.30 \quad (70)$$

The resulting moment distribution is presented in figure 17. It is observed that using this method gives the moment in C slightly lower than the plastic moment level, this is unphysical as the moment here should continue to increase with further loading. This error will lead to the model underestimating the total force.

After the development of the hinge in point B the structure collapses as a plastic mechanism, as further discussed in section 7.4. Figure 32 plots the force levels  $\bar{P}_{cr,1}$  and  $\bar{P}_{cr,2}$  and several results from finite element analysis for verification.

### 7.3.3 Reduction in moment capacity due to compression

As the cross sections are subjected to compressive stresses as well as the bending moment, the moment capacity will be somewhat reduced. The interaction between the two forms of loading is given in the following.

#### Plastic axis in plate flange

Yu (2017) presents a set of interaction equations for the case with the plastic neutral axis in the plate flange, and the axial force acting in tension. In the following it is assumed that the same arguments hold for compressive axial forces.

The reduction in bending moment can be divided into four stages:

*Stage 1: Compression in plate flange only.*

In stage one the bending capacity is not affected:

$$\frac{M}{M_P} = 1 \quad \text{for} \quad \frac{N}{N_P} \leq \frac{N^*}{N_P} \quad (71)$$

where the limiting axial force is  $\frac{N^*}{N_P} = \left(2\frac{A_f}{A_e} - 1\right)$ .

*Stage 2: Compression in plate flange and web.*

In stage two the plastic interaction is given as:

$$\frac{M}{M_P} = 1 - \frac{1}{1 + 2\frac{A_f}{A_w}} \left(\frac{A_e}{2A_w}\right)^2 \left(\frac{N - N^*}{N_P}\right)^2 \quad \text{for} \quad \frac{N^*}{N_P} \leq \frac{N}{N_P} \leq \frac{N^{**}}{N_P} \quad (72)$$

with the limiting axial force being  $\frac{N^{**}}{N_P} = \left(1 - 2\frac{A_f}{A_e}\right)$ .

*Stage 3: Compression in plate flange, web and top flange.*

In stage stage three the interaction is linear and given as:

$$\frac{M}{M^{**}} = 1 - \frac{N - N^{**}}{N_P - N^{**}} \quad \text{for} \quad \frac{N^{**}}{N_P} \leq \frac{N}{N_P} \leq 1 \quad (73)$$

where  $M^{**} = \sigma_Y A_t h_w$  is the maximum plastic bending moment from the top flange.

*Stage 4: Pure compression.*

The cross section does not have any remaining moment capacity, the axial compression have reached the level where  $\frac{N}{N_P} = 1$ .

#### Plastic axis in web

If the plastic axis is located in the web of the cross section the approach above is no longer valid. This case is less common in offshore structures but may be

found. Some of the cross sections analysed in this thesis is of this type, and thus interaction equations is needed. The derivation of these expressions is found in appendix C.

The development can be divided into different stages.

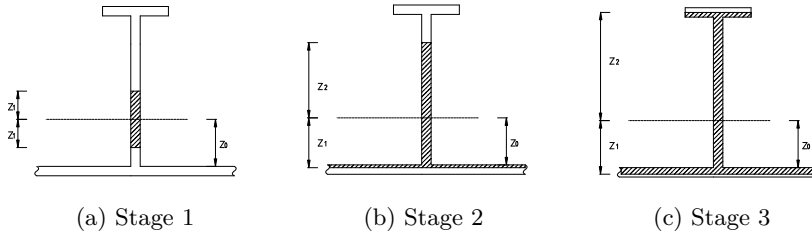


Figure 18: Stages of interaction between compression and bending. Shaded area represent the area "occupied" by the axial force. The plastic neutral axis is located a distance  $z_0$  above the plate flange.

*Stage 1: Compression in web only*

In the first stage the compression only occupy a small area in the web, symmetrically about the neutral axis. It can be shown that the interaction equation becomes:

$$\frac{M}{M_P} = 1 - \frac{A_e^2}{4t_w W_P} \left( \frac{N}{N_P} \right)^2 \quad \text{for} \quad \frac{N}{N_P} \leq \frac{\hat{N}}{N_P} \quad (74)$$

where  $W_P$  is the full plastic section modulus for the cross section, and the limiting axial force is  $\frac{\hat{N}}{N_P} = \left( 1 - 2\frac{A_e}{A_e} \right)$ .

*Stage 2: Compression in web and plate flange*

In stage two the area occupied by axial forces have reached the plate flange. The interaction equation can be expressed as:

$$\frac{M}{M_P} = 1 - \frac{A_e^2}{4t_w W_P} \left[ \left( \frac{N}{N_P} \right)^2 \left( \frac{1}{2} + \frac{t_w}{S} \right) + 2 \left( \frac{N}{N_P} \right) \left( \frac{\hat{N}}{N_P} \right) \left( \frac{1}{2} - \frac{t_w}{S} \right) - \left( \frac{\hat{N}}{N_P} \right)^2 \left( \frac{1}{2} - \frac{t_w}{S} \right) \right] \quad \text{for} \quad \frac{\hat{N}}{N_P} \leq \frac{N}{N_P} \leq \frac{\hat{N}}{N_P} \quad (75)$$

The limiting axial force is  $\frac{\hat{N}}{N_P} = \left(1 - 2\frac{A_f}{A_e}\right)$ .

*Stage 3: Compression in plate flange, web and top flange.*

The expressions for stage 3 can be determined by considering the case where the normal force partially occupies the top flange as well as the web and the plate. It can be shown that the interaction then becomes:

$$\begin{aligned} \frac{M}{M_P} = \frac{A_e^2}{4t_w W_P} \left(1 - \frac{N}{N_P}\right) & \left[ \frac{A_w}{A_e} + \frac{t_w}{w} \left(\frac{N}{N_P} - \frac{\hat{N}}{N_P}\right) \right. \\ & \left. + \frac{t_w}{S} \left(\frac{N}{N_P} - \frac{\hat{N}}{N_P}\right) \right] \quad \text{for} \quad \frac{\hat{N}}{N_P} \leq \frac{N}{N_P} \leq 1 \end{aligned} \quad (76)$$

*Stage 4: Pure compression.*

In stage 4 the cross section has lost all its moment capacity and can only carry axial force.

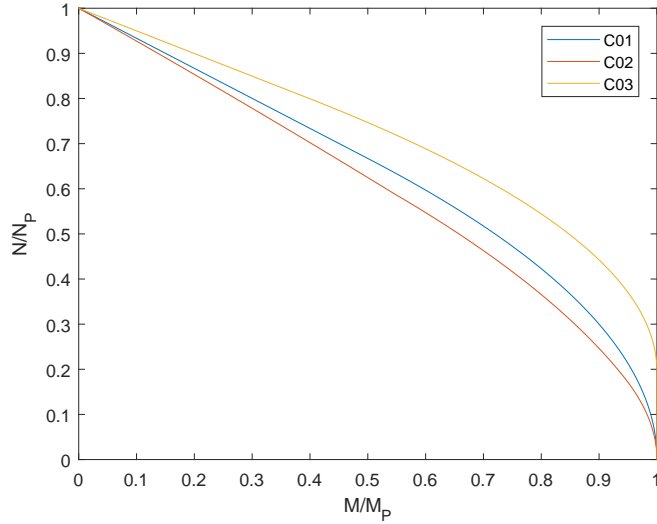


Figure 19: Interaction between moment capacity and axial force

The interaction equations presented in this section is plotted for three cross sections in figure 19. Section C01 and C03 have the plastic axis located in the plate

flange and follow the expressions given by Yu (2017), while section C02 have the axis located in the web.

The critical forces found in the static analysis (see equation 69) can now be modified to account for the compressive stress by multiplying with the fraction  $\frac{M}{M_P}$  for the appropriate level of  $N$ .

$$\bar{P}_1 = 6.67 \cdot \frac{M(N)}{M_P} \quad (77)$$

$$\bar{P}_2 = 9.30 \cdot \frac{M(N)}{M_P} \quad (78)$$

From the equilibrium condition one can find that the axial force in point A, B and C is given

$$N_A = k \frac{P}{2} \quad (79)$$

$$N_B = (k \cos \varphi + \sin \varphi) \frac{P}{2} \quad (80)$$

$$N_C = \frac{P}{2} \quad (81)$$

respectively, where  $k$  is the constant found in equation 49.

As the moment capacity is a function of the axial force  $N$  which again is a function of the impact force  $P$ , iterations is required to find the critical load. For the designs used in this thesis the effect of compressive stresses reduced the moment capacity slightly for some of the cross sections, while other retain their full capacity. The effect is included in figure 32, and shown to be of importance for slender cross sections.

## 7.4 Kinematic analysis

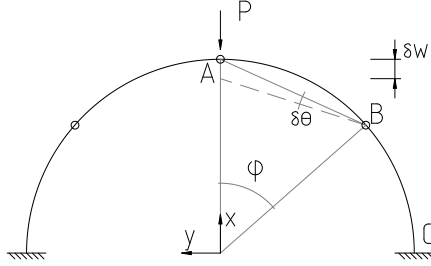


Figure 20: Kinematic model

The kinematic analysis is based on the assumption that the work done by the external forces is equal to the sum of internal work from rotation of plastic hinges and elongation or shortening of these hinges. The material is assumed rigid perfectly plastic such that all the deflection is due to the development of plastic zones. It is further assumed that the effect of shear forces is negligible in the areas where the plastic hinges forms.

In a kinematic analysis one need to establish a kinematically admissible displacement field, where all rotations and displacements are described by the same parameter. One such model was proposed by Johansen and Amdahl (1997) and is recreated in figure 20. For small displacements it is assumed that point B is stationary and that all deformations happen between point A and B. To accommodate the shortening of AB the beam is also subjected to compression forces. It is assumed that all compression takes place in the hinges. This problem turns out to be quite similar to the two-bar problem discussed in section 5.1.2.

For small angles the virtual displacement in point A can be approximated as:

$$\delta w \approx 2R \sin\left(\frac{\varphi}{2}\right) \delta\theta \quad (82)$$

and the end shortening can be given

$$\delta e \approx 2R \sin^2\left(\frac{\varphi}{2}\right) \delta\theta \quad (83)$$

The external and internal virtual work is then found as

$$\delta W_e \approx P\delta w = 2PR \sin\left(\frac{\varphi}{2}\right) \delta\theta \quad (84)$$

$$\delta W_i \approx 4M_P\delta\theta + 2N_P\delta e = 4M_P\delta\theta + 4N_P R \sin^2\left(\frac{\varphi}{2}\right) \delta\theta \quad (85)$$

Equating external and internal virtual work gives the following expression for the critical load

$$P_{cr} = \frac{2M_P}{R} \left( \frac{1}{\sin\left(\frac{\varphi}{2}\right)} + \frac{N_P R}{M_P} \sin\left(\frac{\varphi}{2}\right) \right) \quad (86)$$

Minimising the collapse load on the unknown angle  $\varphi$  gives the following expression for the critical load

$$P_{cr} = \frac{4M_P}{R\sqrt{\frac{M_P}{N_P R}}} = \frac{4}{\sqrt{\lambda}} \frac{M_P}{R} \quad (87)$$

where  $\lambda$  is the dimensionless parameter introduced in section 7.2. The angle at which hinge B will occur is given as

$$\varphi = 2 \sin^{-1}\left(\sqrt{\lambda}\right) \quad (88)$$

Introducing the dimensionless force parameter from equation 7.3.2 the force can simply be given as.

$$\bar{P}_{cr} = \frac{4}{\sqrt{\lambda}} \quad (89)$$

This expression for the collapse load is given in standards such as DNVGL-RP-C204 (2010) and NORSOK-N004 (2004). In accordance with the bound theorems this expression should be larger or equal to the true collapse load. It is shown in figure 32 that the force indeed is quite a bit higher than the results obtained using the finite element method.



7.4.1 Alternative mechanism

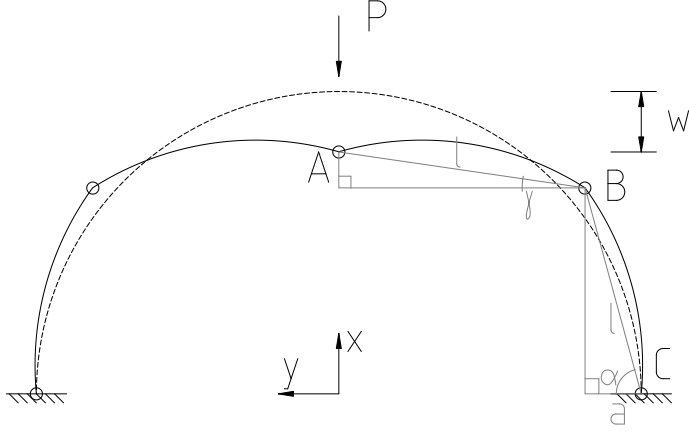


Figure 21: Alternative kinematic model

The result from the kinematic analysis is dependent on the assumed displacement field. Based on observations from the finite element analysis it seems that the assumption that point B remains stationary is quite erroneous. An alternative mechanism is presented in figure 21.

The mechanism is analysed under the assumptions that the plastic hinges can undergo deformations and still maintain the plastic moment, and that the rest of the structure remains rigid. By considering the geometry of the deformation mechanism it can be shown that the rotation in hinge A, B and C is given as:

$$\theta_A = \frac{\pi}{4} - 2\gamma \quad (90)$$

$$\theta_B = \alpha - \gamma - \frac{\pi}{4} \quad (91)$$

$$\theta_C = \alpha - \frac{3\pi}{8} \quad (92)$$

where the angles  $\alpha$  and  $\gamma$  are

$$\alpha = \cos^{-1} \left( \frac{a}{l} \right) \quad (93)$$

$$\gamma = \cos^{-1} \left( \frac{R-a}{l} \right) \quad (94)$$

The lengths  $a$  and  $l$  is marked in figure 21 and can be expressed in terms of the radius  $R$  and the deformation  $w$  in the following manner

$$l = 2R \sin \frac{\pi}{8} \quad (95)$$

$$a = \frac{1}{2}R - \frac{1}{2}(R-w) \sqrt{\frac{4l^2}{(R-w)^2 + R^2} - 1} \quad (96)$$

The expressions for the lengths and angles are derived in appendix D based on the assumption that all the deformations happen in the hinges such that the length  $l$  remains constant.

When the rotation are known the change in internal work ( $dW_i$ ) can easily be determined as the product of the change in rotation and the respective moments in the hinges.

$$dW_i = M_A d\theta_A + 2M_B d\theta_B + 2M_C d\theta_C \quad (97)$$

The change in external work is given as

$$dW_e = Pdw \quad (98)$$

and must be equal to the change in internal work, giving the relation

$$P = \frac{dW_i}{dw} \quad (99)$$

If one assumes that the moment capacity in all three hinges are equal to the plastic moment the critical force reads

$$P = \frac{d\theta_A + 2d\theta_B + 2d\theta_C}{dw} M_P \quad (100)$$

By noticing that  $\theta_B = \frac{1}{2}\theta_A + \theta_C$  the expression can be simplified to

$$P = \frac{4d\theta_B}{dw} M_P \quad (101)$$

or on normalised form

$$\bar{P} = 4R \frac{d\theta_B}{dw} \quad (102)$$

The resulting force deformation for design C03 is presented in figure 22a, together with the same curve from a finite element analysis. In figure 22b the dissipated energy is plotted against the displacement.

For strength design the most important parameter is the collapse load, i.e. the maximal impact resistance. The analytical solution is not easily found due to the complexity of the kinematic model, however a computer search gives that the normalised force have a constant value for all R of about:

$$\bar{P}_{cr} \simeq 9.657 \quad (103)$$

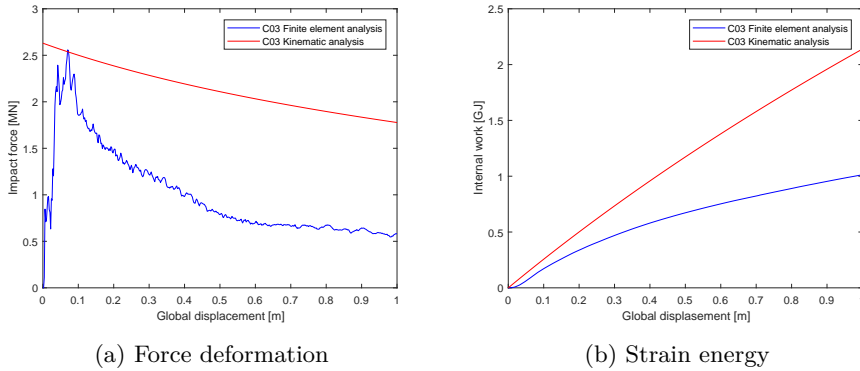


Figure 22: Comparison between finite element and kinematic analysis

The kinematic model gives a reasonable estimate for small displacements, and thereby the maximal load, but for larger displacements the actual value drops. The reason for this drop is a loss of moment capacity in the hinges due to local buckling. The development of the moment capacity for design C03 is plotted in figure 23. It can be observed that hinge C remains at the plastic level even for large displacements, this is due to the fact that the rotation is fairly limited

and that the top flange is in tension. In hinge B the moment never reaches the plastic level, and instead fails due to a local folding mechanism, this is further discussed in section 7.4.2. Hinge A can withstand the plastic moment for small displacements, but fail when the rotations becomes to large.

Regarding the Eurocode 3 (2005) classifications mentioned in section 7.2 the cross section in design C03 can be taken to be of class 4, which is recognised by the failure of the compression elements before the moment reaches the level of first yield. The limits from the design code does also place the cross section in this class.

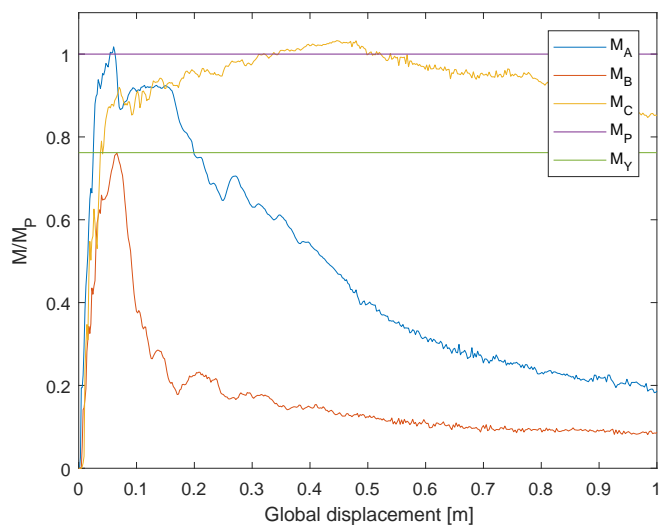


Figure 23: Development of moments in hinges A, B and C

## 7.4.2 Folding mechanism

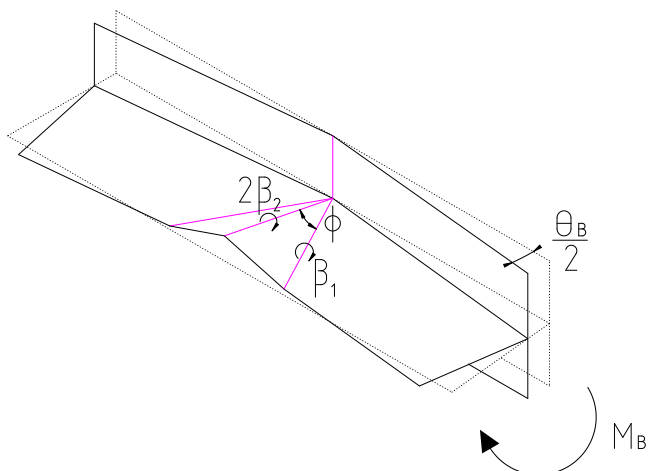


Figure 24: Assumed folding mechanism for web and plate flange

In hinge B the web and flange of the ring stiffener is subjected to compression and a may fail due to local folding rather than forming a plastic hinge. The folding mechanism assumed is given in figure 24 for a section of the shell plate and the ring stiffener web. It is assumed that four folding lines occur (marked in pink), one along the height of the shell plate, one across the web and two diagonals forming an angle  $\phi$  with the center fold. All deformations are assumed to located in these yield lines.

In order to analyse the folding mechanism an expression correlating the rotation of the cross section  $\theta_B$  and the local angles  $\beta_1$  and  $\beta_2$  is needed. In figure 25 some geometrical observations are shown. The triangles on the left is in the plane of the web, with the long side being at the center folding line, and the hypotenuse following the diagonal folding line.

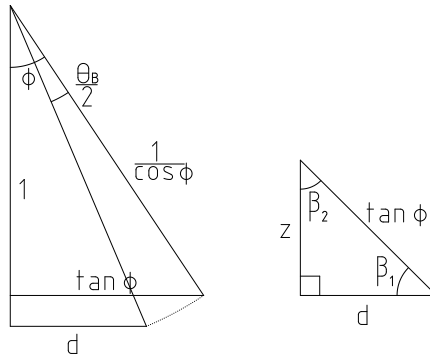


Figure 25: Geometrical observations related to the folding mechanism

The distance  $d$  will then have the length:

$$d = \frac{\sin\left(\phi - \frac{1}{2}\theta_B\right)}{\cos(\phi)} \quad (104)$$

The triangle on the right in figure 25 follow the outer vertical edge of the folding shape in figure 24. Given that the original length of the hypotenuse remains unchanged the local angles in the yielding lines are

$$\cos(\beta_1) = \frac{\sin\left(\phi - \frac{1}{2}\theta_B\right)}{\sin(\phi)} \quad (105)$$

$$\beta_2 = \frac{\pi}{2} - \beta_1 \quad (106)$$

The absolute value of the change in the hinge line angles due to the change in rotation of the cross section are observed to be equal for the two lines:

$$\Delta\beta = \Delta\beta_1 = \Delta\beta_2 \quad (107)$$

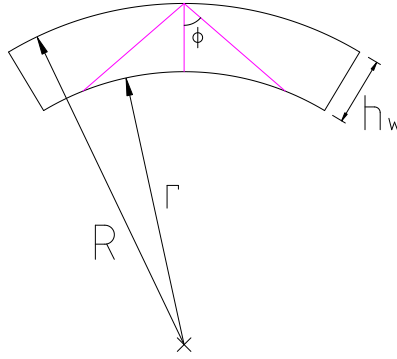


Figure 26: Lengths of the assumed folding lines

The lengths of the yield lines are found by considering the geometrical model in figure 26. The center line have the same lengths as the web height ( $h_w$ ), and it can be shown that the length of the diagonal lines can be written as

$$l_{diag} = R \left( \cos(\phi) - \sqrt{\left(\frac{r}{R}\right)^2 - \sin^2(\phi)} \right) \quad (108)$$

for angles small enough such that the yield line intersects the flange, see appendix E for detailed calculations.

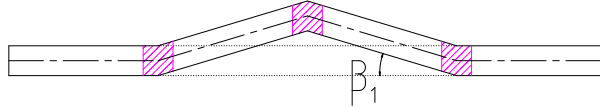


Figure 27: Assumed mechanism for the flange

The flange is assumed to form the three point mechanism in figure 27, with all deformations located at three plastic zones. The energy absorbed by a small deformation can be written:

$$\Delta W_{flange} = 4M_{P,flange} \Delta\beta = t_f w^2 \sigma_Y \Delta\beta \quad (109)$$

The internal work done by a small deformation in the web and plate flange is

given

$$\Delta W_{web} = 2M_{0,web} (h_w + l_{diag}) \Delta\beta \quad (110)$$

$$\Delta W_{plate} = M_{0,plate} S \Delta\theta_B \quad (111)$$

respectively. Where  $M_0 = \frac{1}{4}t^2\sigma_Y$  is the moment necessary to rotate a unit length of a yield hinge.

The work needed to rotate the entire hinge a small angle  $\Delta\theta_B$  is given in terms of the external moment

$$\Delta W_{B,ext} = M_B \Delta\theta_B \quad (112)$$

or as a sum of all the internal work components

$$\Delta W_{B,int} = \Delta W_{web} + \Delta W_{flange} + \Delta W_{plate} \quad (113)$$

Equating the external and internal work gives the following expression for the external moment

$$M_B = \left( \left[ \frac{1}{2}t_w^2 (h_w + l_{diag}) + t_f w^2 \right] \frac{\Delta\beta}{\Delta\theta_B} + \frac{1}{4}S t_p^2 \right) \sigma_Y \quad (114)$$

where  $\Delta\beta$  is the change in the angles  $\beta_1$  and  $\beta_2$  due to the change in  $\theta_B$ .

This expression is still dependent on the unknown angle between the yield lines. The expression for the internal work was therefore minimised numerically with respect to  $\phi$ . Different cross sections yielded different optimal angles. Cross sections with wide top flanges gave large values such that the rotations are kept to a minimum, while for sections with smaller flanges the effects of the web is more important and the angle tends towards lower values.

A picture of the folding mechanism obtained using finite element analysis is included in figure 28. The folding lines are visualized by highlighting the effective plastic strain. A figure of a analysis with vertical stiffening is also included to demonstrate how the angle between the yield lines are limited by the stiffeners.

The calculated moment and the moment found from a finite element analysis is given in figure 29. The general shape of the two curves coincide well, however the folding mechanism does not take any initial deformations into account which results in an offset in displacement between the predicted moment and the moment measured. The elastic moment is included in the figure. It is observed that the intersection between the elastic moment and the moment obtained from the folding mechanism happen for a lower moment level than what is found in the FEA. This is probably due to the mechanism not taking any elastic deformation into account.



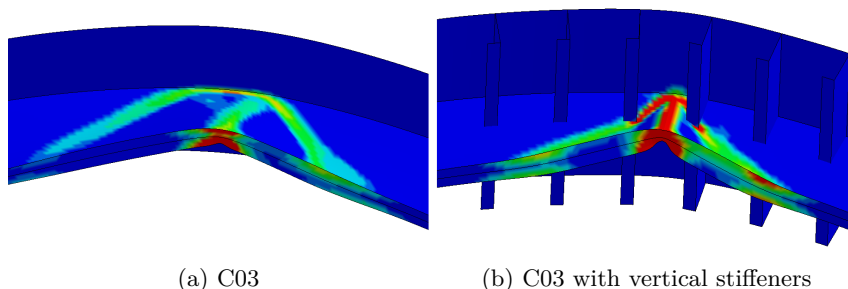


Figure 28: Actual folding patterns from FEA

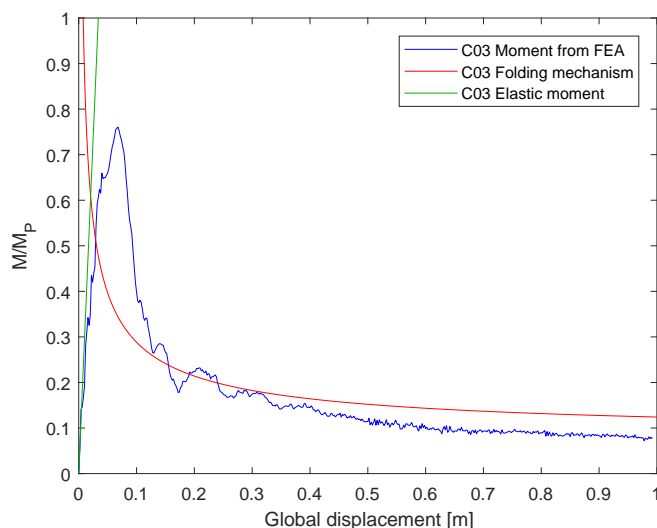


Figure 29: Moment comparison between FEA and folding mechanism

Huang and Wierzbicki (1993) proposed a similar folding mechanism under different assumptions. The resulting expressions give quite similar moments for the same global rotation even though the local geometry is somewhat different. This goes to show the strength of the plastic mechanism method.

The force displacement function for the mechanism is updated to include the effect of folding in hinge B, the result is plotted in figure 30a. The discrepancy between the model and the measured force at large deformations are probably

mainly due to the loss of moment capacity in hinge A and the change in loading pattern as the flat impactor contacts the arch away from the center point. The elastic solution found in section 7.3 is also included.

For more slender cross sections the effect of local folding becomes increasingly important. The same analysis as described above have been performed for cross section C01, the results are presented in figure 31.

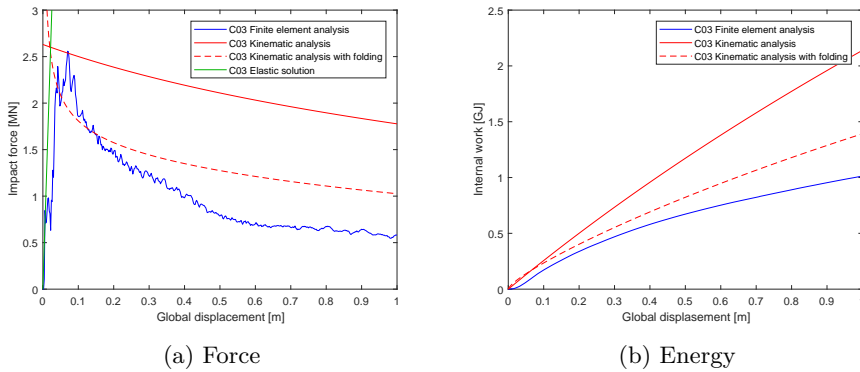


Figure 30: Comparison between FEA and folding mechanism for design C03

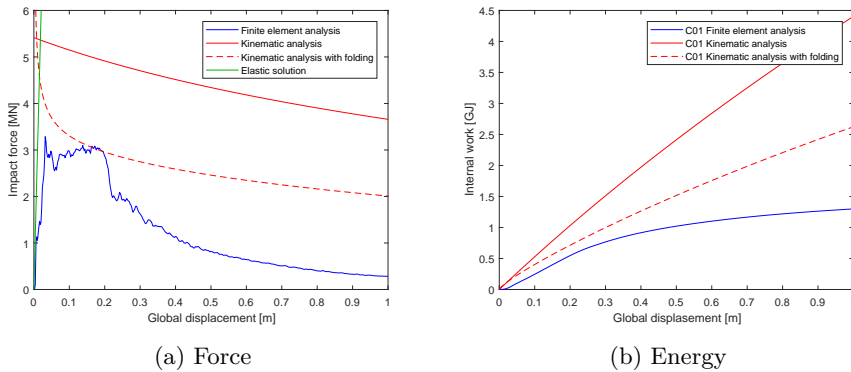


Figure 31: Comparison between FEA and folding mechanism for design C01

## 7.5 Verification using finite elements

The simplified methods for determining the critical load for the ring stiffener is verified by performing several finite element analyses of various circular arches consisting of one ring stiffener including the plate flange. The load was introduced by a flat rigid plate moving with constant speed. This will result in a somewhat different load condition than used in the simplified analyses, especially for large displacements. For small displacement however, this approach should give comparable results. The use of a flat plate instead of a more concentrated load is to reduce the stress concentration in the impact area. It is also observed from the full scale analysis that the stern corner used deforms at a quite low impact force and presents a flat impact area.

The arch was fully constrained in all directions and rotations at each end point. All nodes along the edges of the plate flange was restricted in the vertical direction to simulate the presence of the rest of the structure. This last measure proved necessary due to the arch failing in an out of plane buckling mode if it was not prevented.

For these analyses the mesh was refined to a global mesh edge length of 25 mm giving about 6 elements across the flange and 26 across the web. The influence of mesh size was investigated prior to the analysis and it was found that the critical load changed insignificantly for mesh sizes smaller than about 50 mm. Due to the simplicity of the model, the use of such a fine mesh did not result in significant use of computational resources.

The model used consist of three parts, the plate flange, the web and the top flange. All three parts are represented by shell elements. The different arches are denoted with the prefix C, dimensions for the respective designs can all be found in appendix A.

The maximal load from all the finite element analyses is plotted in figure 32 together with the analytical method discussed herein. The static analysis gave rise to the lines for the first and last hinge as described in section 7.3. The dotted line represent the formation of hinge 2 if correction of the moment capacity due to compression is used. As this factor is dependent on several parameters other than  $\lambda$  the correction has been calculated for all the cross sections independently. Mechanism 1 is the mechanism behind the collapse formulae currently used in the recommended practice (DNVGL-RP-C204, 2010), as presented in section 7.4. Mechanism 2 is the alternative mechanism developed in this work, the derivation of which can be found in section 7.4.1.

Four points from the designs curves proposed by Spoorenberg et al. (2012) is included in figure 32 as a reference.

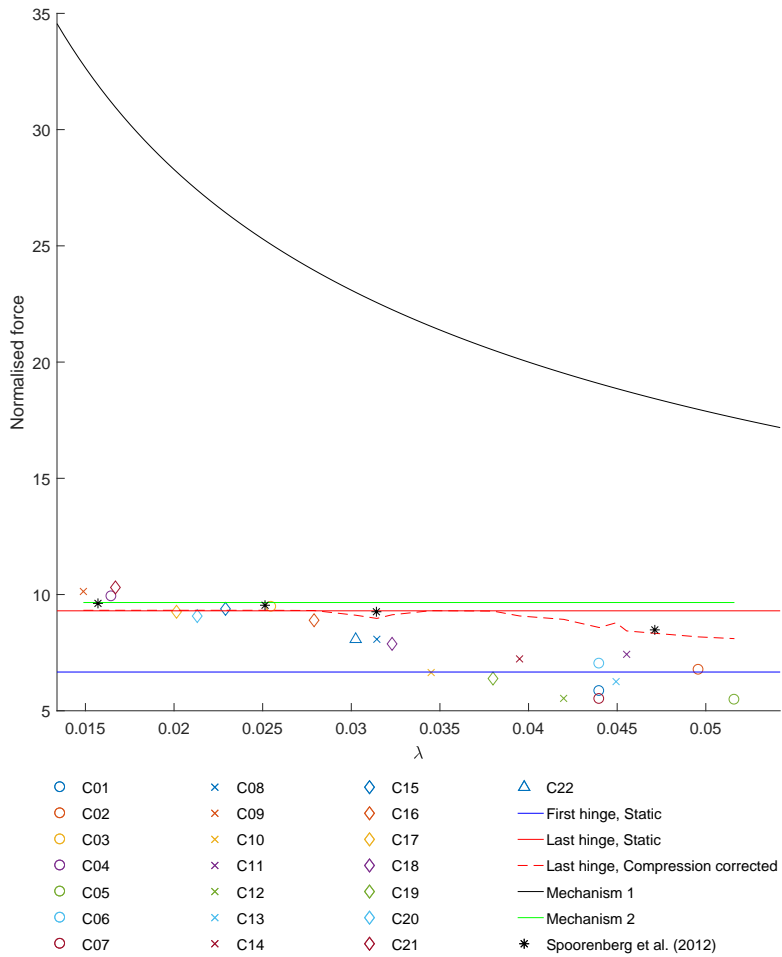


Figure 32: Normalised collapse load

With reference to the bound theorems one would expect the static analysis to under estimate the collapse load, while the kinematic models over estimates. Some few stocky designs exceeds the level predicted by mechanism 2. The common factor for these is that they have an increased shell plate thickness, which reduces the the tendency of hinge A to fail due to local effects. The delayed failure of point A may have increased the effect of strain hardening which is represented in the finite element analysis, but not in the analytical models.

The collapse loads of the different designs are plotted with the dimensionless slenderness parameter  $\lambda$  introduced in section 7.2 along the horizontal axis. There seem to exist a limit value of this parameter ( $\lambda_{lim}$ ), for which the analyses with a larger value are not able to reach the force level necessary to develop the last hinge. This limit has a value of about  $\lambda_{lim} = 0.03$ .

The collapse of the ring stiffeners as seen in the finite element analysis is presented in figure 33. The Von Mises stress fringe levels are scaled for each frame to give a better picture of the stress concentrations, the stress levels are thus not comparable between figure. The force displacement curve for this impact can be found in figure 22a, the development of the moment in the different hinges are plotted in figure 23. The frames are captured at three points that proved interesting for the collapse. The first frame is from the maximal impact force, note how the stress level associated with yielding have not completely covered the hinge in point B. The next frame is for a state where the cross section in point B have collapsed due to buckling of the flange, but there are still some capacity in point A. In the last frame the plate flange in point A buckles and the capacity of the plastic hinge reduces significantly.

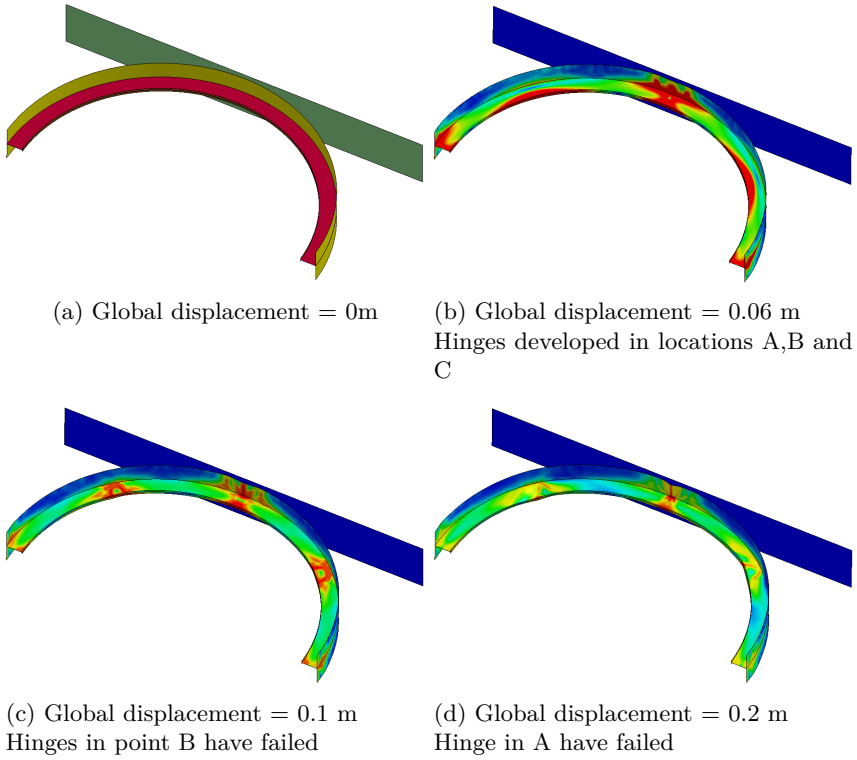


Figure 33: Collapse of ring stiffener. Von Mises stress contour plot

## 7.5.1 Influence of vertical stiffeners

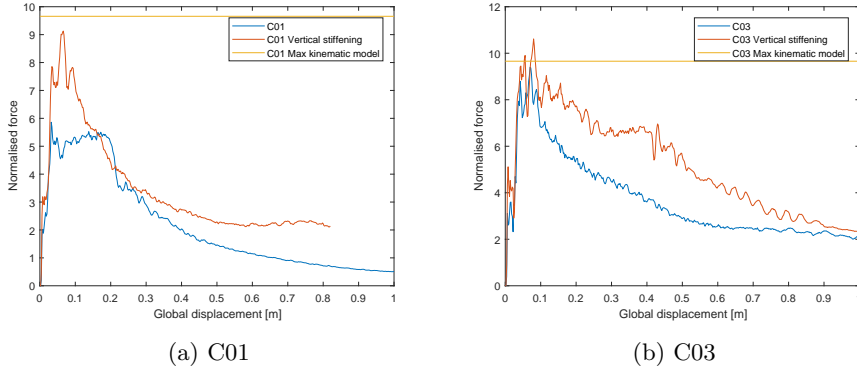


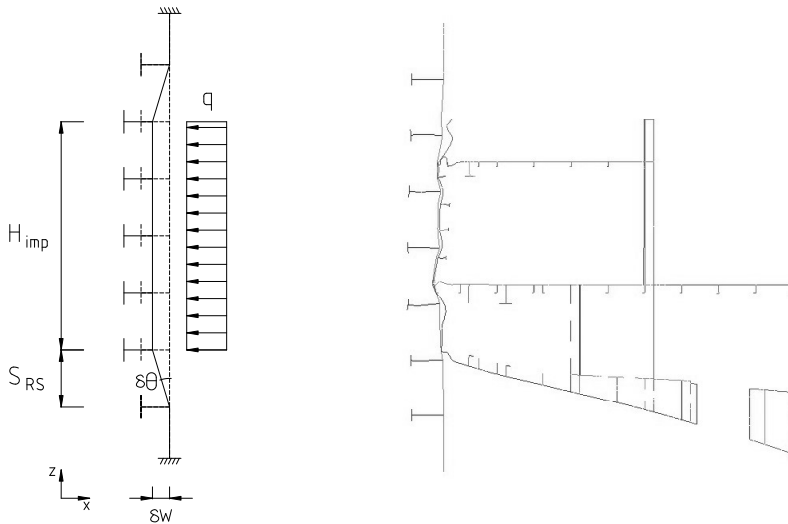
Figure 34: Effect of vertical stiffeners

In the previous analysis it became apparent that tripping of the ring stiffener contributed significantly in the reduction of the capacity. The vertical stiffeners in the column might help prevent this mode of failure by restraining the vertical displacement of the ring stiffener web. To test this hypothesis an analysis of the ring stiffener design C01 was performed with vertical stiffening similar to design A01, the results of which can be found in figure 34a. The addition of the vertical stiffening does in fact postpone the onset of the tripping in this case and allows the plastic hinge to form in point B. The vertical stiffeners also limits the local buckling of the web in point A, and thereby limits the loss of moment capacity.

The same analysis was performed with the ring stiffener cross section from design C03, this result is given in figure 34b. This cross section is able to carry the plastic moment for small rotations. The addition of vertical stiffeners therefore have limited effect on the maximum load capacity, however it limits the rate of which the force decays in the post failure region.

## 8 Collapse of the three dimensional column

In an effort to describe the effect of multiple ring stiffeners and the upper and lower boundary, the model in figure 35 is proposed. The ring stiffeners are assumed to displace the same distance and thereby carry the same load. The loading from the ship is simplified to be a line load with intensity  $q$  working over the height  $H_{imp}$ . The extent of the loaded area is further discussed in section 10.2



(a) Simplified model

(b) Section through center from FEA

Figure 35: The effect of multiple ring stiffeners

Using this model it can be found that the virtual external work is expressed as:

$$\delta W_e = qH_{imp}\delta w \quad (115)$$

while the internal work is

$$\delta W_i = nP_{cr,RS}\delta w + 4mM_{P,VS}\delta\theta \quad (116)$$

where  $n$  and  $m$  is the number of deformed ring stiffeners and vertical stiffeners



respectively. Assuming small angles this can be rewritten to

$$\delta W_i = nP_{cr,RS}\delta w + 4mM_{P,VS}\frac{\delta w}{S_{RS}} \quad (117)$$

where  $M_{P,VS}$  is the moment resistance of the vertical stiffeners and  $P_{cr,RS}$  is the critical load for the individual ring stiffeners as found in section 7.

The number of deformed ring stiffeners  $n$  can be approximated with the expression

$$n = \left( \frac{H_{imp}}{S_{RS}} + 1 \right) \quad (118)$$

Equating the internal and external energy gives the following expression for the global collapse load

$$P_{cr} = qH_{imp} = \left( \frac{H_{imp}}{S_{RS}} + 1 \right) P_{cr,RS} + 4m\frac{M_{P,VS}}{S_{RS}} \quad (119)$$

On normalised form this expression becomes:

$$\bar{P}_{cr} = \frac{P_{cr}R}{M_{P,RS}} = \frac{H_{imp}}{S_{RS}} \left( \bar{P}_{cr,RS} + \frac{4mR}{H_{imp}} \frac{M_{P,VS}}{M_{P,RS}} \right) + \bar{P}_{cr,RS} \quad (120)$$

For the designs analysed in this thesis the plastic modulus for the vertical stiffeners is significantly lower than for the ring stiffeners, and the actual moment capacity of vertical stiffeners are probably even lower than the plastic modulus would suggest due to local effects. The term regarding vertical stiffeners is as an estimate neglected, leaving the expression:

$$\bar{P}_{cr} \simeq \frac{H_{imp}}{S_{RS}} \bar{P}_{cr,RS} + \bar{P}_{cr,RS} \quad (121)$$

To verify this expression for the collapse several analyses with varying ring stiffener spacing and three different ring stiffener sections is plotted in figure 36. A linear fit is constructed for each of the cross sections and plotted in the same figure. The data points marked with a blue star have the same ring stiffener dimensions as design C01, while the red and green points have the same dimensions as C03 and C08 respectively.

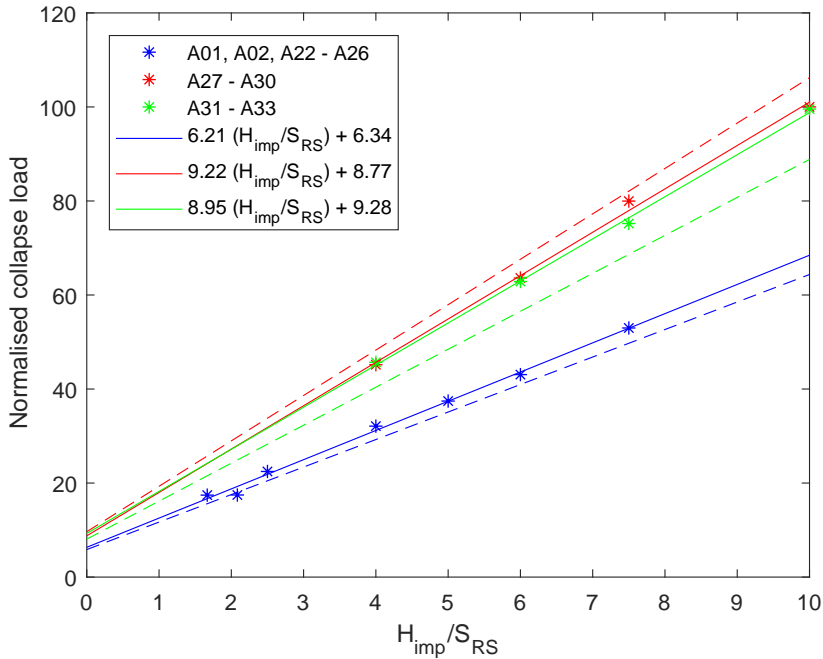


Figure 36: Linear relation between number of stiffeners and collapse load, the dotted lines represent the simplified model

From the analysis done in section 7.5 the ring stiffener collapse load for these designs are:

$$\bar{P}_{RS,C01} = 5.85$$

$$\bar{P}_{RS,C03} = 9.66$$

$$\bar{P}_{RS,C08} = 8.08$$

Comparing these values to the values for the linear expressions in figure 36 it lends credence to the expression given in equation 121. The dotted lines in the plot represents the simplified model using the ring stiffener collapse load. It is noted that the collapse load for design C03 is about the theoretical maximum obtained using the kinematic approach in section 7.4.1, the red dotted line does therefore represent the line one obtains if this value is used.

For the analyses marked in green and blue the model slightly underestimates the collapse load. This may be because the ring stiffeners have a relatively high value of  $\lambda$ , and thus fail due to local effects. The vertical stiffeners have previously been shown to prevent local failure of the ring stiffener web, and when this effect is not accounted for one underestimates the strength.

The impact height have been taken to be 6 m for most of the designs. This is slightly more than the initial impact height at 5 m, however the stern corner deforms quickly to the level where the contact surface covers a height of 6 m. For the three designs with the lower  $\frac{H_{imp}}{S_{RS}}$ -ratios the total load did not surpass the force level needed to deform the stern corner. For these the initial height of 5 m where therefore used.

In this model the effect of vertical stiffeners are excluded. From further analyses it becomes apparent that this simplification is erroneous, in that the presence of vertical stiffeners greatly influences the collapse forces. The effect of vertical stiffening is discussed in section 10.5.

## 9 Finite element model

The finite element model used to conduct the analyses in this thesis consist of a column model, an impacting ship part, a material model and a set of analysis control parameters. For most of the analysis the impacting ship part is the stern corner of a supply vessel. The stern and column models are further described in this section.

The material model describes how the material deforms during loading and is an essential part of the element analysis. The model used is an implementation of the power law model discussed in section 6 with isotropic hardening. The failure criteria used is the BWH failure criteria as discussed in section 6.4. The implementation is done by Storheim et al. (2015).

The sensitivity of the results with regard to the most important control parameters are discussed in the following sections.

### 9.1 Column model

The column model developed in this work consist of an outer shell, vertical stiffeners, ring stiffeners, decks and bulkheads. The column shell is assumed to be perfectly circular, with evenly spaced stiffeners. The ring stiffeners are assumed to be larger than the vertical stiffeners, such that the vertical stiffener intersects the web of the ring stiffener. In the intersection the web of the vertical stiffener is fixed to the web of the ring stiffener, while the flange is free to move. This resembles a cut out, as one often find in ships and offshore structures. The bulkheads are both vertically and horizontally stiffened, and can be given an arbitrary location in the model. The decks are stiffened in the x direction with evenly spaced stiffeners terminating in a continuous circular flange.

The column was modelled in *Patran 2012*. The geometry definition, meshing and property assignment were all automated by utilizing Patran Command Language(PCL). All model parameters are collected in a separate input file, making the task of altering the model trivial. This feature is essential when one wants to explore the effects of varying the parameters.

All the column designs were given a unique identifier with the prefix A followed by a two digit number. The dimensions for these can be found in appendix A. The original design (A01) is largely based on drawings of a real column leg of a semi submersible platform. The remaining designs are variations of this to investigate the effect of different parameters. Some of the designs have dimensions that would be impractical in a real construction due to other concerns such as the availability

of odd sized plates and stiffeners for production, as well as maintenance and use of the facility. These dimensions are however beneficial in this work as they give the opportunity to study the effect of changing one parameter while keeping other quantities like area and stiffness constant.

All edges, but the upper one, is restricted in all translational degrees of freedom. The top edge is left free in the vertical direction to avoid unwanted membrane forces developing. The effect of these boundary conditions is further studied in section 9.3.

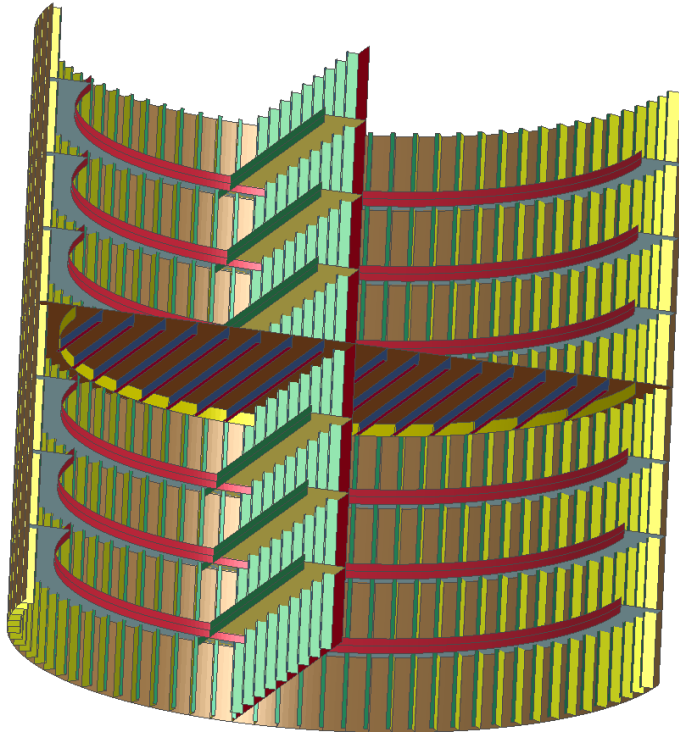


Figure 37: Column model

### 9.1.1 Finite element mesh

Most parts have been meshed using the mesher *IsoMesh* in Patran, with a global edge length of  $l_e = 100$  mm and quadratic element shape. This mesh generator provided a consistent mesh with undistorted quadrilateral elements throughout the entire geometry. Figure 38 shows a representative section of the meshed structure. For the deck part it proved necessary to use the *Paver* meshing routine which uses more irregular quadrilateral elements with some occasional triangular elements with some occasional triangular elements. To ensure proper alignment of the nodes, all plate fields were cut at all intersections with other parts. This allowed the mesh generator to automatically recognise mesh seeds on the edges, and mesh accordingly.

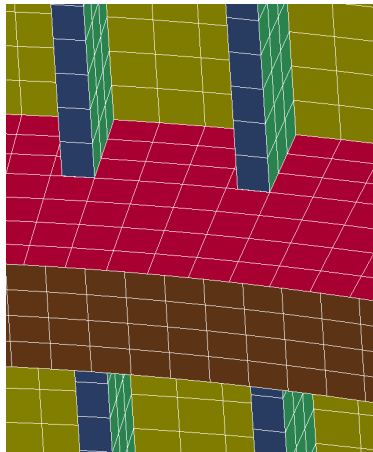


Figure 38: Typical mesh with global edge length equal 100 mm

The element used is the Belytschko-Lin-Tsay shell element. The element is very computationally efficient, and therefore the default shell element in LS-DYNA (Hallquist, 2006). The element is based on a combination of co-rotated and velocity-strain formulations. The co-rotated formulation reduces the complexity of the geometrical nonlinearities by fixing a local coordinate system to the element and decomposing the global deformation into a rigid body motion, and a local deformation (Cook et al., 2002). The deformations in the local coordinates is thus small, and the stresses can be expressed using the Cauchy formulation.

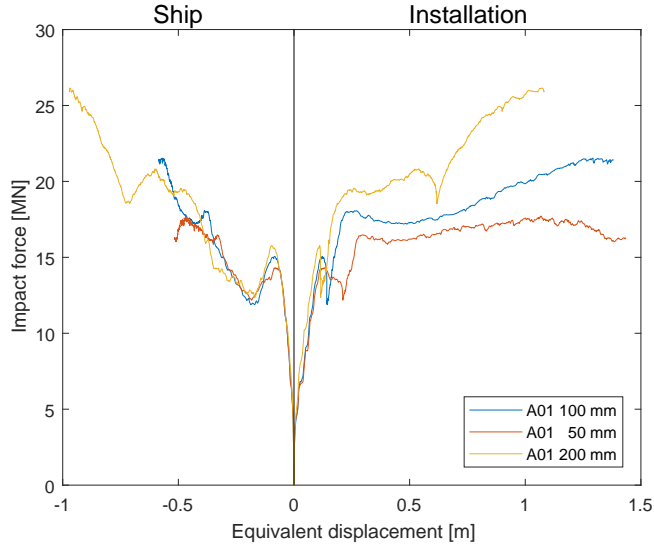


Figure 39: Effect of mesh size

The sensitivity with respect to the mesh size have been studied by performing three analyses of design A01 with global mesh size lengths ranging from 200 mm to 50 mm. The resulting force deformation curves are presented in figure 39. The mesh of the stern corner was left unaltered. The mesh with size 200 gave only one element across the vertical stiffener web, largely limiting the stiffeners ability to fail due to local effects and thus raising the capacity of the structure. Halving the mesh size to 100 mm gave three elements across the vertical stiffener web, resulting in a more physical deformation pattern. However, when another halving of the mesh was performed the analysis gave an even lower capacity for the structure. It is seen that the mesh size of 100 mm will over estimate the strength of the structure to some degree.

The run time of the analysis was found to scale with a factor of  $l_e^{-2}$  quickly resulting in impractical CPU time usage. In this work a mesh size of 100 mm was adopted to accommodate the need for a large number of analyses. In this an inherent error was introduced, but it is assumed that the general behaviour of the system will be captured.

## 9.2 Stern model

The stern model used for the impact analyses is prepared by Force Technology and published with DNV GL recommended practise C208, *Determination of structural capacity by non-linear finite element analysis method* (DNVGL-RP-C208, 2016). The typical element size is in the range of 45-55 mm (DNV GL, 2015).

By using this openly available standardized model, the results obtained can be compared to other analysis with the same stern. It also ensures that the results are easily reproducible. As this thesis focuses on the design of the column, there have been no further assessment of the stern model. The main dimensions of the stern model are presented in figure 40.

The stern model has been analysed in an impact with a rigid column to establish a baseline for the impact forces to be expected. The result of this analysis is presented in figure 41. An interesting point to note is the plateau in the force displacement curve at about 12 MN. This force level is significant for the energy distribution between the ship and the installation, and is further discussed in section 10.1. The maximal force of the ship stern is also important when strength design is desired.

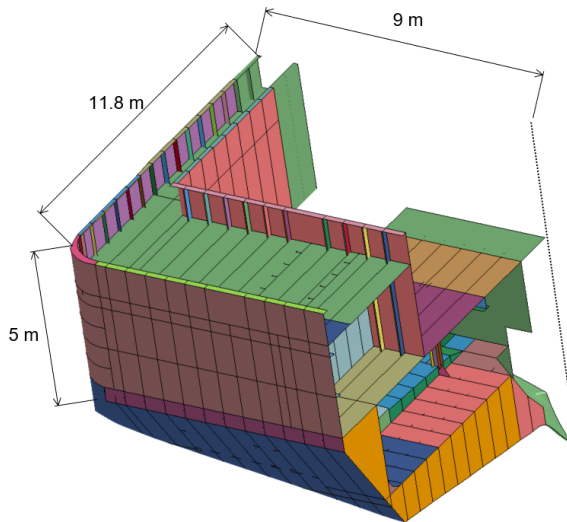


Figure 40: Stern model with main dimensions



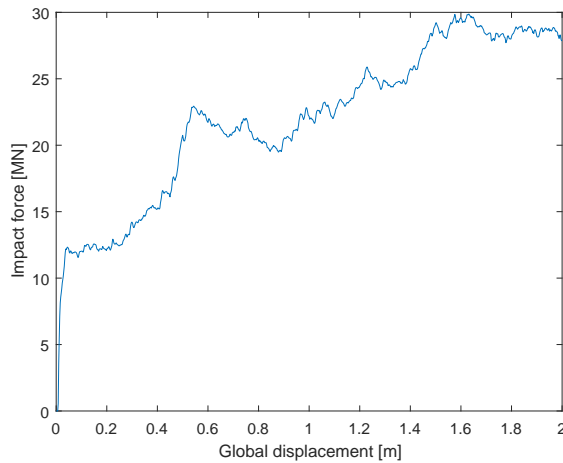


Figure 41: Stern corner vs. 10 m rigid column

It is also noted that this curve is significantly higher than the newly proposed design curve given in figure 5. The curve found herein is however congruent with the one published alongside the stern model, suggesting that the design curve is erroneous.

### 9.3 Effect of boundary conditions

One of the more challenging parts of creating a good finite element models is the choice of boundary conditions. To minimize the need for computational resources it is important that the part of the structure that is modelled is as small as possible. This gives the boundary conditions the task of representing the rest of the structure that is not included, as well as possible reaction forces to other systems.

For the size of the modelled part there were two main concerns that needed to be addressed, the height of the part, and which angle of the column that needed to be modelled.

The angle was set to 180 degrees, leaving the column cross section as a semicircle. This simplification involves fixing the translation degree of freedom of all nodes in the exposed center plane in x and y direction. In figure 42a a full 360 degree analysis is compared with the half model used herein. The force level in the two models are virtually identical, apart from a notable drop at large deformations.

This drop corresponds to point A (as marked in figure 14) reaching the same x coordinate as point B, giving an effect similar to the snap trough behaviour discussed in section 5.1.2. The x and y displacement of a single node in the would be boundary was tracked trough the full column analysis, the results of which is plotted in figure 42b. This shows that the restriction of this degree of freedom will result in some overestimation of the global strength of the structure. However when considering how small this effect proved to be, compared with the relative large gain in efficiency, the half model was adopted for all other analysis. A good side effect of this choice is that the ring stiffeners could be approximated as semicircular fixed arches as discussed in section 7.

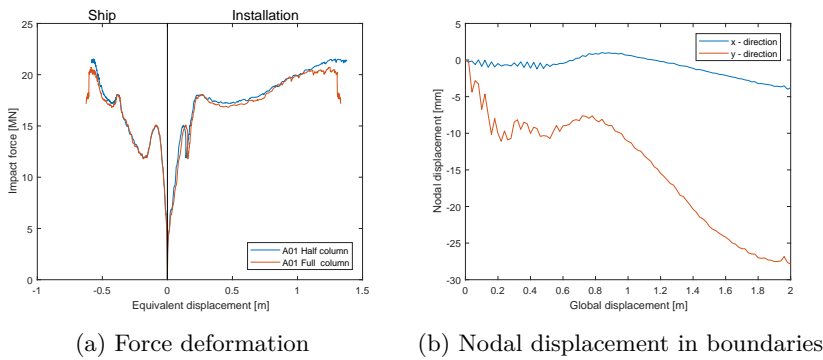


Figure 42: Effect of half model

The other choice is the height of the column that is to be modelled, and consequently how to constrain the top and bottom boundaries. The three tested models were a high model with a total height of 18 m and the top free in z-direction, a low model (H=12m) with the top free in z-direction and the same low model but with the top clamped in the top. Force deformation curves are presented in figure 43 for all three models.

For the high model there was no significant displacement of the top nodes, thus the boundary is deemed far enough away to not influence the results. However the additional elements needed for this larger model added to the computational cost, and gave a want for a more efficient model. The two low models preform equally good for small displacements, but after the collapse of the ring stiffeners unwanted membrane forces quickly develop in the clamped model giving a to large resistance. The capacity is eventually limited by fracture of the vertical stiffeners and shell plate.

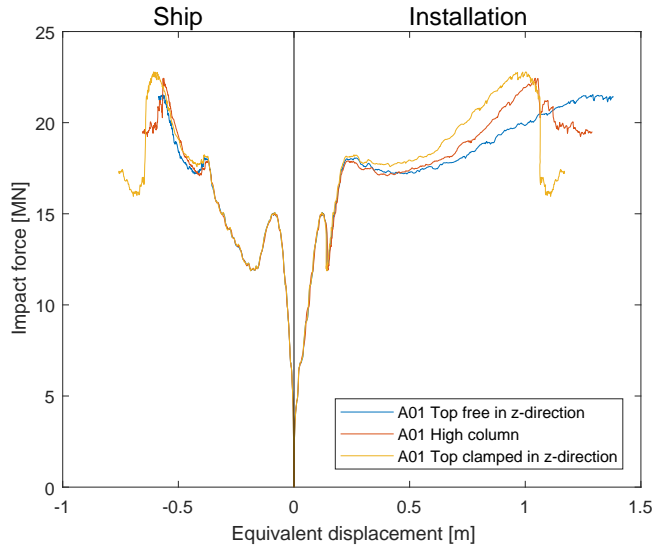


Figure 43: Effect the modelled height

The model where the top nodes are left free in the z-direction perform good up to a equivalent displacement of about 0.5 m, after which the lack of vertical constraints underestimates the membrane forces present. This underestimation of the capacity is however small as well as conservative. At the point where the models have dissipated the required 22 MJ the difference in the equivalent displacement is in the order of 1% for the low model. The low model with a the top nodes free in vertical direction is therefore adopted for most of the analyses, knowing that the force level in the extreme displacements will be underestimated. In some analyses where the behaviour at these displacements were especially sought after the high model was used.

In figure 44 the displacement shape for the different models are shown. Note how the free top plane for the model in 44b distorts.

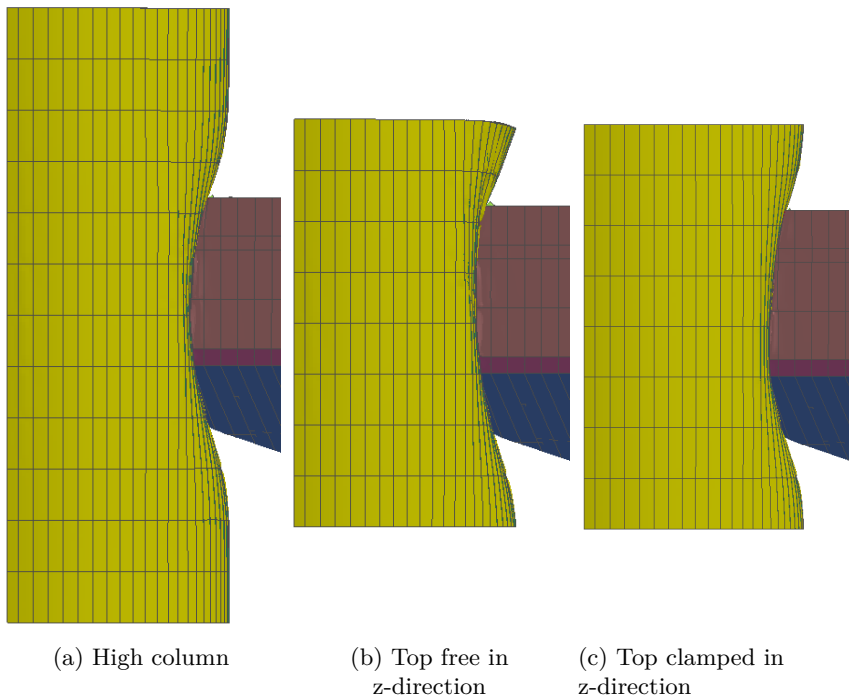


Figure 44: Displacement shape at the end of the analysis

## 9.4 Effect of fracture

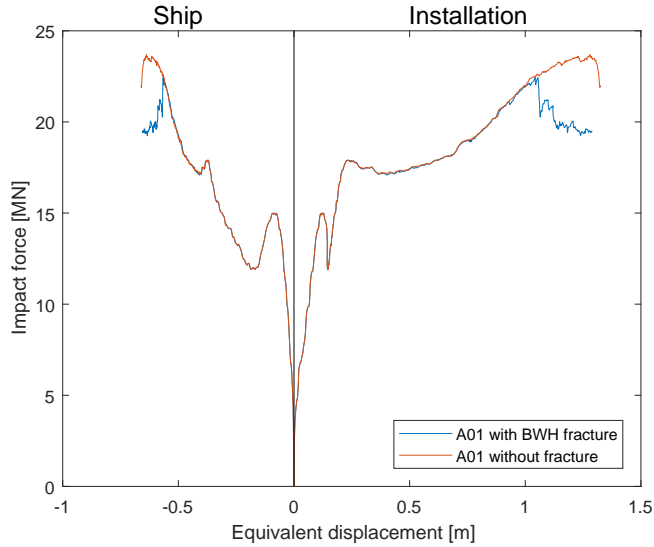


Figure 45: Effect of fracture

The effect of including the fracture model was investigated by analysing design A01 with  $H = 18$  m both with and without fracture, the force deformation curve is presented in figure 45. The fracture becomes significant for extreme deformations, and may only be relevant for analysis where the column is expected to undergo large deformations. However, as the fracture criteria did not impose any significant change in the computational time it was left active in all analyses. The added height in this analysis proved necessary for the membrane forces to develop as discussed in section 9.3, Without this the effect of fracture becomes insignificant.

## 9.5 Analysis control

The software used to perform the analyses, LS-DYNA, is controlled via a series of control cards. Each card controlling some essential part of the analysis. The most important parameters will be discussed in the following section. For a full overview of the parameters used in the analyses, see appendix B.

### 9.5.1 Contact definitions

The method used to account for contact between bodies is based on the penalty method presented in section 5.1.1.

The contact definitions is controlled by the cards `*CONTACT_AUTOMATIC_SURFACE_TO_SURFACE` and `*CONTACT_AUTOMATIC_SINGLE_SURFACE` for the contact between bodies, and the internal contact respectively. The contact types are symmetric with respect to slave and master, which means that the subroutine that checks for penetration of nodes are called twice, one for each of the contacting faces (LS-DYNA Support, a). The choice of master and slave surfaces is thereby irrelevant to the solution. The methods are also non-oriented meaning that they can detect penetrations from both sides, a crucial property in collision analyses where the deformations are expected to be large.

### 9.5.2 Timestep and mass scaling

The timestep and the mass scaling parameters are given in the card `*CONTROL_TIMESTEP`.

In the analysis software LS-DYNA the assignment of timestep size is automated. The algorithm uses the method discussed in section 5.2.2 for each element. The default safety factor 0.9 is used, giving the following expression for the next global timestep

$$\Delta t^{n+1} = 0.9 \cdot \min\{\Delta t_1, \Delta t_2, \dots, \Delta t_N\} \quad (122)$$

where  $N$  is the number of elements (LS-DYNA, 2003).

The individual elements timestep is as shown dependent on a characteristic length and mass. As the analysis progresses the lengths may change. Some elements may become very small and thereby require the time step to be reduced significantly to ensure stability. To counter this phenomena one can use a technique known as mass scaling. In mass scaling a non physical mass is added to the structure to increase the critical time step (LS-DYNA Support, b). This process will naturally

affect the results of the analysis, but sometimes this effect is negligible and the addition of extra mass is justifiable.

Invoking selective mass scaling on the smallest elements in the analysis may significantly reduce the time consumption of the analysis. However, Storheim (2016) warns that the use of this technique in ship-ship collisions may affect the energy balance. One should therefore verify that it does not influence the results before utilizing the method.

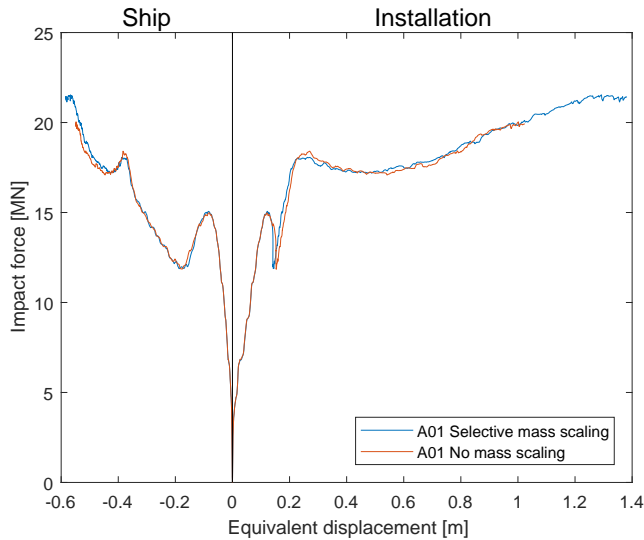


Figure 46: The effect of mass scaling

In figure 46 an analysis with mass scaling is compared with one without. The non mass scaled analyses timed out before it could complete, however the two force deformation curves seems to align well.

In the analysis with mass scaling the non physical mass was added to ensure that the minimum time step did not become lower than  $3.0 \cdot 10^{-6}$ . The mass added to the system was logged through the analysis and proved to be in the order of 10 kg, of which all was added to elements in the ship model. This mass is deemed negligible in relation to the energy levels in the problem. The technique about halved the required CPU time and gave no noticeable ill effects. Mass scaling was adopted for the remaining analysis.

### 9.5.3 Impact speed

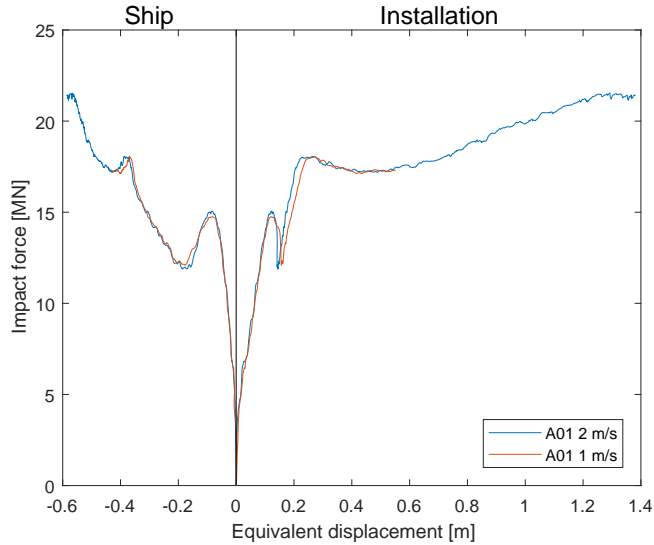


Figure 47: Effect of impact velocity

The impact speed is controlled by two different control cards, `*BOUNDARY_PRESCRIBED_MOTION` and `*INITIAL_VELOCITY_NODE`, which control the prescribed constant velocity and the initial velocity respectively. The prescribed motion was given to the boundary of the striking vessel, while the whole vessel was assigned an initial velocity. Initial velocity was given to avoid an acceleration phase in the start of the analyses, which can give undue stresses on the vessel.

A key assumption in this work is that external and internal mechanics can be decoupled. From this it follows that the force deformation curve should be unaffected by the impact velocity. In figure 47 two analyses with different impact velocities are compared. The analysis with velocity 1 m/s was terminated after one second to save on CPU and memory resources. The results seem to coincide quite well. The only difference between the two impacts is the change in kinetic energy of the impacting bodies. This change was examined throughout the analysis and deemed negligible in contrast to the strain energy developing in the structure.



## 9.6 Effect of both structures being deformable

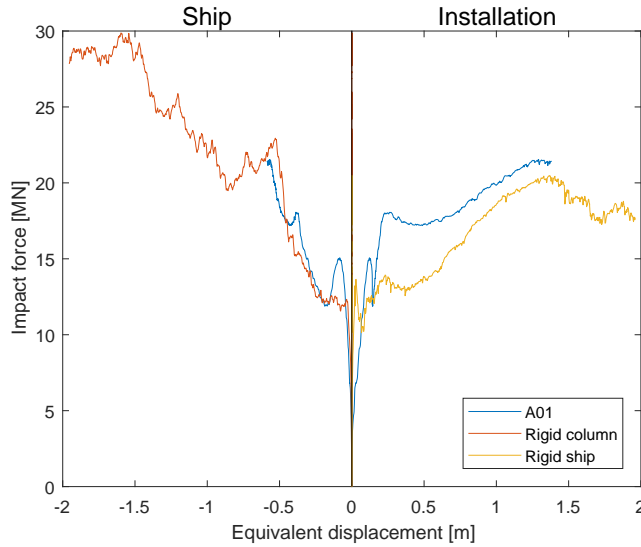


Figure 48: Comparison between coupled and uncoupled analysis

In traditional analyses the force deformation curves are often obtained independently for the two colliding bodies, keeping the other rigid (DNVGL-RP-C204, 2016). This approach can give erroneous results, especially in shared energy design where both bodies are expected to undergo significant deformations. This is illustrated in figure 48 where three analyses are presented, one where the column is kept rigid, one where the stern corner is rigid and one where both bodies are allowed to deform. Both the rigid analyses underestimates the force levels to some extent. Most notably is the underestimation of the force level in the column when the stern corner is kept rigid, due to the fact that the corner does not flatten and thus presents a much smaller impact area. The development of the contact area is discussed in section 10.2.

## 10 Analysis of stern corner impact

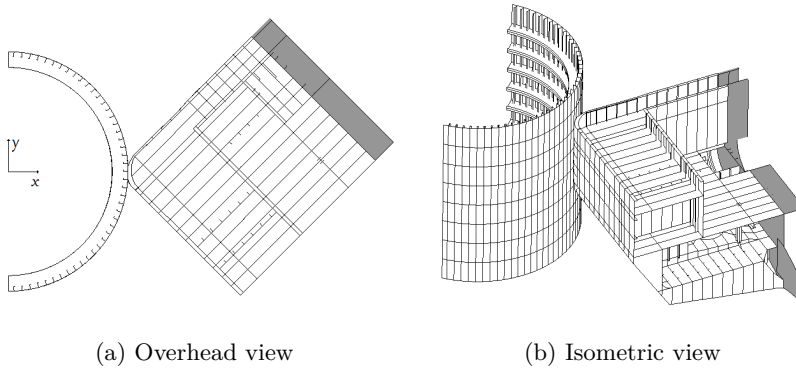


Figure 49: Overview of impact scenario

In the following section some of the results from the analyses will be presented and discussed. The full description of the designs used in each analysis can be found in appendix A. Force deformation curves for all the different designs is included in appendix F.

The part of the striking ship highlighted in figure 49 are defined as a rigid body and only permitted to move in the global x direction. The rigid part is given a prescribed constant velocity of 2 m/s for the entire simulation. The analysis is terminated after 1 second, giving an total deformation of 2 m. This have proved sufficient to cover the required energy dissipation for all but the weakest columns.

The initial position of the stern corner is such that there is only a few millimetres of clearance between the two bodies, sufficient to prevent initial penetration, but not so large as to introduce unnecessary time delay before the first contact.

### 10.1 Phases of the stern corner impact

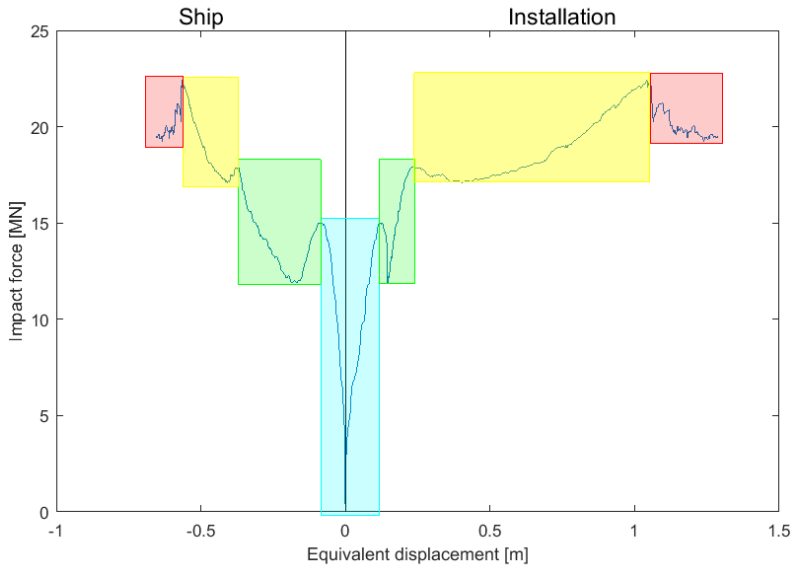


Figure 50: Phases of a typical force displacement curve from a stern corner impact

A typical force deformation curve for the stern corner versus column collision can be divided into four phases. First both the ship and the installation undergoes minor deformations as the impact force increases rapidly. At an impact force of about 15 MN the stern corner collapses and the force level drops while the ship sustains a large deformation. This force level corresponds to the plateau in the force deformation curve for the ship, as seen in figure 41. As the ship strengthens the force level rises again and reaches a local maximum, this top is taken as the collapse load for the installation.

Now the installation obtains a large deformations as the ring stiffeners are no longer able to carry the load. After some displacement the stresses redistributes and membrane effects in the shell and vertical stiffening becomes important, these stresses give another rise in the total resistance until the last phase is reached where the shell and vertical stiffening fractures due to excessive strain. The yellow and red phase will hereafter be referred to as the post failure region.

A picture from each of the phases is presented in figure 51, note the fracture of the vertical stiffeners in the last picture.

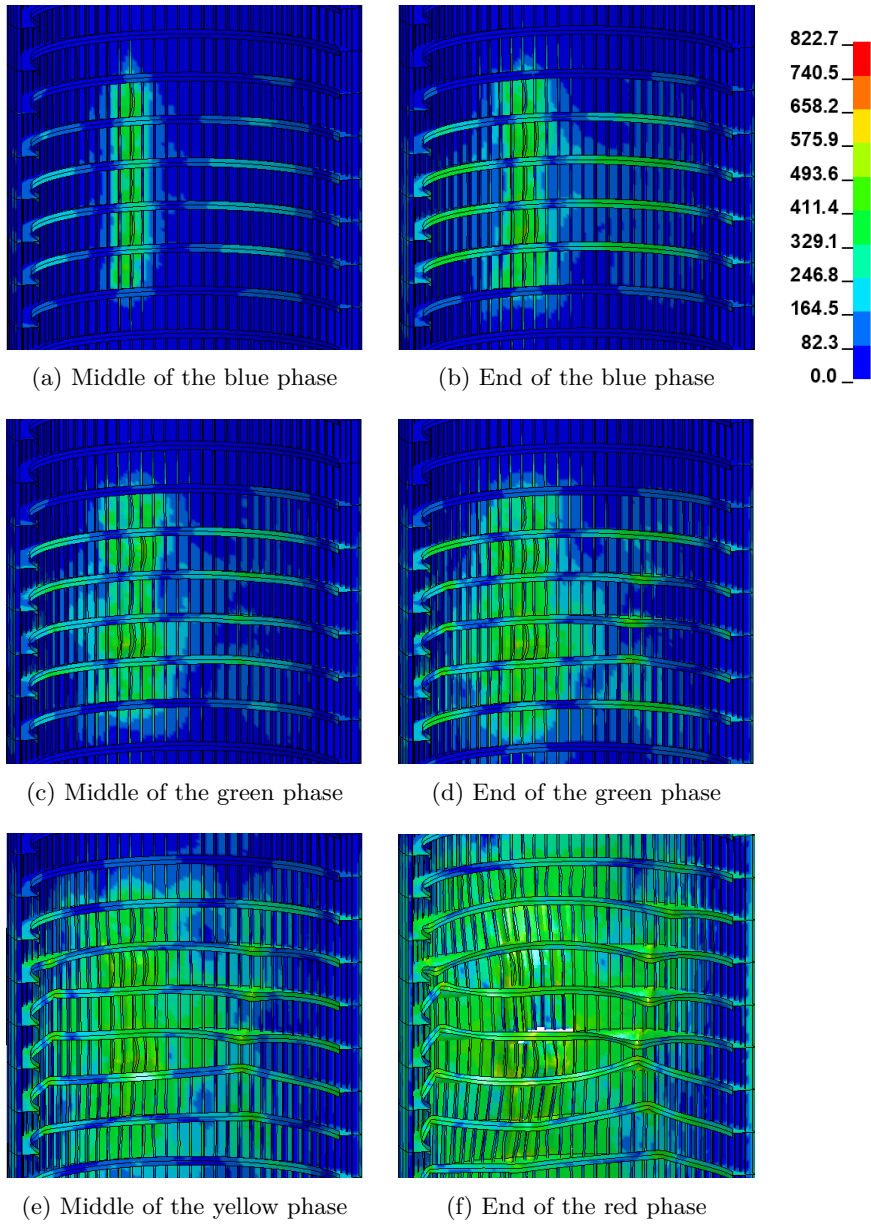


Figure 51: Collapse of A01. Von Mises stress in MPa.

## 10.2 Impact area and pressure

Figure 53 shows how the impact pressure develops as the analysis progresses. The pressure starts as expected in a vertical band where the stern impacts, with high points corresponding to the stiffeners in the stern. Further the stern corner deflects in such a way that the pressure forms two distinct vertical bands moving to either side and unloading the middle section. It is worth noting that this unloading leads to pressures that greatly exceeds the value one would get if one assumes the impact load as uniformly distributed over the impact area. For comparison, the pressure would be about 1.3 MPa for the collapse load 18 MN if it was to be taken as a uniformly distributed pressure, that is a factor of 10 lower than the pressures present.

Two horizontal bands can also be observed in the pressure, especially at large deformations. These bands corresponds to the two decks in the stern model. In this case the strong point in the ship caused by the decks happen to strike the column between the ring stiffeners, this means that the vertical stiffeners must have the capacity to carry the load to the nearest ring stiffener to avoid a collapse.

The impact force is plotted against the analysed time in figure 52 as a reference, and the points where the pressures in figure 53 are recorded are marked.

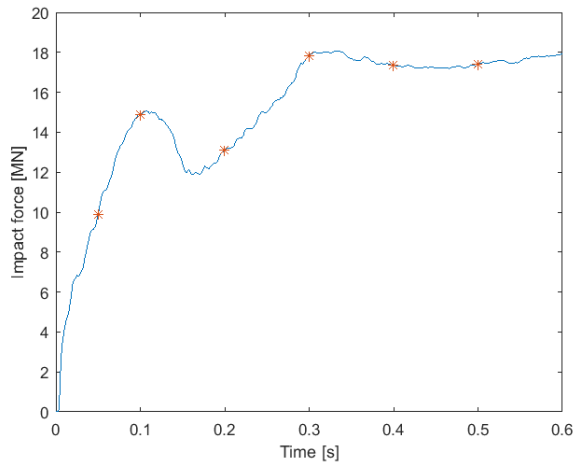


Figure 52: Impact force versus time

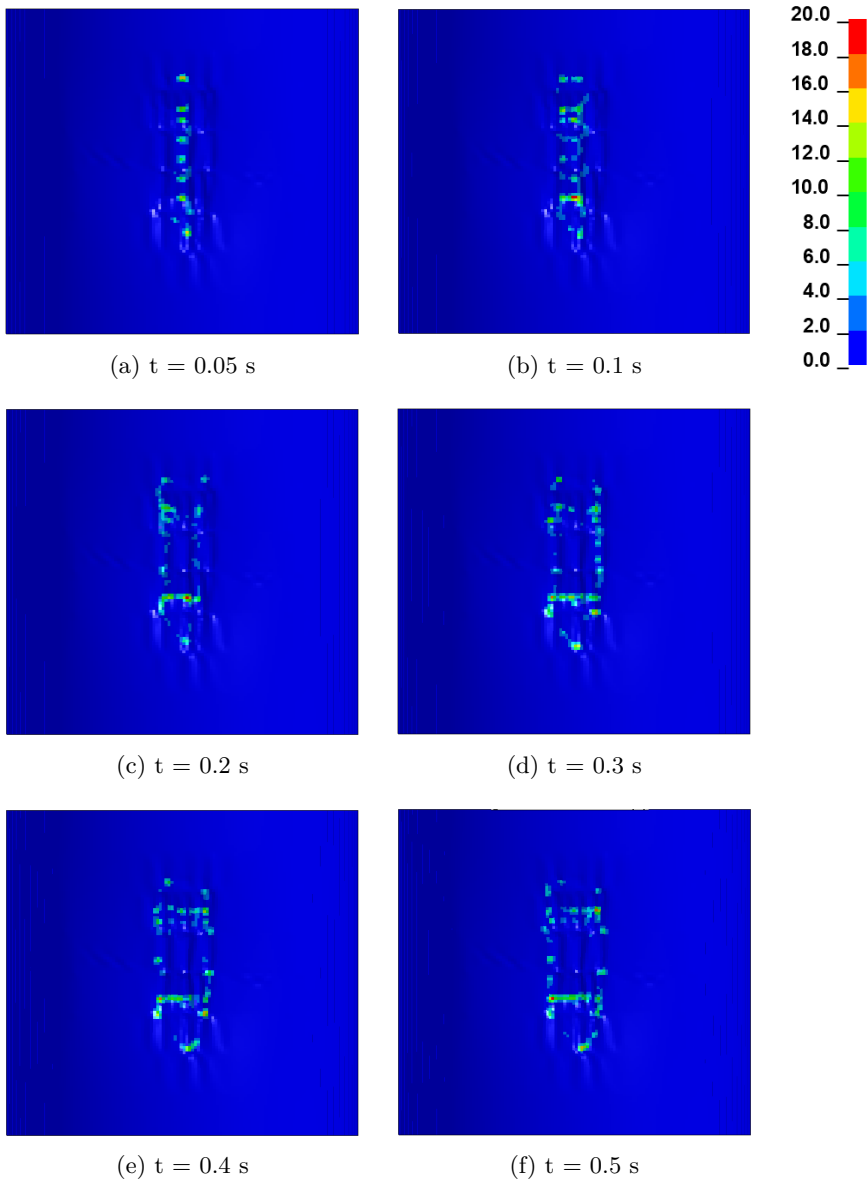


Figure 53: Interface pressure on column A01. Values in MPa.

### 10.3 Relative strength

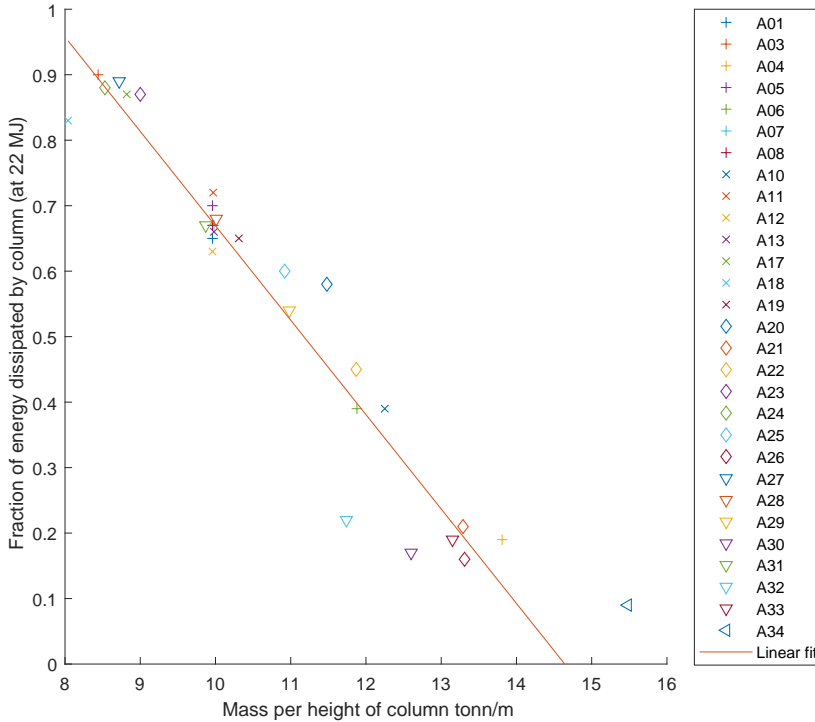


Figure 54: Mass as a measure for strength

In the design codes regarding ship collision the term relative strength is often used to describe the distribution of energy dissipation between the impacting bodies (see figure 3). This is however not so easily determined without performing an analysis of the collision scenario. It would be beneficial to use a more intrinsic property of the analysed structures to determine the distribution of energy. For the simple case of the curved stiffened shell there seems to be a correlation between the mass and the ability to dissipate the energy. This relation is shown in figure 54, where the fraction of the ALS requirement dissipated by the structure is plotted against the mass.

The use of mass as a measure for relative strength is however only suitable when comparing structures with similar load bearing geometry. For example when a deck or bulkhead is added to the cylinder the capacity increases significantly without increasing the mass with the same factor.

As the mass is an important parameter for design of offshore structures, this graph may be used to compare different designs on their load bearing abilities. Structures below the linear fit performs better than expected for that total weight. By correlating these designs to their individual dimensions it is observed that these generally have strong ring stiffeners spaced close together.

Some analyses are excluded from figure 54 due to the capacity being so low that the required 22 MJ was not dissipated during the 1 s analysis. Analysis A34 is worth noting as this design falls in the strength design range. In this analysis the ring stiffeners does not collapse and the stern corner takes all the deformations. The column still dissipates some energy due to deformations of vertical stiffeners and local plate fields.

A parallel to Minorsky's method of correlating strain energy with deformed volume can be seen, but as the energy levels are too low no direct link can be established.



### 10.3.1 Internal distribution of energy dissipation

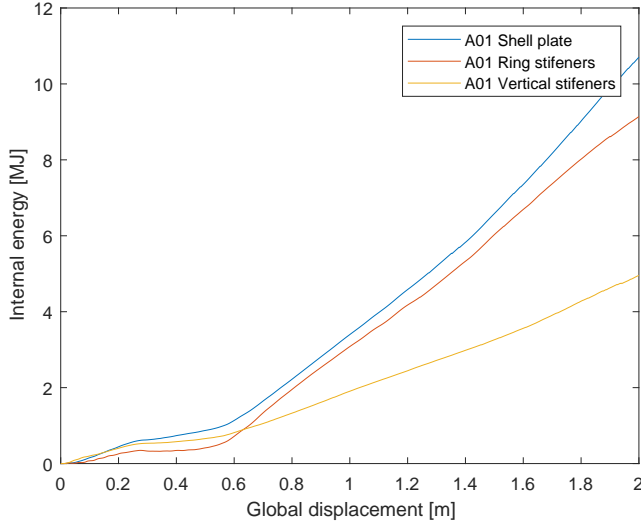


Figure 55: Distribution of energy for design A01

The dissipation of energy in the column is logged for all the parts of the column separately. This allows for the study of the distribution of said energy between the components. In figure 55 the energy dissipated by the different parts of the structure is plotted against the time. The values for the ring and vertical stiffeners are without the associated plate flange, as the shell plate is plotted as a separate part.

It is observed that most of the energy is dissipated by the vertical stiffeners the first 0.3 seconds of the impact. After this time the the ring stiffeners fail and the plastic work required to deform these dominates the energy dissipation for the rest of the process. The shell plating is the part that dissipates the most energy. The plate deforms in three different ways, as a plate between the stiffeners, as the plate flange of the vertical stiffener and as the plate flange of the ring stiffener.

For large displacements the energy dissipated by each part was found to be proportional to the mass of the part.

## 10.4 Effect of ring stiffeners

In the designs considered in this work the ring stiffeners are the main load carrying components in the radial direction. To avoid large deformations of the column it is therefore important that the ring stiffeners are designed with sufficient strength to withstand the impact. The effect of cross section types, cross section slenderness and ring stiffener spacing is investigated in the following. It is seen that after the loss of the ring stiffeners the resistance decreases and large deformations occur. The collapse of the ring stiffeners are proposed as a limit for the structure to be classified as a strength design.

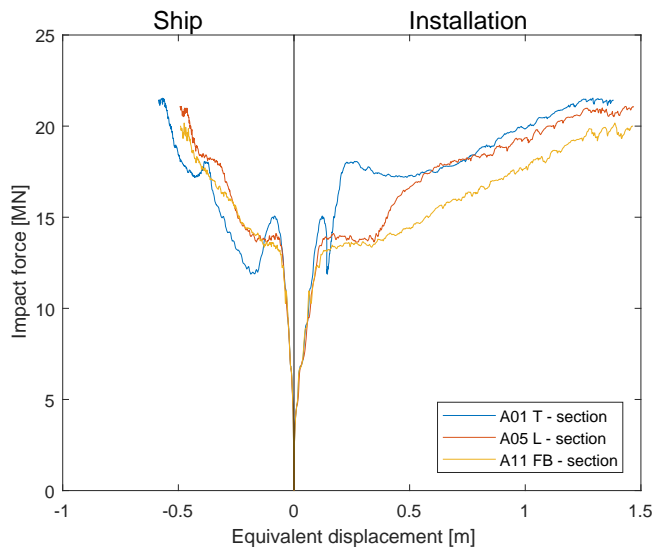


Figure 56: Ring stiffener sections

The effect of the ring stiffener cross section type was investigated by analysing designs A05 and A11 where the stiffener type is changed to a L-type and a flat bar (FB) respectively. The cross sectional areas and the plastic moduli are kept constant. The results of the analyses is presented in figure 56. The main takeaway from this figure is that the collapse of the ring stiffeners happen at a significantly lower impact force for the L and FB stiffeners. This can be explained by the fact that the lack of lateral support for the FB stiffeners and the unsymmetrical nature of the L stiffeners advances the onset of local failure of the ring stiffeners.

Some displacement after the first collapse the L-type stiffeners regain some strength

and the forces eventually reach the same level as in the case with the T-type stiffeners.

At large deformations the stiffness of the system is virtually unaffected by the choice of stiffener section as other load carrying members come into effect.

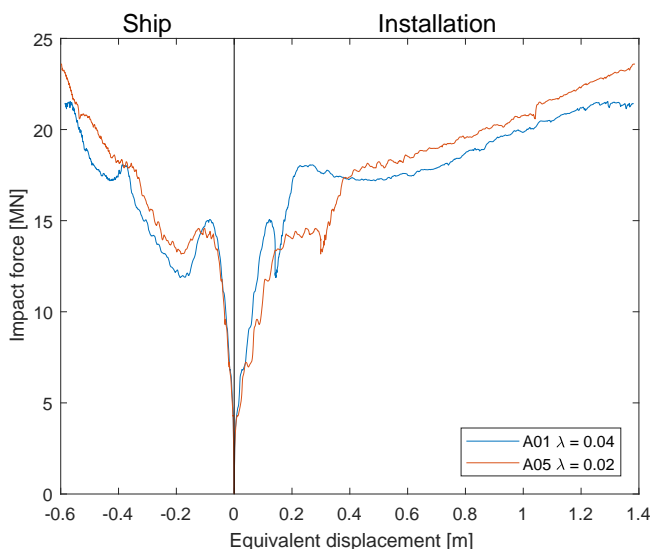


Figure 57: Ring stiffeners with different slenderness

The analysis of the single ring stiffeners in section 7 showed that the slenderness of the cross sections are important for the moment capacity of the structure. In figure 57 the response of two cross sections with different slenderness ratio  $\lambda$  is compared. The cross sections have the same area, and thereby the same weight. The plastic cross sectional modulus  $W_P$  is different for the two designs giving two different responses. The main difference is the force level at which the ring stiffeners collapse. This change appears quite big in the force displacement curves due to design A07 failing just before the stern corner at about 15 MN. This leads to a much larger displacement in this design compared to design A01. At large displacements both cross sections exhibits more or less the same behaviour due to other load carrying components coming into effect.

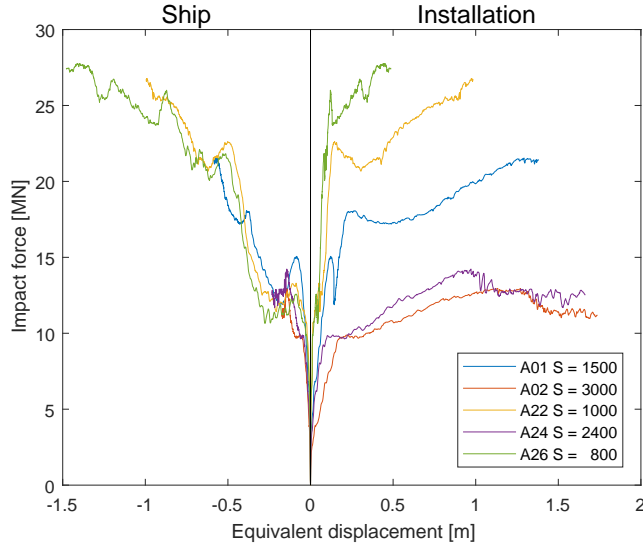


Figure 58: Effect of varying ring stiffener spacing

Changing the spacing between the ring stiffeners will obviously affect the weight of the structure significantly, and one expects the strength to rise proportionally. In figure 58 several analyses with varying ring stiffener spacing are compared. For the three analyses with the smallest spacing the collapse load for the column increases about linearly with the factor  $S_{RS}^{-1}$  as shown in section 8. For the two lowest analyses very little extra capacity where gained by reducing the spacing. This is because no additional ring stiffeners came in contact with the stern, and thus no extra capacity where gained.

### 10.5 Effect of vertical stiffeners

The vertical stiffeners serves two main purposes. Firstly as a load bearing structure in the vertical direction, and secondly as a mean to carry a radial load to the ring stiffeners. In this work only the latter is studied. As a secondary effect the vertical stiffeners also serve as tripping brackets for the ring stiffener web, preventing local buckling.

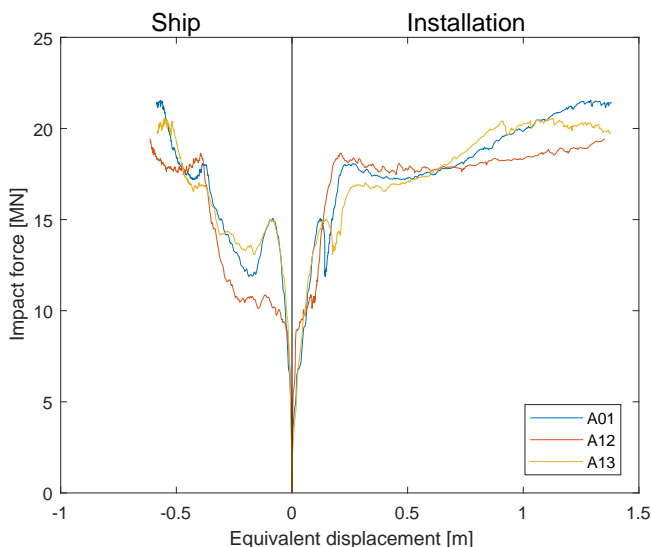


Figure 59: Equal total vertical stiffener area

Two different designs with altered vertical stiffening are modelled and analysed, these designs are named A12 and A13. In figure 59 they are presented together with design A01 with unaltered vertical stiffening. In design A12 the total number of stiffeners are halved, while the cross-sectional area of each stiffener is doubled resulting in the same total area. In design A13 the opposite was done, giving twice the number of stiffeners but still with the same total area.

As observed in the force deformation curve, this does not change the behaviour of the collapse to a large degree. One aspect to note is that the stern corner fails at a slightly lower total force for the case with the strongest vertical stiffeners. Some of this effect may be due to the vertical stiffeners being higher and thus preventing the vertical displacement of the stiffener web to a larger extent, and postponing the local failure of the ring stiffeners.

In the post failure range the stiffness of design A12 is the lowest while design A13 with the most numerous stiffeners are the highest. In this phase the load is predominantly carried as membrane forces in the vertical elements. Even though the total cross sectional area of stiffeners is the same for these three analyses the number of stiffeners that are mobilised is different, and thus the area that carry the load.

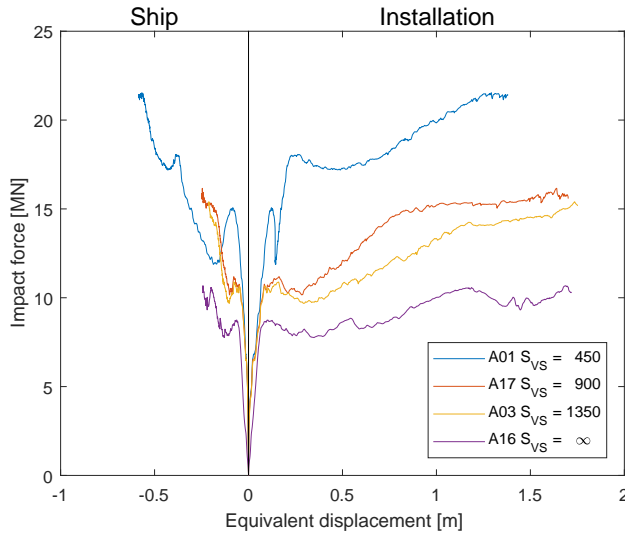


Figure 60: Equal vertical stiffener sections

A series of analyses with the same vertical stiffener section but with varying spacing was then performed. The force deformation curves is given in figure 60. The reduction in vertical stiffening does, as expected, influence the impact force significantly.

It is worth noting that the first collapse load for the two middle analyses (A17 and A03) is similar even though the vertical stiffening is different. In both these scenarios the stern impacts a single vertical stiffener which takes the initial load. The distance between the vertical stiffeners are also wide enough such that the folding mechanism discussed in section 7.4.2 can form unhindered.

The capacity of one ring stiffener with design C01 and no vertical stiffeners have been shown to be equal to 3.28 MN (see fig 34a). The stern contacts four ring stiffeners giving the expected capacity

$$P_{collapse} = 4 \cdot 3.28 = 13.12 \quad [\text{MN}] \quad (123)$$

for the case without ring stiffeners. This is higher than what is observed with none ring stiffeners, however quite close to what is found in the case for few stiffeners.

With vertical stiffeners the capacity of the ring stiffener raised to 5.12 MN due to the folding being constrained. In this case the capacity is expected to be

$$P_{collapse} = 4 \cdot 5.12 = 20.48 \quad [\text{MN}] \quad (124)$$

which is slightly higher than what is found.

In analysis A16 there are no vertical stiffeners, and the entire load must be carried by the ring stiffeners and the shell plate. These analysis clearly show how the presence of vertical stiffeners is important for the global strength.

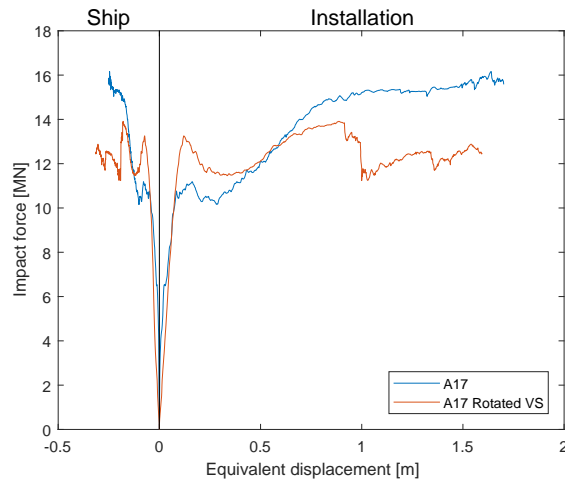
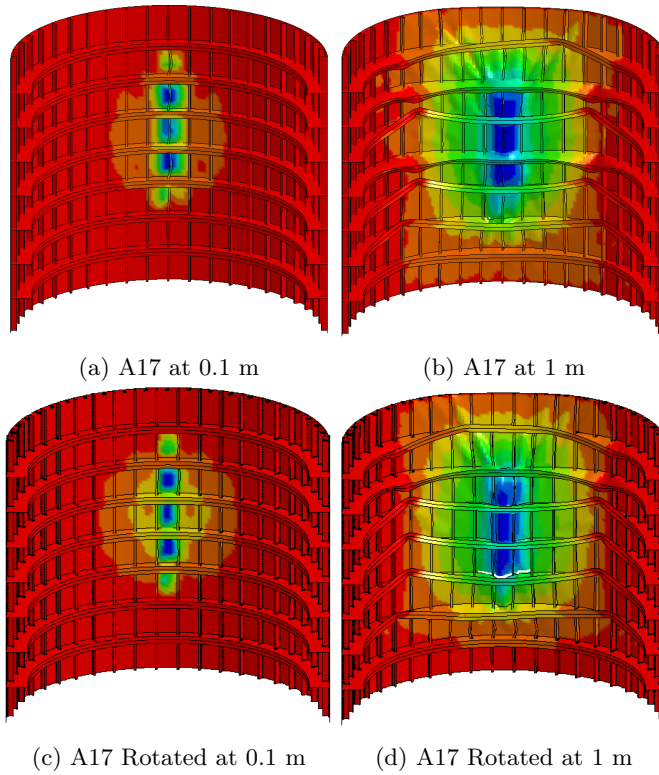
The orientation of the vertical stiffeners in relation to the impact direction also proved important for the collapse load. The two analyses depicted in figure 61 have the exact same scantlings, however they give quite different force deformation curves. In the original analysis (A17) the stern corner impacts exactly on a vertical stiffener, while in the second (A17 Rotated VS) the vertical stiffeners are rotated such that the impact happens between two stiffeners.

A plausible explanation for the discrepancies is that even though the stern corner in the second scenario hits between two stiffeners the impact area is wide enough to include the two neighbouring stiffeners, while for the first scenario only one stiffener is affected. This may explain the difference in the initial peak. Further the area of the column affected by the impact widens and more vertical stiffeners contributes to the load bearing. At this point the ring stiffeners have failed and an important mechanism for supporting the load is the membrane forces in the vertical direction.

From studying the analysis in greater detail it becomes apparent that in the scenario where the column is rotated one fewer vertical stiffener contribute in this load bearing mode and consequently the stiffness is reduced. This becomes even more significant at about 1 m equivalent displacement in the rotated case where the two central vertical stiffeners fractures due to excessive tensile strain.

It is also noted that the local tripping of the ring stiffeners happen in another location when the stiffeners are moved. This changes the geometry of the problem and ultimately the collapse load of the structure. The change is not large (from about 36° to 40° away from the centre) however this shows that the local failure will happen between two vertical stiffeners.

All the other analyses herein is oriented such that the stern corner impacts on a vertical stiffener.



(e) Force deformation curve

Figure 61: Effect of relative position of the vertical stiffeners



## 10.6 Effect of shell thickness

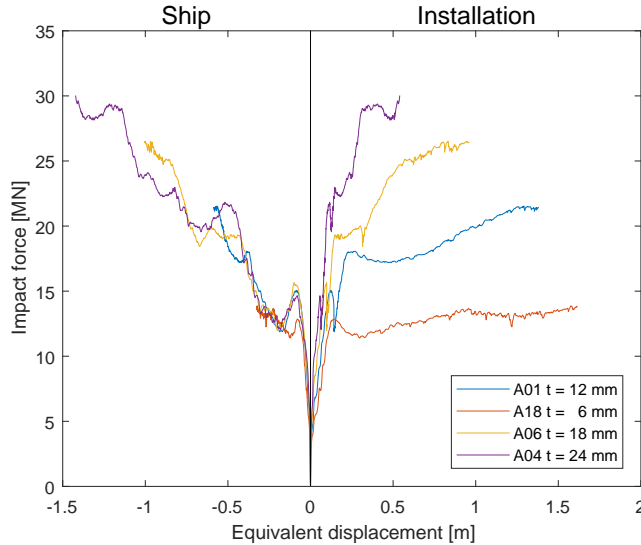


Figure 62: Effect of shell plate thickness

The effect of the outer shell plate thickness was investigated by analysing three similar stern corner impacts with only the shell thickness as the changing parameter. The results are plotted in figure 62 together with the original design A01. The thickness of the shell plating proved to influence the impact load quite much, as it deforms dissipating a large amount of energy. The change in thickness also changed the total weight of the structure significantly as the shell plating usually make up a large portion of the overall weight.

This approach is not an effective way of strengthening the structure. With reference to figure 54 where the amount of impact energy dissipated by the column is plotted against the mass of the structure, it is found that all the analyses fall more or less on the trend line. Other solutions, particularly with many close spaced ring stiffeners, have proved much more efficient in raising the strength of the structure without adding large amounts of weight.

In the post failure phase the stiffness of the structure increases with thicker shell plates. Here the shell plate can be regarded as the plate flange of the vertical stiffeners that is carrying the load as membrane forces.

## 10.7 Effect of bulkhead

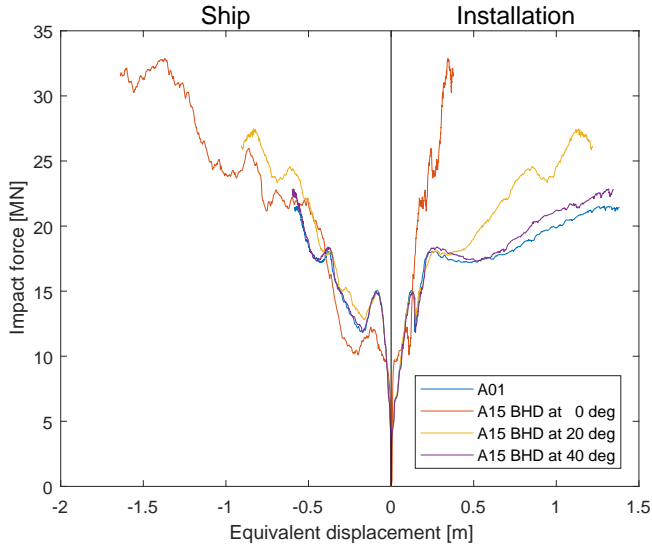


Figure 63: Effect of bulkheads

In offshore applications one often find vertical bulkheads in stiffened columns. The effects of these is therefore interesting to examine. In figure 63 three different impact scenarios where a bulkhead is present are shown, together with the same same column without bulkhead for comparison. The first scenario is an impact directly in way of the bulkhead. In this case the stern deforms significantly and dissipates most of the energy. However when the bulkhead is rotated  $40^\circ$  away from the line of impact the contribution from the bulkhead becomes insignificant and the force level matches that of the column without a bulkhead. For the case where the bulkhead is offset by  $20^\circ$  some mixture of the two behaviours is observed. The first collapse of the ring stiffeners happen at the same force level, but after some displacement the presence of the bulkhead strengthens the structure by preventing the rotation of the second hinge. A horizontal section is included in figure 64 to better illustrate this point.

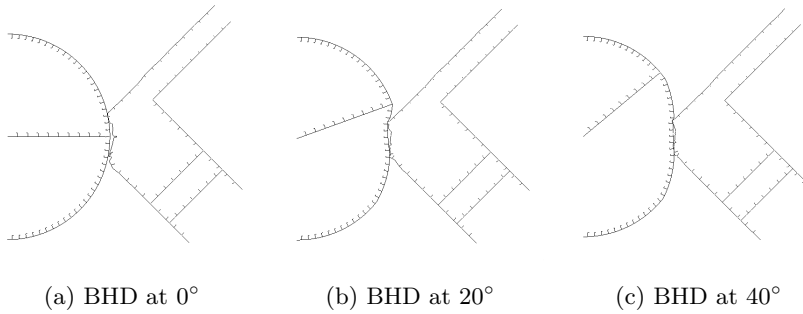


Figure 64: Horizontal section through the column and ship in the way of the middle most ring stiffener at global displacement equal to 1.2 m

### 10.8 Effect of deck

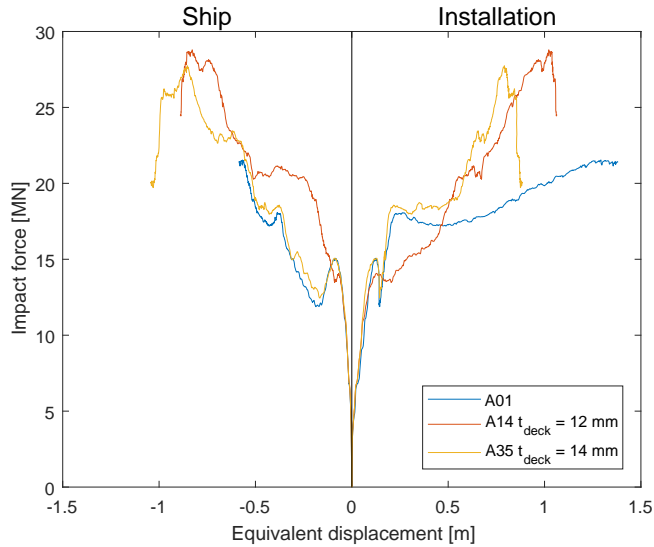


Figure 65: Effect of deck

Decks may also be present in columns and may be influential on the global strength. Two different decks are considered, the effect of which are presented in figure 65. Surprisingly design A14 was shown to perform worse than design A01

even though they have the same scantlings apart from the deck. The reason for this is that a ring stiffener had to be removed in order for the deck to be fitted, and the deck plating is thinner than the web of the ring stiffener giving rise to local crushing. At larger displacements the continued crushing of the deck gives a higher impact load as one would expect. In design A35 the plate thickness of the deck is set to the same thickness as the ring stiffener web. The impact force does in this case follow the same level as for the case without deck until the first collapse and then diverges as the deck starts to deform. To reduce the total weight added by the deck, a solution could be to use the same thickness as for the ring stiffener web for an outer boundary of the deck and reduce the thickness towards the center of the column.

From these analyses it seems like the local crushing of the ring stiffener web is the catalytic factor for the collapse of the ring stiffener. This effect should be studied further.

## 10.9 Side and bow impact

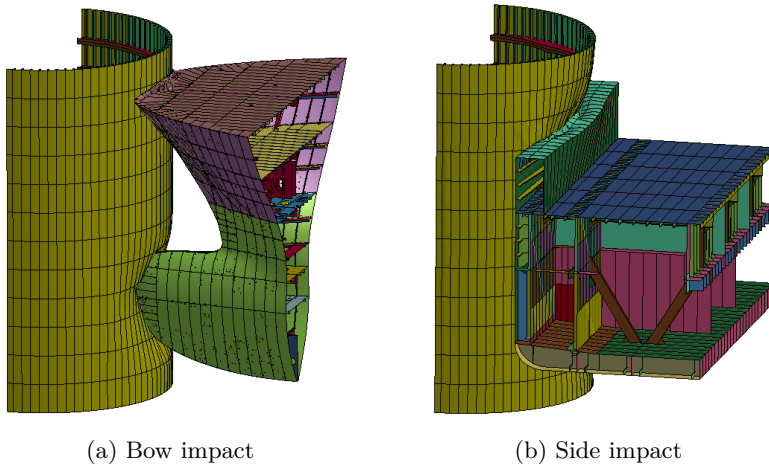


Figure 66: Deformed bow and side after 2 m global displacement

The platform column may also be subjected to side and bow impacts. Two analyses have been prepared to compare these impact scenarios with the stern impact analysed herein. Both models are published as an appendix to the design code DNVGL-RP-C208 (2016) together with the stern corner, and are designed

to be representative for the type of platform supply vessels that operate on the Norwegian shelf. The deformed bodies after the impact is shown in figure 66, the resulting force deformation curves is given in figure 67.

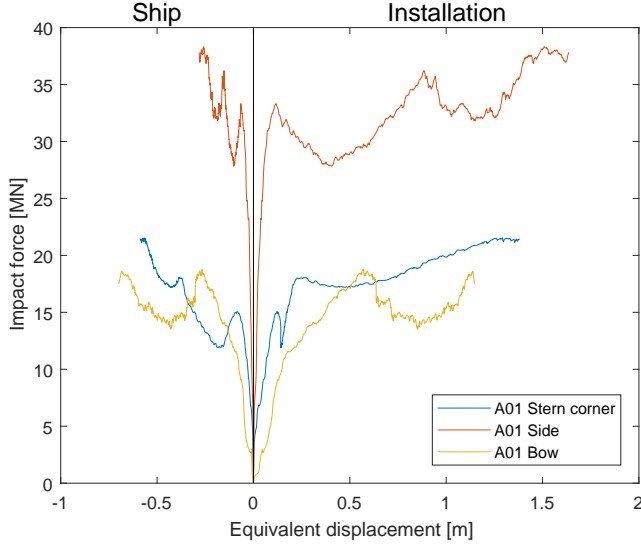


Figure 67: Comparison between stern corner, side and bow impacts

The side impact resembles the set-up used to evaluate collapse load of the individual ring stiffeners in section 7. The side itself is sufficiently strong to not undergo any significant deformations. If one neglects the contribution from the bulwark the total number of ring stiffeners in direct contact with the ship side is 6. An estimate for the structural capacity can then be made as

$$P_{collapse} = 6P_{cr,RS} = 6 \cdot 9.6 \frac{M_P}{R} = 6 \cdot 5.4 = 32.4 \quad [\text{MN}] \quad (125)$$

which is confirmed to be about correct in figure 67. After the collapse the structural capacity is reduced, and is not regained before after a large displacement. The peak around 1 m is due to the flat ship side impacting the hinges that have formed at  $45^\circ$  from the impact direction, previously denoted as point B.

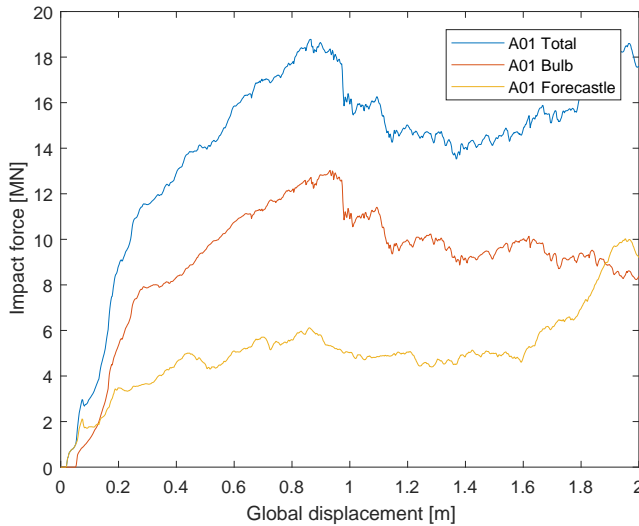


Figure 68: Force distribution between forecastle and bulb in bow impact

The bow impact is somewhat different from the two other scenarios in that the contact surface is split into two distinct areas with very different relative resistance, namely the bulb and the forecastle. In figure 68 the force from each impact is plotted separately. The forecastle deforms without causing significant damage to the structure. The bulb on the other hand has a much higher resistance and penetrates the outer shell. The collapse of the first two ring stiffeners that initially contacted the bulb happens at 0.3 m, with a collapse load at about 8 MN. This is somewhat less than the  $2P_{cr,RS} = 10.8$  MN predicted. This is probably due to the narrow impact area of the bulb, which lead to local crushing of the ring stiffener web.

After the first collapse the total force keeps rising as the vertical membrane forces forming around the bulb increases. After about 1 m global displacement the vertical stiffening fractures along with the shell plate due to excessive straining. This penetration of the outer skin may pose problems for the buoyancy and stability of the structure, considering that the bulb will impact at the waterline.

### 10.10 Strength design

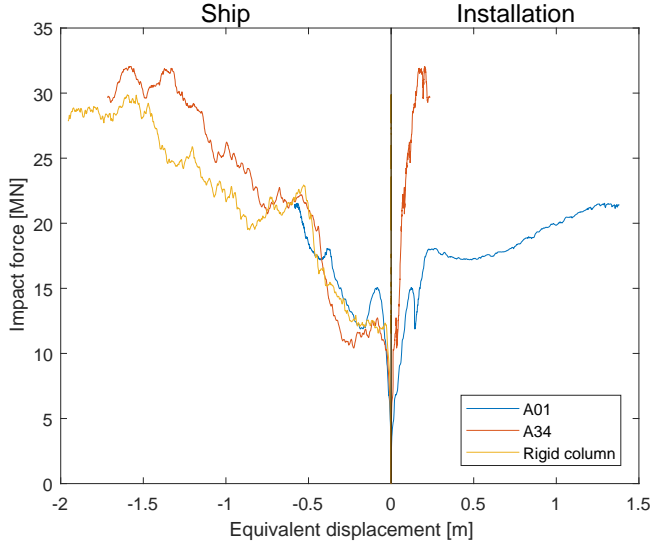


Figure 69: Force displacement in strength design

In a strength design case the impacting ship should undergo most of the deformations. From the analysis of the stern corner versus the rigid column it was found that the peak load is about 30 MN. Due to deformations of the column, a slightly higher load should be expected.

For design A34 the ring stiffeners are spaced with a distance  $S_{RS} = 600$  mm giving 11 ring stiffeners in contact with the impacting ship. The maximal resistance can be estimated as

$$P_{collapse} = 11P_{cr,RS} = 11 \cdot 9.6 \frac{M_P}{R} = 11 \cdot 3.08 = 33.9 \quad [\text{MN}] \quad (126)$$

The result of the analysis of design A34 is presented in figure 69, along with the analysis of the stern corner against the rigid column. It is observed that the ring stiffeners in design A34 fails at a global load equal 32 MN, quite close to the estimate.

This design can be classified as a strength design, as the required 22 MJ is dissipated before this failure.

In figure 70 the deformed bodies are presented after 2 m global displacement. Most of the deformations are located in the stern corner. The plate fields between the ring stiffeners does undergo some deformations accounting for the energy dissipation seen in the force deformation curve.

There are observed some fracturing in the outer shell of the column structure. This happen in way of the lower deck of the stern, which impacts in between two ring stiffeners.

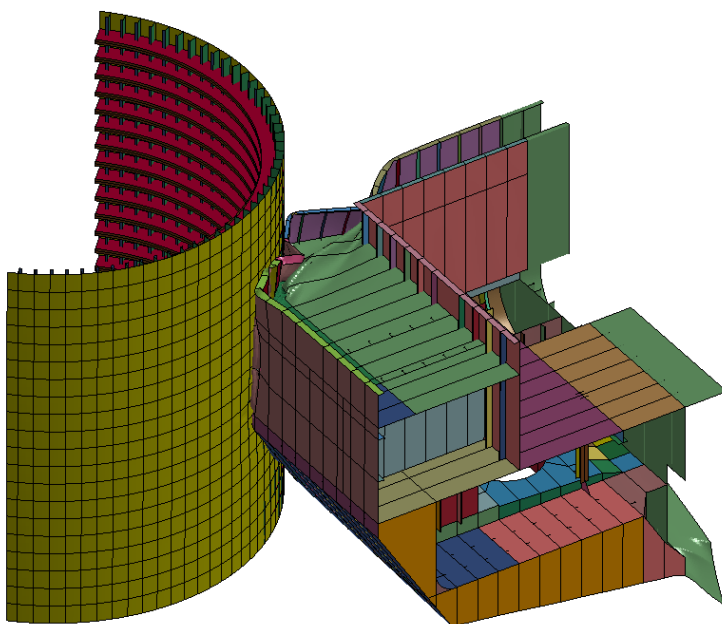


Figure 70: Deformed stern after strength design impact



## 11 Conclusion

A ship impact with a circular stiffened shell is a highly nonlinear phenomena and is largely governed by local effects not easily described using analytical methods, which makes NLFEA the tool of choice in analysing such designs. Analytical methods can never the less give insight in the dependence on the various parameters, and give a first estimate for the resistance.

Several analytical methods were explored in an effort to describe the collapse of the ring stiffeners. From the analysis of the full column it was found that the ring stiffener can be represented by a semicircular arch with clamped boundaries. Both static and kinematic analyses gave the collapse load of the ring stiffener of about  $P = 9.6 \frac{M_P}{R}$ . It was found, using the finite element method, that the analytical methods predicts the collapse load well for structures that are able to carry the plastic moment without failing due to local effects. The susceptibility to local failure was captured in a dimensionless slenderness parameter  $\lambda = \frac{M_P}{N_P R}$  and it was found that the analytical models overpredicts the resistance if  $\lambda > \lambda_{lim} \simeq 0.03$ .

It was found that the vertical stiffeners contributed to the strength of the ring stiffeners by preventing vertical displacement of the ring stiffener web. This effect was particularly prominent in the designs with high  $\lambda$  values where the local buckling was an important factor. The vertical stiffeners also contribute to the global strength by carrying the impact pressure to the ring stiffeners. In the post failure phase the effect of the vertical stiffeners are important as the load is redistributed to vertical membrane loads. Here the cross sectional area is governing.

The effect of bulkheads was tested and found to not be of importance, unless the impact happened directly in line with the bulkhead. This suggests that the presence of a bulkhead should be disregarded if the impact direction is unknown. This is not to say that the bulkhead is unimportant as it provides a lot of residual strength for the column, and limits the water ingress if the outer shell is compromised.

If a deck is to be fitted in way of a ring stiffener it is found that the deck plate thickness should be no less than the web of the ring stiffener it replaces, at least in the outer region. This is to prevent a loss of initial strength by loosing a ring stiffener. After some deformation the effect of the deck greatly increases the strength of the structure as expected.

There have been observed fracturing of the outer shell in most of the analyses performed herein. Punctures like this looks to be unavoidable as the locations of the strong points in the stern are unpredictable.

## 11.1 Strength design

As earlier stated, it is often a want for the designs of offshore structures to follow the strength design philosophy. The collapse of the ring stiffeners is proposed as a limit for when a structure no longer can be classified as a strength design. After the loss of the ring stiffeners the resistance decreases and large deformations occur.

The following suggestions are made in order to obtain a strength design. These are mainly to ensure that there are no loss of ring stiffeners.

1. Find the maximal impact load, either by design curves or by FEA where the installation is kept rigid.
2. Establish the collapse load of a single ring stiffener by FEA, or use  $P_{cr} \simeq 9.6 \frac{M_F}{R}$  as an estimate.
3. Design ring stiffener sections such that  $\lambda < \lambda_{lim}$ .
4. Use symmetrical stiffener sections (i.e. T instead of L or FB).
5. Ensure that no ring stiffener carry more than the collapse load. In lieu of a better estimate divide the total load in equal parts between the ring stiffeners in direct contact with the ship.
6. Deck plating thickness should be no less than the thickness of the RS web in the outer region.
7. Bulkheads should not be considered if the impact can happen out of line with the bulkhead.
8. The shell plating should be kept thin to reduce weight.

## 12 Further work

The model proposed for the progressive collapse of the ring stiffener does not take the crushing of the ring stiffener web in point A into account. Neither does it include the effect of the plate flange buckling. Both these effects reduces the moment capacity in hinge A, and should be included to fully capture the collapse. A small angle approximation of the kinematic model should also be established to find a analytic expression for the collapse load.

Some evidence suggest that the local crushing of the ring stiffener web in point A is the catalytic factor for the collapse of the ring stiffeners. This effect should therefore be studied in greater detail.

The effect of vertical stiffeners on the collision resistance should be further studied, and if relevant included in the analytical model of the structural capacity.

The static model of the collapse should be extended to include the difference in moment in point A and C. This will include solving for the elastic moment distribution in the case where hinge A have formed, but not hinge C.

A model of the post failure phase should be developed in order to describe shared energy designs. The analyses herein suggest that the area of the vertical stiffeners will be an important parameter in such a model.



---

## References

- Alsos, H. S., Amdahl, J., and Hopperstad, O. S. (2009). On the resistance to penetration of stiffened plates, Part II: Numerical analysis. *International Journal of Impact Engineering*, 36(7):875–887.
- Amdahl, J. (1983). *Energy absorption in ship-platform impacts*. PhD thesis, Divisions of Marine Structures, The Norwegian Institute of Technology, The University of Trondheim, Trondheim.
- Amdahl, J. (2013). TMR 4205 Buckling and ultimate strength of marine structures.
- Bergan, P. G. and Syvertsen, T. G. (1977). *Knekning av søyler og rammer*. Tapir, Trondheim.
- Callister, jr, W. D. and Rethwisch, D. G. (2015). *Materials Science and Engineering*. Wiley, ninth edition edition.
- Cook, R. D., Malkus, D. S., Plesha, M. E., and Witt, R. J. (2002). *Concepts and applications of finite element analysis*. Wiley, New York, 4th ed. edition.
- DNV GL (2015). FE model library for collision analysis: Description and results. Technical Report 2015-0984, Rev. 1.
- DNVGL-OS-B101 (2003). Metallic materials.
- DNVGL-OS-C101 (2016). Design of Offshore Steel Structures , General ( Lrfd Method ).
- DNVGL-RP-C204 (2010). Design against accidental loads.
- DNVGL-RP-C204 (2016). PROPOSAL Design against accidental loads.
- DNVGL-RP-C208 (2016). Determination of structural capacity by non-linear finite element analysis methods.
- Do Amaral Amante, D., Trovado, L., and Estefen, S. (2008). Residual strength assessment of semi-submersible platform column due to supply vessel collision. In *Proceedings of the International Conference on Offshore Mechanics and Arctic Engineering - OMAE*, volume 2, pages 779–789.
- Eurocode 3 (2005). Eurocode 3: Design of steel structures - Part 1-1: General rules and rules for buildings.
- Hallquist, J. O. (2006). *LS-DYNA3D Theoretical Manual*. Livermore Software thecnology corporation, 2876 Waverly Way, Livermore, CA 94550, USA.

- Hu, Z., Yang, J., Xiao, L., and Yan, X. (2009). Global strength assessment for semi-submersible column after supply vessel collision accident. In *Proceedings of the International Conference on Offshore Mechanics and Arctic Engineering - OMAE*, volume 2, pages 75–83.
- Huang, J. and Wierzbicki, T. (1993). Plastic tripping of ring stiffeners. *Journal of Structural Engineering*, 119(5):1622–1642.
- Johansen, A. and Amdahl, J. (1997). Ship impact against floating platforms simulated with LS-DYNA3D. Technical report.
- Langen, I. (1999). *Dynamisk analyse av konstruksjoner*. [s.n.].
- Larsen, C. M. (2014). *TMR 4182 Marine Dynamics*. Akademika forlag.
- LS-DYNA (2003). *LS-DYNA Keyword User's Manual*. Livermore Software Technology Corporation.
- LS-DYNA Support. Contact types. <https://www.dynasupport.com/tutorial/contact-modeling-in-ls-dyna/contact-types>. Accessed: 2018-05-15.
- LS-DYNA Support. Mass scaling. <https://www.dynasupport.com/howtos/general/mass-scaling>. Accessed: 2018-18-15.
- Moan, T. (1994). *Design of Marine Structures*, volume 1. Department of Marine Technology, Norwegian University of Science and Technology, Trondheim.
- Moan, T. (2003). *Finite element modelling and analysis of marine structures*. Department of Marine Technology, Norwegian University of Science and Technology, Trondheim.
- NORSOK-N003 (2016). Action and action effects.
- NORSOK-N004 (2004). Design of steel structures, annex a, design against accidental actions.
- Ottosen, N. and Petersson, H. (1992). *Introduction to the finite element method*. Pearson, Prentice Hall.
- Spoorenberg, R. C., Snijder, H. H., and Hoenderkamp, J. C. D. (2012). A theoretical method for calculating the collapse load of steel circular arches. *Engineering Structures*, 38:89–103.
- Storheim, M. (2016). *Structural response in ship-platform and ship-ice collisions*. PhD thesis, Norwegian University of Science and Technology, Faculty of Natural Sciences and Technology, Department of Marine Technology, Trondheim.

- Storheim, M., Alsos, H. S., Hopperstad, O. S., and Amdahl, J. (2015). A damage-based failure model for coarsely meshed shell structures. *International Journal of Impact Engineering*, 83:59–75.
- Timoshenko, S. P. and Gere, J. M. (1961). *Theory of elastic stability*. Engineering Societies monographs. McGraw-Hill Book Company, second edition.
- Yu, Z. (2017). *Hydrodynamic and structural aspects of ship collisions*. PhD thesis, Norwegian University of Science and Technology, Faculty of Engineering Science and Technology, Department of Marine Technology, Trondheim.





# A Dimensions

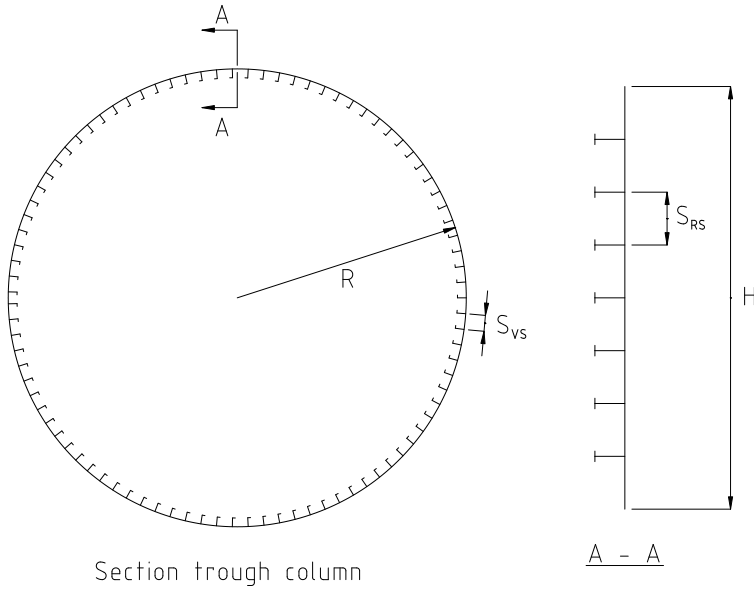


Figure A.1: Principal drawing of the column

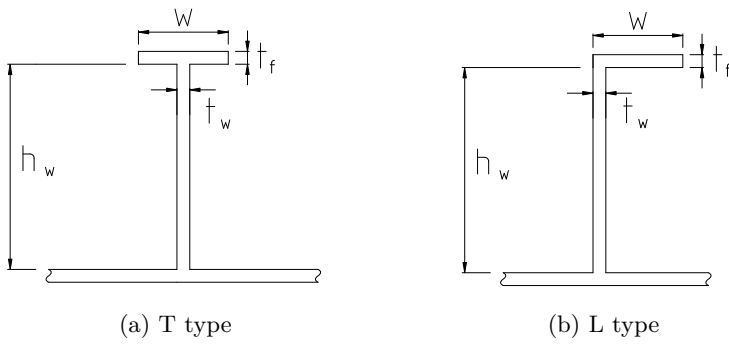


Figure A.2: Stiffener definitions

## Dimensions A-series

Design	R	H	$t_{shell}$	$S_{VS}$	Vertical stiffeners					$S_{RS}$	Ring stiffeners				
					Type	$h_w$	w	$t_w$	$t_f$		Type	$h_w$	w	$t_w$	$t_f$
A01	6500	12000	12	450	L	250	80	9	12	1500	T	850	300	14	20
A02	6500	12000	12	450	L	250	80	9	12	3000	T	850	300	14	20
A03	6500	12000	12	1350	L	250	80	9	12	1500	T	850	300	14	20
A04	6500	12000	24	450	L	250	80	9	12	1500	T	850	300	14	20
A05	6500	12000	12	450	L	250	80	9	12	1500	L	850	300	14	20
A06	6500	12000	18	450	L	250	80	9	12	1500	T	850	300	14	20
A07	6500	12000	12	450	L	250	80	9	12	1500	T	400	300	30	20
A08	6500	12000	12	450	L	250	80	9	12	1500	T	1000	145	16.5	9.5
A09	6500	12000	24	450	L	250	80	9	12						
A10	6500	12000	12	450	L	350	110	13	17	1500	T	850	300	14	20
A11	6500	12000	12	450	L	250	80	9	12	1500	FB	1135		15.8	
A12	6500	12000	12	900	L	350	110	13	17	1500	T	850	300	14	20
A13	6500	12000	12	225	L	180	60	6	9	1500	T	850	300	14	20
A14 <sup>D</sup>	6500	12000	12	450	L	250	80	9	12	1500	T	850	300	14	20
A15 <sup>B</sup>	6500	12000	12	450	L	250	80	9	12	1500	T	850	300	14	20
A16	6500	12000	12							1500	T	850	300	14	20
A17	6500	12000	12	900	L	250	80	9	12	1500	T	850	300	14	20
A18	6500	12000	6	450	L	250	80	9	12	1500	T	850	300	14	20
A19	6500	12000	12	450	L	250	80	10	15	1500	T	850	300	14	20
A20	6500	12000	12	450	L	250	80	15	20	1500	T	850	300	14	20
A21	6500	12000	12	450	L	250	80	9	12	1500	T	1000	450	20	30
A22	6500	12000	12	450	L	250	80	9	12	1000	T	850	300	14	20
A23	6500	12000	12	450	L	250	80	9	12	2000	T	850	300	14	20
A24	6500	12000	12	450	L	250	80	9	12	2400	T	850	300	14	20
A25	6500	12000	12	450	L	250	80	9	12	1200	T	850	300	14	20

Design	R	H	$t_{shell}$	$S_{VS}$	Vertical stiffeners					$S_{RS}$	Ring stiffeners				
					Type	$h_w$	w	$t_w$	$t_f$		Type	$h_w$	w	$t_w$	$t_f$
A26	6500	12000	12	450	L	250	80	9	12	800	T	850	300	14	20
A27	6500	12000	12	450	L	250	80	9	12	1500	T	650	150	14	20
A28	6500	12000	12	450	L	250	80	9	12	1000	T	650	150	14	20
A29	6500	12000	12	450	L	250	80	9	12	800	T	650	150	14	20
A30	6500	12000	12	450	L	250	80	9	12	600	T	650	150	14	20
A31	6500	12000	12	450	L	250	80	9	12	1500	T	650	150	20	30
A32	6500	12000	12	450	L	250	80	9	12	1000	T	650	150	20	30
A33	6500	12000	12	450	L	250	80	9	12	800	T	650	150	20	30
A34	6500	12000	12	450	L	250	80	9	12	600	T	650	150	20	30
A35 <sup>D</sup>	6500	12000	12	450	L	250	80	9	12	1500	T	850	300	14	20

<sup>D</sup>Including one deck

<sup>B</sup>Including one bulkhead

Design	$H_{deck}$	$t_{deck}$	S	Stiffeners					Ring flange	
				Type	$h_w$	w	$t_w$	$t_f$	$h_w$	$t_w$
A14	6000	12	650	L	250	80	9	12	250	15
A35	6000	14	650	L	250	80	9	12	250	15

Design	Placement	$t_{plate}$	$S_{VS}$	Vertical stiffeners					$S_{HS}$	Horizontal stiffeners				
				Type	$h_w$	w	$t_w$	$t_f$		Type	$h_w$	w	$t_w$	$t_f$
A15	center, x-direction	12	650	L	250	80	9	12	1500	T	850	300	14	20

## Dimensions C-series

Design	R	H	$t_{shell}$	$S_{RS}$	Ring stiffener					$\sigma_Y$
					Type	$h_w$	w	$t_w$	$t_f$	
C01	6500	1500	12	1500	T	850	300	14	20	355
C02	6500	1500	12	1500	T	850	300	20	30	355
C03	6500	1500	12	1500	T	650	150	14	20	355
C04	6500	1500	24	1500	T	650	150	14	20	355
C05	6500	1500	6	1500	T	850	300	14	25	355
C06	6500	1500	12	1500	T	850	300	14	20	300
C07	6500	1500	12	1500	T	850	300	14	20	400
C08	6500	1500	12	1500	T	650	150	20	30	355
C09	6500	1500	18	1500	T	650	150	10	12	355
C10	6500	1500	12	1500	T	850	300	10	12	355
C11	6500	1000	12	1000	T	850	200	14	20	355
C12	6500	2000	12	2000	T	850	400	14	20	355
C13	7800	1500	12	1500	T	1020	300	14	20	355
C14	5000	1500	12	1500	T	653.85	250	14	20	355
C15	6500	1500	12	1500	T	650	100	14	20	355
C16	6500	1500	12	1500	T	650	200	14	20	355
C17	6500	1500	12	1500	T	650	50	14	20	355
C18	6500	1500	12	1500	T	650	300	14	20	355
C19	6500	1500	12	1500	T	650	450	14	20	355
C20	6500	1500	12	1500	T	450	300	14	20	355
C21	6500	1500	18	1500	T	450	300	14	20	355
C22	6500	1500	12	1500	T	650	150	25	20	355

## B Control cards used in the analyses

---

```

1 *CONTACT_AUTOMATIC_SURFACE_TO_SURFACE_ID
2 $#   cid                               title
3     1leg to ship
4 $#   ssid   msid   sstyp   mstyp   sboxid   mboxid   spr   mpr
5       3     1     2     2     0     0     1     1
6 $#   fs     fd     dc     vc     vdc   penchk   bt     dt
7       0.0   0.0   0.0   0.0   0.0   0     0.01.00000E20
8 $#   sfs    sfm    sst    mst    sfst   sfmt    fsf    vsf
9       1.0   1.0   2.0   0.0   1.0   1.0   1.0   1.0
10 *CONTACT_AUTOMATIC_SINGLE_SURFACE_ID
11 $#   cid                               title
12     2ship internal
13 $#   ssid   msid   sstyp   mstyp   sboxid   mboxid   spr   mpr
14       2     0     2     0     0     0     0     0
15 $#   fs     fd     dc     vc     vdc   penchk   bt     dt
16       0.0   0.0   0.0   0.0   0.0   0     0.01.00000E20
17 $#   sfs    sfm    sst    mst    sfst   sfmt    fsf    vsf
18       1.0   1.0   0.0   0.0   1.0   1.0   1.0   1.0
19 *CONTROL_CONTACT
20 $#   slsfac  rwpnal  islchk  shlthk  penopt  thkchg  orien  enmass
21       0.0   0.0     0     2     0     1     0     0
22 $#   usrstr  usrfrc  nsbcs  interm  xpene  ssthk  ecdt  tiedprj
23       0     0     0     0     0.0   0     0     0
24 $#   sfric  dfric  edc    vfc    th    th_sf  pen_sf
25       0.0   0.0   0.0   0.0   0.0   0.0   0.0
26 $#   ignore  frceng  skiprwg  outseg  spotstp  spotdel  spothin
27       0     0     0     0     0     0     0
28 $#   isym  nserod  rwgaps  rwgdth  rwksf  icov  swradf  ithoff
29       0     0     1     0.0   1.0   0     0.0   0
30 $#   shldg  pstiff  ithcnt  tdcnof  ftall  unused  shltrw
31       0     0     0     0     0     0     0.0
32 *CONTROL_ACCURACY
33 $#   osu    inn  pidosu  iacc
34       0     2     0     0
35 *CONTROL_ENERGY
36 $#   hgen  rwen  slnten  rylen
37       2     2     2     1
38 *CONTROL_HOURLASS
39 $#   ihq    qh
40       4     0.03
41 *CONTROL_TERMINATION
42 $#   endtim  endcyc  dtmin  endeng  endmas
43       1.0   0     0.0   0.0   0.0
44 *CONTROL_TIMESTEP
45 $#   dtinit  tssfacs  isdo  tslimit  dt2ms  lctm  erode  ms1st
46       0.01  0.9     0     0.0-3.0000E-6  0     0     0
47 $#   dt2msf  dt2mslc  imslc  unused  unused  rmscl
48       0.0   0     0     0.0

```

---



## C Derivation of interaction equations

When a cross section is loaded with both moment and axial stress the capacity for carrying both kinds of loading is reduced. This reduction will follow an interaction equation. In this appendix the interaction equations are derived for a I-stiffener without vertical symmetry, with the plastic neutral axis in the web. The plastic neutral axis is placed a distance  $z_0$  above the inside of the plate flange, this distance can be expressed as:

$$z_0 = \frac{1}{t_w} \left( \frac{1}{2} A_e - A_p \right) = \frac{A_e}{2t_w} \left( 1 - 2 \frac{A_p}{A_e} \right) \quad (C.1)$$

where  $A_e$  is the total area of the stiffener including the plate flange,  $A_p$  is the area of said plate flange and  $t_w$  is the thickness of the web. Further  $A_t = wt_f$  if defined to be the area of the top flange, and  $A_w = h_w t_w$  the area of the web. The neutral axis is assumed to remain stationary during all the stages.

The equations are derived on the assumption that the moment and axial force is independent and "occupy" different parts of the cross section. The entire cross section is yielding and the material is assumed perfectly plastic such that the stresses have the value  $\pm\sigma_Y$  and are working normal to the cross section surface.

The interaction is divided into four stages.

### Stage 1

In stage one the area occupied by the axial forces are limited to the web. The axial force does not give any resulting moment and the area is thereby placed symmetrically around the plastic neutral axis, extending a distance  $z_1$  in both directions.

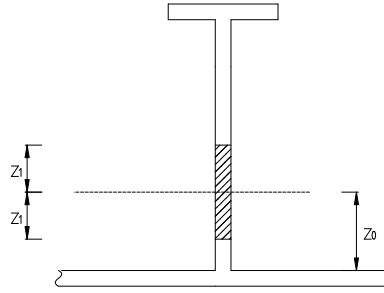


Figure C.1: Stage 1

The axial force can be written as:

$$N = 2z_1 t_w \sigma_Y \quad (\text{C.2})$$

or on the normalised form as:

$$\frac{N}{N_P} = \frac{2z_1 t_w}{A_e} \quad (\text{C.3})$$

where  $N_P = A_e \sigma_Y$  is the full plastic capacity in axial loading only.

The moment carried by the rest of the cross section is written as

$$M = M_P - 2 \left( \frac{1}{2} z_1^2 t_w \right) \quad (\text{C.4})$$

giving

$$\frac{M}{M_P} = 1 - \frac{z_1^2 t_w}{W_P} \quad (\text{C.5})$$

where  $W_P$  is the full plastic section modulus for the cross section.

Solving equation C.3 for  $z_1$  and inserting in equation C.5 gives the interaction equation for stage 1 as:

$$\frac{M}{M_P} = 1 - \frac{A_e^2}{4t_w W_P} \left( \frac{N}{N_P} \right)^2 \quad (\text{C.6})$$

Stage 1 is limited by level of axial force when  $z_1 = z_0$  and the area carrying axial force reaches the plate flange. This axial force is termed  $\hat{N}$  and is given as:

$$\frac{\hat{N}}{N_P} = \frac{2t_w z_0}{A_e} = \left( 1 - 2 \frac{A_P}{A_e} \right) \quad (\text{C.7})$$



It is noted that the distance  $z_0$  can be expressed in terms of this limiting force in the following manner:

$$z_0 = \frac{A_e}{2t_w} \frac{\hat{N}}{N_P} \quad (\text{C.8})$$

## Stage 2

In stage two the area where the axial forces are working is limited by two parameters  $z_1$  and  $z_2$  as given in figure C.2.

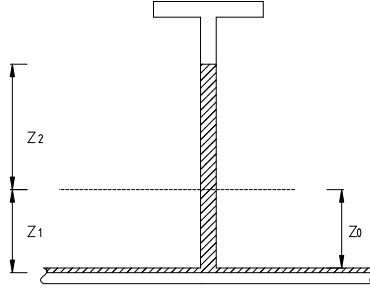


Figure C.2: Stage 2

The area of the plate flange that is occupied by the axial force is denoted  $A_p^*$ .

The axial force is given as:

$$\frac{N}{N_P} = \frac{A_p^*}{A_e} + \frac{t_w(z_0 + z_2)}{A_e} \quad (\text{C.9})$$

The moment does not contribute to the axial force, giving:

$$A_f + t_w(h - z_2 - z_0) = A_p - A_p^* \quad (\text{C.10})$$

$$A_f + A_w - t_w(z_2 + z_0) = A_p - A_p^* \quad (\text{C.11})$$

$$A_f + A_w - A_p = t_w(z_2 + z_0) - A_p^* \quad (\text{C.12})$$

$$A_e - 2A_p = t_w(z_2 + z_0) - A_p^* \quad (\text{C.13})$$

$$\frac{\hat{N}}{N_P} = 1 - 2\frac{A_p}{A_e} = \frac{t_w(z_2 + z_0)}{A_e} - \frac{A_p^*}{A_e} \quad (\text{C.14})$$

$$\frac{A_p^*}{A_e} = \frac{t_w(z_2 + z_0)}{A_e} - \frac{\hat{N}}{N_P} \quad (\text{C.15})$$

Inserting in equation C.9

$$\frac{N}{N_P} = \frac{t_w(z_2 + z_0)}{A_e} - \frac{\hat{N}}{N_P} + \frac{t_w(z_0 + z_2)}{A_e} \quad (\text{C.16})$$

$$\frac{N}{N_P} = \frac{2t_w(z_2 + z_0)}{A_e} - \frac{\hat{N}}{N_P} \quad (\text{C.17})$$

$$\frac{N}{N_P} = \frac{2t_w z_2}{A_e} + \frac{2t_w z_0}{A_e} - \frac{\hat{N}}{N_P} \quad (\text{C.18})$$

Inserting for  $z_0$

$$\frac{N}{N_P} = \frac{2t_w z_2}{A_e} + \frac{\hat{N}}{N_P} - \frac{\hat{N}}{N_P} \quad (\text{C.19})$$

$$\frac{N}{N_P} = \frac{2t_w z_2}{A_e} \quad (\text{C.20})$$

$$\frac{A_e}{2t_w} \frac{N}{N_P} = z_2 \quad (\text{C.21})$$

Inserting this expression back into equation C.9

$$\frac{N}{N_P} = \frac{A_p^*}{A_e} + \frac{t_w z_0}{A_e} + \frac{t_w z_2}{A_e} \quad (\text{C.22})$$

$$\frac{N}{N_P} = \frac{A_p^*}{A_e} + \frac{t_w}{A_e} \frac{A_e}{2t_w} \frac{\hat{N}}{N_P} + \frac{t_w}{A_e} \frac{A_e}{2t_w} \frac{N}{N_P} \quad (\text{C.23})$$

$$\frac{N}{N_P} = \frac{A_p^*}{A_e} + \frac{1}{2} \frac{\hat{N}}{N_P} + \frac{1}{2} \frac{N}{N_P} \quad (\text{C.24})$$

$$\frac{1}{2} \left( \frac{N}{N_P} - \frac{\hat{N}}{N_P} \right) = \frac{A_p^*}{A_e} \quad (\text{C.25})$$

The area  $A_p^*$  can also be given in terms of the distance  $z_1$

$$\frac{1}{2} \left( \frac{N}{N_P} - \frac{\hat{N}}{N_P} \right) = \frac{A_p^*}{A_e} = \frac{S(z_1 - z_0)}{A_e} \quad (\text{C.26})$$

$$\frac{A_e}{2S} \left( \frac{N}{N_P} - \frac{\hat{N}}{N_P} \right) = z_1 - z_0 \quad (\text{C.27})$$

$$\frac{A_e}{2S} \left( \frac{N}{N_P} - \frac{\hat{N}}{N_P} \right) + z_0 = z_1 \quad (\text{C.28})$$

$$\frac{A_e}{2S} \left( \frac{N}{N_P} - \frac{\hat{N}}{N_P} \right) + \frac{A_e}{2t_w} \frac{\hat{N}}{N_P} = z_1 \quad (\text{C.29})$$

$$\frac{A_e}{2S} \left( \frac{N}{N_P} - \frac{\hat{N}}{N_P} \left( 1 - \frac{S}{t_w} \right) \right) = z_1 \quad (\text{C.30})$$

Now the moment can be expressed

$$\frac{M}{M_P} = 1 - \frac{1}{W_P} \left[ \frac{1}{2} t_w z_2^2 + \frac{1}{2} t_w z_0^2 + A_p^* z_1 \right] \quad (\text{C.31})$$

$$\frac{M}{M_P} = 1 - \frac{1}{W_P} \left[ \frac{1}{2} t_w \left( \frac{A_e}{2t_w} \frac{N}{N_P} \right)^2 + \frac{1}{2} t_w \left( \frac{A_e}{2t_w} \frac{\hat{N}}{N_P} \right)^2 + A_p^* z_1 \right] \quad (\text{C.32})$$

$$\frac{M}{M_P} = 1 - \frac{A_e^2}{4W_P t_w} \left[ \frac{1}{2} \left( \frac{N}{N_P} \right)^2 + \frac{1}{2} \left( \frac{\hat{N}}{N_P} \right)^2 + \frac{2A_p^*}{A_e} \frac{2t_w z_1}{A_e} \right] \quad (\text{C.33})$$

$$\begin{aligned} \frac{M}{M_P} = 1 - \frac{A_e^2}{4W_P t_w} & \left[ \frac{1}{2} \left( \frac{N}{N_P} \right)^2 + \frac{1}{2} \left( \frac{\hat{N}}{N_P} \right)^2 \right. \\ & \left. + \left( \frac{N}{N_P} - \frac{\hat{N}}{N_P} \right) \frac{t_w}{S} \left( \frac{N}{N_P} - \frac{\hat{N}}{N_P} \left( 1 - \frac{S}{t_w} \right) \right) \right] \quad (\text{C.34}) \end{aligned}$$

$$\begin{aligned} \frac{M}{M_P} = 1 - \frac{A_e^2}{4W_P t_w} & \left[ \frac{1}{2} \left( \frac{N}{N_P} \right)^2 + \frac{1}{2} \left( \frac{\hat{N}}{N_P} \right)^2 \right. \\ & \left. + \frac{t_w}{S} \left( \left( \frac{N}{N_P} \right)^2 - \frac{N}{N_P} \frac{\hat{N}}{N_P} \left( 1 - \frac{S}{t_w} \right) - \frac{N}{N_P} \frac{\hat{N}}{N_P} + \left( \frac{\hat{N}}{N_P} \right)^2 \left( 1 - \frac{S}{t_w} \right) \right) \right] \quad (\text{C.35}) \end{aligned}$$

$$\begin{aligned}
 \frac{M}{M_P} = 1 - \frac{A_e^2}{4W_P t_w} & \left[ \frac{1}{2} \left( \frac{N}{N_P} \right)^2 + \frac{1}{2} \left( \frac{\hat{N}}{N_P} \right)^2 \right. \\
 & \left. + \frac{t_w}{S} \left( \left( \frac{N}{N_P} \right)^2 - \frac{N}{N_P} \frac{\hat{N}}{N_P} \left( 2 - \frac{S}{t_w} \right) + \left( \frac{\hat{N}}{N_P} \right)^2 \left( 1 - \frac{S}{t_w} \right) \right) \right] \quad (C.36)
 \end{aligned}$$

$$\begin{aligned}
 \frac{M}{M_P} = 1 - \frac{A_e^2}{4W_P t_w} & \left[ \frac{1}{2} \left( \frac{N}{N_P} \right)^2 + \frac{1}{2} \left( \frac{\hat{N}}{N_P} \right)^2 \right. \\
 & \left. + \frac{t_w}{S} \left( \frac{N}{N_P} \right)^2 - \frac{N}{N_P} \frac{\hat{N}}{N_P} \left( 2 \frac{t_w}{S} - 1 \right) + \left( \frac{\hat{N}}{N_P} \right)^2 \left( \frac{t_w}{S} - 1 \right) \right] \quad (C.37)
 \end{aligned}$$

$$\begin{aligned}
 \frac{M}{M_P} = 1 - \frac{A_e^2}{4W_P t_w} & \left[ \left( \frac{N}{N_P} \right)^2 \left( \frac{1}{2} + \frac{t_w}{S} \right) + \left( \frac{\hat{N}}{N_P} \right)^2 \left( \frac{1}{2} + \frac{t_w}{S} - 1 \right) \right. \\
 & \left. + \frac{N}{N_P} \frac{\hat{N}}{N_P} \left( 1 - 2 \frac{t_w}{S} \right) \right] \quad (C.38)
 \end{aligned}$$

Giving the final expression

$$\begin{aligned}
 \frac{M}{M_P} = 1 - \frac{A_e^2}{4W_P t_w} & \left[ \left( \frac{N}{N_P} \right)^2 \left( \frac{1}{2} + \frac{t_w}{S} \right) + 2 \frac{N}{N_P} \frac{\hat{N}}{N_P} \left( \frac{1}{2} - \frac{t_w}{S} \right) \right. \\
 & \left. - \left( \frac{\hat{N}}{N_P} \right)^2 \left( \frac{1}{2} - \frac{t_w}{S} \right) \right] \quad (C.39)
 \end{aligned}$$

The limiting axial force for this stage is

$$\frac{\hat{N}}{N_P} = \left( 1 - 2 \frac{A_f}{A_e} \right) \quad (C.40)$$

### Stage 3

In stage three the area occupied by the axial force have developed into the top flange.

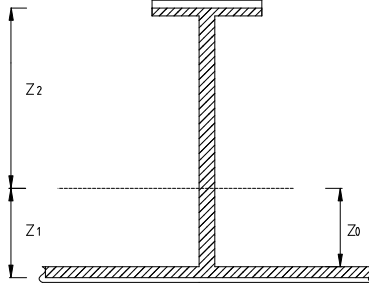


Figure C.3: Stage 2

The area occupied in the top and plate flange is denoted  $A_f^*$  and  $A_p^*$  respectively. Under the condition that the moment does not contribute to the axial force the remaining areas must be equal

$$A_f - A_f^* = A_p - A_p^* \Rightarrow A_p^* = A_p - A_f + A_f^* \quad (C.41)$$

The axial force is given:

$$\frac{N}{N_P} = \frac{A_w + A_f^* + A_p^*}{A_e} \quad (C.42)$$

$$\frac{N}{N_P} = \frac{A_w + A_f^* + A_p - A_f + A_f^*}{A_e} \quad (C.43)$$

$$\frac{N}{N_P} = \frac{A_e - 2A_f + 2A_f^*}{A_e} \quad (C.44)$$

$$\frac{N}{N_P} = 1 - 2\frac{A_f}{A_e} + 2\frac{w(z_2 - (h_w - z_0))}{A_e} \quad (C.45)$$

$$\frac{N}{N_P} = \frac{\hat{N}}{N_P} + 2\frac{w(z_2 - (h_w - z_0))}{A_e} \quad (C.46)$$

And it follows that the distance  $z_2$  is

$$z_2 = h_w - z_0 + \frac{A}{2w} \left( \frac{N}{N_P} - \frac{\hat{N}}{N_P} \right) \quad (\text{C.47})$$

Using the same approach the distance  $z_1$  is given

$$z_1 = z_0 + \frac{A_e}{2S} \left( \frac{N}{N_P} - \frac{\hat{N}}{N_P} \right) \quad (\text{C.48})$$

The moment carried by the cross section is

$$\frac{M}{\sigma_Y} = (A_f - A_f^*)z_2 + (A_p - A_p^*)z_1 \quad (\text{C.49})$$

$$\frac{M}{\sigma_Y} = (A_p - A_p^*)[z_2 + z_1] \quad (\text{C.50})$$

$$\frac{M}{\sigma_Y} = (A_p - A_p^*) \left[ h_w + \frac{A_e}{2w} \left( \frac{N}{N_P} - \frac{\hat{N}}{N_P} \right) + \frac{A_e}{2S} \left( \frac{N}{N_P} - \frac{\hat{N}}{N_P} \right) \right] \quad (\text{C.51})$$

The area  $(A_p - A_p^*)$  is

$$(A_p - A_p^*) = A_p - S(z_1 - z_0) \quad (\text{C.52})$$

$$(A_p - A_p^*) = A_p - \frac{A_e}{2} \left( \frac{N}{N_P} - \frac{\hat{N}}{N_P} \right) \quad (\text{C.53})$$

Inserting into equation C.51:

$$\begin{aligned} \frac{M}{M_P} &= \frac{1}{W_P} \left( A_p - \frac{A_e}{2} \left( \frac{N}{N_P} - \frac{\hat{N}}{N_P} \right) \right) \left[ h_w + \frac{A_e}{2w} \left( \frac{N}{N_P} - \frac{\hat{N}}{N_P} \right) \right. \\ &\quad \left. + \frac{A_e}{2S} \left( \frac{N}{N_P} - \frac{\hat{N}}{N_P} \right) \right] \end{aligned} \quad (\text{C.54})$$

$$\begin{aligned} \frac{M}{M_P} &= \frac{A_e^2}{4t_w W_P} \left( 2 \frac{A_p}{A_e} - \left( \frac{N}{N_P} - \frac{\hat{N}}{N_P} \right) \right) \left[ \frac{A_w}{A_e} + \frac{t_w}{w} \left( \frac{N}{N_P} - \frac{\hat{N}}{N_P} \right) \right. \\ &\quad \left. + \frac{t_w}{S} \left( \frac{N}{N_P} - \frac{\hat{N}}{N_P} \right) \right] \end{aligned} \quad (\text{C.55})$$

Giving the final expression:

$$\begin{aligned} \frac{M}{M_P} = \frac{A_e^2}{4t_w W_P} \left(1 - \frac{N}{N_P}\right) & \left[ \frac{A_w}{A_e} + \frac{t_w}{w} \left( \frac{N}{N_P} - \frac{\hat{N}}{N_P} \right) \right. \\ & \left. + \frac{t_w}{S} \left( \frac{N}{N_P} - \frac{\hat{N}}{N_P} \right) \right] \end{aligned} \quad (C.56)$$

The expression is valid until the entire cross section is occupied by axial force, that is

$$\frac{N}{N_P} = 1 \quad (C.57)$$





## D Derivation of mechanism angles

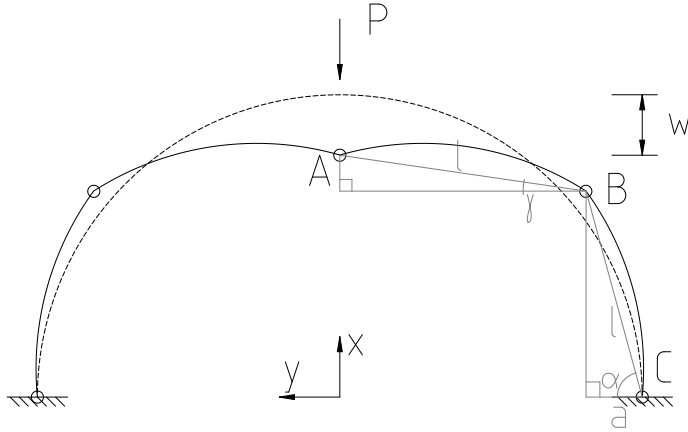


Figure D.1: Kinematic model

Relations between the displacement  $w$  of point A and the rotations of the yield hinges are needed in order to describe the energy necessary to deform the structure.

It is assumed that all deformations happen in the yield hinges, and that hinge B forms at an angle  $\frac{\pi}{4}$  from the impact location. From this one can observe that the undeformed structure is described by a regular octagon with internal angles  $\frac{3\pi}{4}$ . The side lengths of this octagon is denoted  $l$  and is given as:

$$l = 2R \sin \frac{\pi}{8} \quad (\text{D.1})$$

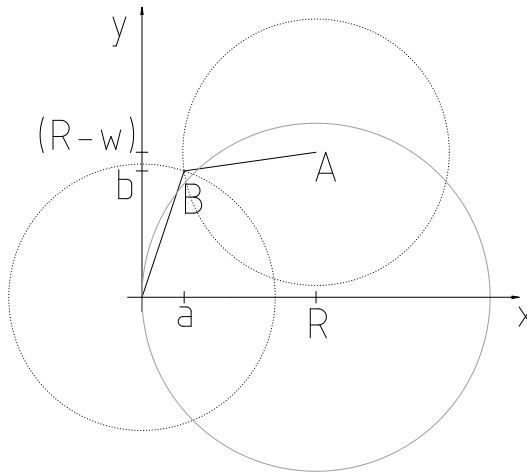


Figure D.2: Calculation model for position of point B

In figure D.2 point A and B is drawn into a Cartesian coordinate system. Point B have the coordinate  $B = (a, b)$ . Under the assumption that the side lengths in the original octagon does not change, it is observed that point B must be located at the intersection between two circles given as:

$$x^2 + y^2 = l^2 \quad (\text{D.2})$$

$$(x - R)^2 + (y - (R - w))^2 = l^2 \quad (\text{D.3})$$

such that the point  $B = (a, b)$  can be written

$$a^2 + b^2 = l^2 \quad (\text{D.4})$$

$$(a - R)^2 + (b - (R - w))^2 = l^2 \quad (\text{D.5})$$

Taking the difference between D.5 and D.4 one obtains

$$a^2 - 2aR + R^2 - a^2 + b^2 - 2b(R - w) + (R - w)^2 - b^2 = 0 \quad (\text{D.6})$$

solving for b yields

$$b = \frac{1}{2(R-w)} (-2aR + R^2 + (R-w)^2) \quad (\text{D.7})$$

This expression is then inserted in equation D.4:

$$a^2 + \left( \frac{1}{2(R-w)} (-2aR + R^2 + (R-w)^2) \right)^2 = l^2 \quad (\text{D.8})$$

$$a^2 + \frac{1}{4(R-w)^2} [4a^2R^2 - 4aR(R^2 + (R-w)^2) + (R^2 + (R-w)^2)^2] = l^2 \quad (\text{D.9})$$

$$a^2 \left( 1 + \frac{4R^2}{4(R-w)^2} \right) - a \left( \frac{4R(R^2 + (R-w)^2)}{4(R-w)^2} \right) + \frac{(R^2 + (R-w)^2)^2}{4(R-w)^2} - l^2 = 0 \quad (\text{D.10})$$

$$a^2 \left( 1 + \left( \frac{R^2}{R-w} \right)^2 \right) - aR \left( 1 + \left( \frac{R}{R-w} \right)^2 \right) + \frac{(R^2 + (R-w)^2)^2}{4(R-w)^2} - l^2 = 0 \quad (\text{D.11})$$

$$a^2 - aR + \frac{(R^2 + (R-w)^2)^2}{4(R-w)^2 \left( 1 + \left( \frac{R^2}{R-w} \right)^2 \right)} - \frac{l^2}{\left( 1 + \left( \frac{R^2}{R-w} \right)^2 \right)} = 0 \quad (\text{D.12})$$

$$a^2 - aR + \frac{1}{4} (R^2 + (R-w)^2) - \frac{l^2(R-w)^2}{(R-w)^2 + R^2} = 0 \quad (\text{D.13})$$

Solving for  $a$  yields:

$$a = \frac{1}{2}R - \frac{1}{2}(R-w) \sqrt{\frac{4l^2}{(R-w)^2 + R^2} - 1} \quad (\text{D.14})$$

When the distances  $a$  and  $l$  are known the angles  $\alpha$  and  $\gamma$  can be expressed as

$$\cos(\alpha) = \frac{a}{l} \quad (\text{D.15})$$

$$\cos(\gamma) = \frac{R - a}{l} \quad (\text{D.16})$$

The rotations of the three hinges is then given as functions of the original undeformed angles of the octagon and the angles  $\alpha$  and  $\gamma$

$$\theta_A = \frac{3\pi}{4} - 2\left(\frac{\pi}{2} - \gamma\right) = 2\gamma - \frac{\pi}{4} \quad (\text{D.17})$$

$$\theta_B = \frac{3\pi}{4} - \left(\frac{\pi}{2} - \alpha + \frac{\pi}{2} + \gamma\right) = \alpha - \gamma - \frac{\pi}{4} \quad (\text{D.18})$$

$$\theta_C = \frac{3\pi}{8} - \alpha \quad (\text{D.19})$$

For the use in conjunction with energy dissipation only the absolute value of the rotations are interesting. The angles is therefore redefined to have a positive value for the interesting values of  $w$ .

$$\theta_A = \frac{\pi}{4} - 2\gamma \quad (\text{D.20})$$

$$\theta_B = \alpha - \gamma - \frac{\pi}{4} \quad (\text{D.21})$$

$$\theta_C = \alpha - \frac{3\pi}{8} \quad (\text{D.22})$$

## E Length of diagonal folding lines

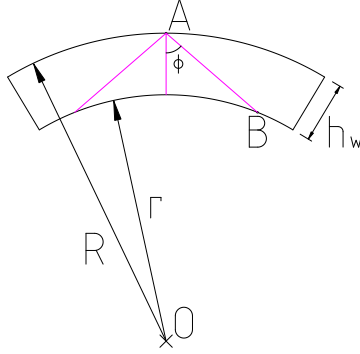


Figure E.1: Lengths of the assumed folding lines

The lengths of the diagonal yield lines are found by considering the geometrical model in figure E.1.

The angle  $\phi$  is assumed such that the folding line intersects the inner radius  $r$  at a point  $B = (a, b)$ .

With base in point  $A = (0, R)$  two vectors are defined.

$$\overrightarrow{AO} = \begin{bmatrix} 0 \\ -R \end{bmatrix}, \quad \text{and} \quad \overrightarrow{AB} = \begin{bmatrix} a \\ b - R \end{bmatrix} \quad (\text{E.1})$$

Since  $B$  lays on a circle with radius  $r = R - h_w$ , the coordinate  $a$  can be given as

$$a = \sqrt{r^2 - b^2} \quad (\text{E.2})$$

yielding vector  $\overrightarrow{AB}$  on the form:

$$\overrightarrow{AB} = \begin{bmatrix} \sqrt{r^2 - b^2} \\ b - R \end{bmatrix} \quad (\text{E.3})$$

The angle between two vectors is given

$$\cos(\theta) = \frac{v_1 \cdot v_2}{|v_1| \cdot |v_2|} \quad (\text{E.4})$$

The angle between  $\overrightarrow{AB}$  and  $\overrightarrow{AO}$  are the unknown angle  $\phi$ .

$$\cos(\phi) = \frac{-R(b - R)}{R\sqrt{r^2 - b^2 + (b - R)^2}} \quad (\text{E.5})$$

The expression for the coordinate  $b$  then follows:

$$\sqrt{r^2 - 2bR + R^2} \cos(\phi) = R - b \quad (\text{E.6})$$

$$(r^2 - 2bR + R^2) \cos^2(\phi) = R^2 - 2bR + b^2 \quad (\text{E.7})$$

$$b^2 + 2R(\cos^2(\phi) - 1)b + R^2 - (r^2 + R^2) \cos(\phi) = 0 \quad (\text{E.8})$$

Solving for  $b$  gives

$$b = -R(\cos^2(\phi) - 1) \pm \frac{1}{2} \sqrt{4R^2(\cos^2(\phi) - 1)^2 - 4(R^2 - (r^2 + R^2) \cos^2(\phi))}$$

$$b = R \sin^2(\phi) \pm \sqrt{R^2 \sin^4(\phi) - R^2 + (r^2 + R^2) \cos^2(\phi)} \quad (\text{E.9})$$

Further, normalizing on the outer radius:

$$\frac{b}{R} = \sin^2(\phi) \pm \sqrt{\sin^4(\phi) - 1 + \left(\left(\frac{r}{R}\right)^2 + 1\right) \cos^2(\phi)} \quad (\text{E.10})$$

$$\frac{b}{R} = \sin^2(\phi) \pm \sqrt{\underbrace{\sin^4(\phi) - 1 + \cos^2(\phi)}_{\cos^4(\phi) - \cos^2(\phi)} + \left(\frac{r}{R}\right)^2 \cos^2(\phi)} \quad (\text{E.11})$$

$$\frac{b}{R} = \sin^2(\phi) \pm \cos(\phi) \sqrt{\cos^2(\phi) - 1 + \left(\frac{r}{R}\right)^2} \quad (\text{E.12})$$

$$\frac{b}{R} = \sin^2(\phi) \pm \cos(\phi) \sqrt{\left(\frac{r}{R}\right)^2 - \sin^2(\phi)} \quad (\text{E.13})$$

The length of the diagonal folding line is the length of vector  $\overrightarrow{AB}$

$$l_{diag} = |\overrightarrow{AB}| = \sqrt{r^2 - 2bR + R^2} = R \sqrt{\left(\frac{r}{R}\right)^2 - 2\frac{b}{R} + 1} \quad (\text{E.14})$$

Inserting the positive expression for  $\frac{b}{R}$  gives the length of the diagonal as:

$$l_{diag} = R \sqrt{\left(\frac{r}{R}\right)^2 - 2 \sin^2(\phi) - 2 \cos(\phi) \sqrt{\left(\frac{r}{R}\right)^2 - \sin^2(\phi) + 1}} \quad (\text{E.15})$$

$$l_{diag} = R \sqrt{\left(\frac{r}{R}\right)^2 - \sin^2(\phi) - 2 \cos(\phi) \sqrt{\left(\frac{r}{R}\right)^2 - \sin^2(\phi) + 1} - \sin^2(\phi)} \quad (\text{E.16})$$

$$l_{diag} = R \sqrt{\left(\frac{r}{R}\right)^2 - \sin^2(\phi) - 2 \cos(\phi) \sqrt{\left(\frac{r}{R}\right)^2 - \sin^2(\phi) + \cos^2(\phi)}} \quad (\text{E.17})$$

$$l_{diag} = R \sqrt{\left(\sqrt{\left(\frac{r}{R}\right)^2 - \sin^2(\phi) - \cos(\phi)}\right)^2} \quad (\text{E.18})$$

$$l_{diag} = R \left| \sqrt{\left(\frac{r}{R}\right)^2 - \sin^2(\phi) - \cos(\phi)} \right| \quad (\text{E.19})$$

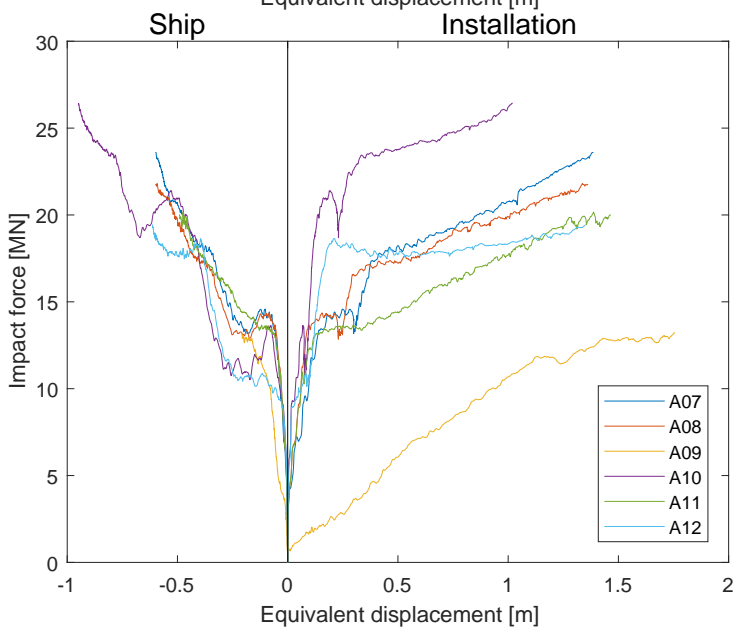
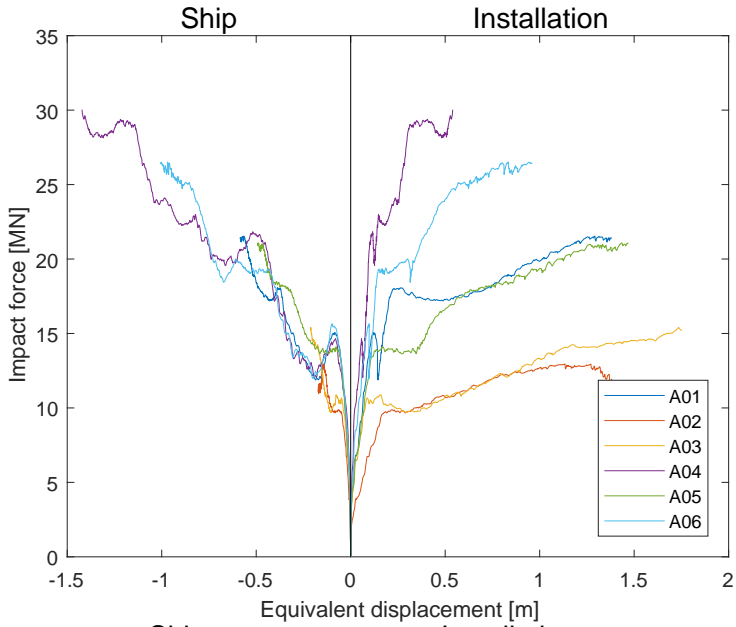
The positive length is given

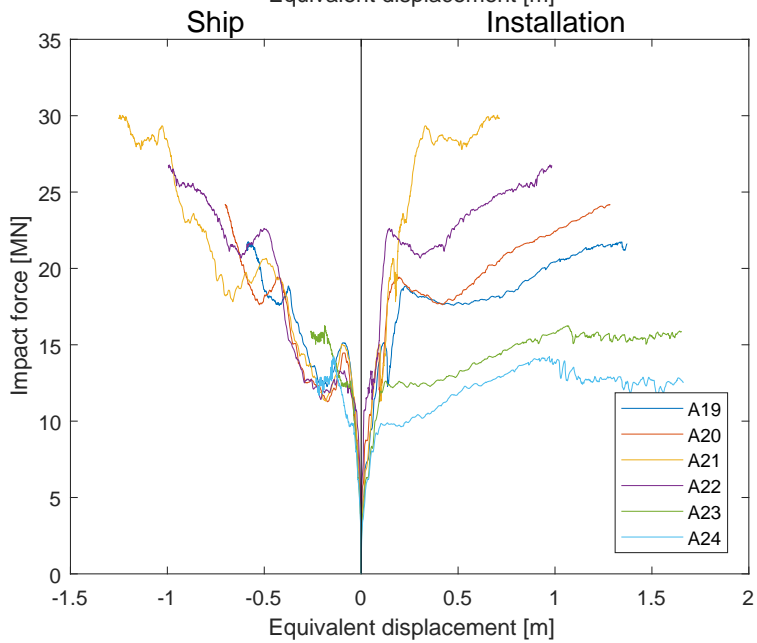
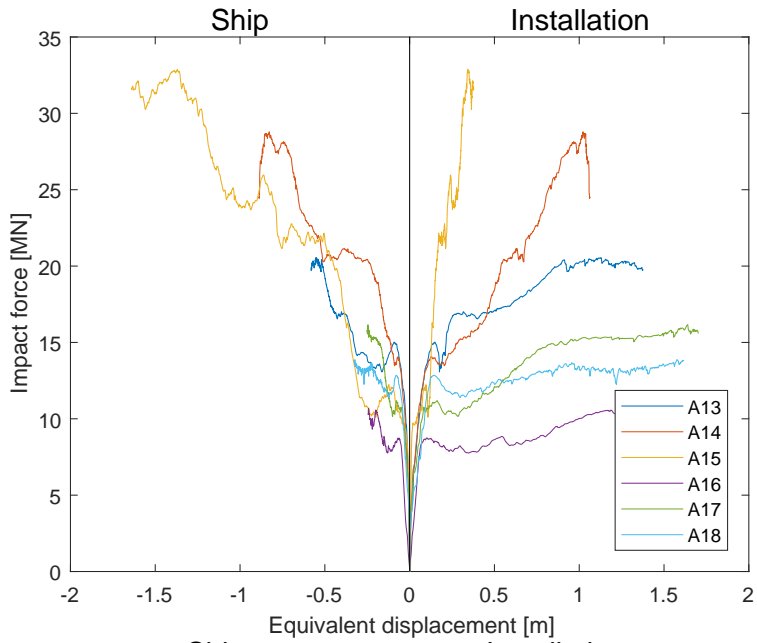
$$l_{diag} = R \left( \cos(\phi) - \sqrt{\left(\frac{r}{R}\right)^2 - \sin^2(\phi)} \right) \quad (\text{E.20})$$





## F Force deformation curves





## F. FORCE DEFORMATION CURVES

